CHALMERS
UNIVERSITY OF TECHNOLOGY

FE-Modelling of Composite Laminates for Sailboat Masts

Eric Eriksson
Emanuel Werner

Department of Industrial and Materials Science
CHALMERS UNIVERSITY OF TECHNOLOGY
Gothenburg, Sweden 2018

FE-Modelling of Composite Laminates for Sailboat Masts

Eric Eriksson

Emanuel Werner

Department of Industrial and Materials Science
Chalmers University of Technology
Gothenburg, Sweden 2018

FE-Modelling of Composite Laminates for Sailboat Masts

Department of Industrial and Materials Science
Chalmers University of Technology
SE-412 96 Göteborg Sweden
Telephone +46(0)31-772 1000
Printed by Chalmers Reproservice
Gothenburg, Sweden, 2018

Abstract

Seldén Mast is a world leading producer of aluminium sail boat masts. The company has also been developing and producing carbon fibre masts and poles for sail boat rigs for the last 20 years. Carbon fibre composites are high-performing and expensive materials, and any improvements made to the layup of the laminates will create a lighter and less expensive product. Seldén's composite masts are produced with a method called filament winding, where the resin impregnated fibre tows are wound onto a rotating aluminium mandrel with the same shape as the inside of the finished mast.

The goals of the project have been to accurately predict the bending stiffness and deflection behaviour of any given mast or pole produced by this method, to evaluate the compressive stiffness and strength of Seldén's laminates. As well as characterising the micro structure of the carbon fibre laminate in terms of out-of-plane waviness and relating this to the compressive strength of the laminate. A mix of FE analyses using the FEA software LUSAS together with actual benchmark testing has been used to compare simulation to reality. The use of high resolution misalignment analysis (HRMA) has been implemented to characterise the out-of-plane-waviness of the laminates. A method to experimentally determine the compressive strength of a carbon fibre tube has been developed and tested.

Comparing the test results to the results from the FE computations shows that it is possible to come within 15% of the actual deflection when using Seldén's previously obtained material data. There are however signs of asymmetrical bending and stiffness behaviour in non-circular cross-sections. This may occur as a result of the handling of the masts during production, but also due to irregularities in the production technique itself. Strength assessments based on the HRMA were shown to be in good agreement with the experimental values. The method developed in this project to experimentally determine compressive strength of a carbon fibre laminate tube has been shown to give satisfactory results. However, to completely confirm the method, the failure mode of the laminates in the test has to be identified.

Keywords: filament winding, stiffness modelling, carbon fibre, strength in compression, HRMA

Preface and Acknowledgement

The authors would like to give a profound thank you to the Seldén group and its employees, with special thanks to our supervisor Per Wretlind for the guidance and discussions during our work, as well as to William Holt, Neil Carstens and Greame Willcox for the technical expertise provided throughout the project. Seldén has really put the mast in Master's thesis.

A special thanks to our professor Martin Fagerström as well as our supervisor Dennis Wilhelmsson at Chalmers for their support and invaluable theoretical knowledge in the area.

This project would not have been possible without you.

We would also like to thank Johannes Qvist, Panagiota Papadopoulou and Roger Sagdahl for their assistance in the compressive tests.

Contents

List of Figures

List of Tables

1 Introduction

According to The Seldén Group, they are the world leading manufacturer of sailboat rigging systems and deck hardware for dinghies, keel boats and sailing yachts. Seldén produces and sells both aluminium and carbon fibre composite masts.

Seldén has been producing carbon fibre composite mast sections since year 2000. According to the company, good production technique, composite skills and experience has given them good products that are very competitive. However, improvements can always be made to optimise stiffness, strength and weight and also material and production costs of the laminates.

Filament winding is the manufacturing process currently employed by Seldén to produce composite masts. This method allows for parts of the process to be automated with less variations in the layup, compared to composite masts produced with hand laid laminates. In this project the effects of the filament winding process on the finished product, have been studied and documented.

1.1 Background

Carbon fibre composites (Carbon Fibre Reinforced Polymer - CFRP) are high performance construction materials. With a high specific stiffness and strength compared to other materials such as aluminium, carbon fibres can be used to make a structure lighter, stiffer and stronger at the same time. These properties come at a high price since carbon fibres are expensive and energy demanding to produce. The use of composite laminates in high-end applications is also usually more labour intensive as compared to more traditional materials. Any optimisation regarding material usage or production cycle time will make a big difference for the end user. Seldén's composite products have previously been designed using quick and easy calculations together with the expertise of their engineers. Their designs have been proven over time, but there is a chance that they can be improved further. Better predictive capabilities of stiffness based on numerical simulations and a better understanding of compressive strength will help Seldén to achieve these improvements.

The process of filament winding has been researched extensively in previous works, mainly relating to the winding process itself and different ways of calculating the roving trajectories along the geometry of the product being manufactured. However research focused on the material properties that come as a result of the production process is scarce, and no papers on the subject were found during the initial phase of the current master thesis.

1.2 Purpose and aim

The main purpose of the current master thesis was to find consistent methods and routines to model and optimise the mast section laminate layups further. The laminate calculations have been carried out with the FEA software LUSAS, regularly used by

Seldén in their design work.

The main task of the thesis was to find a consistent method to model the laminate layup (produced by the filament winding method) in LUSAS. Focus has been on the stiffness and weight properties of the laminates. Model predictions were also benchmarked against practical bending tests. The proposed method was also to be converted into a short guideline for future use within the company.

To further increase the understanding of compressive failure in the carbon fibre mast, the out of plane waviness of the fibre was practically measured in laminates produced by Seldén. Waviness characteristics may then be used as input for models to more precisely predict the compressive strength. These studies were compared with practical compression tests performed during the project.

1.3 Limitations

A number of limitations were applied to the project from the start in order to focus the work better. The limitations are listed below.

- The modelling methods developed in this project will be specifically adapted to laminates produced with filament winding. No studies will be performed on laminates produced with other manufacturing methods.
- As requested by Seldén, FE-simulations will be performed exclusively with the FEA-software LUSAS, unless it is found to be insufficient for the needs of the project. This is due to the fact that LUSAS is the main FEA-software used at Seldén.
- Variations in the material system of the test specimen, i.e. the type of fibre or matrix, will not be evaluated. The production method and product quality is also fixed. Any optimisation suggestions will only be with regards to layup. One exception is in the case of low modulus fibre implementation where a separate kind of fibre will be used in the calculations.
- Compressive failure is the only failure mode that will be evaluated in this project. This is the dominant failure mode, together with buckling, that Seldén has identified as potential problems in their composite masts.
- Material data provided by Seldén will be used as far as possible.
- Many of the components that make up a complete mast (such as spreaders, boom brackets, mast step, head box etc.) will not be treated in this project since these components will have negligible or no effect on the stiffness of the mast. Hence only the bare mast without any additional components, sometimes referred to as the "tube", will be treated in this work. Neither will the full rigging (the mast together with sails, standing rigging, spreaders, boom, running rigging etc.) be discussed in any depth in this work. Both Larsson, Eliasson, and Orych (2014) and Bethwaite (2008) provide useful information on the subject of rigging types, rigging dynamics and rig design.

2 Theory

2.1 The mast

The mast is a main component of any sailing yacht, sailing dinghy or sailing boat, both present and historically. On a sailing vessel the mast can be considered as a cantilever beam, since during rigging it is common practice that pre-bend is introduced through shrouds, backstay and forestay. At the same time, due to the compressive loading introduced by the rigging the mast is also acting as a column. In both of these load configurations, acting at the same time, the stiffness of the mast is a main design parameter. To be able to control and predict the pre-bend during rigging and to prevent buckling during operation it is important to have an accurate prediction of the mast stiffness. Considering the equation of elastic behaviour of a pinned-end column in Equation (2.1) as well as the basic equation of bending of a beam in Equation (2.2) (Ugural & Fenster, 2011), both equations show that the bending stiffness EI, defined as the product of Young's modulus E times the cross-section area moment of inertia I, will have influence on both the buckling load P and deflection w of a beam subjected to bending. It is clear that bending stiffness is paramount when defining the characteristics of the mast.

$$EI\frac{\partial^2 w}{\partial x^2} + P_x w = 0 \tag{2.1}$$

$$\frac{\partial^2}{\partial x^2}\left(EI\frac{\partial^2 w}{\partial x^2}\right) = q_z \tag{2.2}$$

In Figure 2.1 the outline of a typical mast section is presented. Key locations and their names are marked with arrows. The arrows mark the locations of the fore-line, aft-line and B-lines. These lines run vertically along the length of the mast. The fore-line marks the foremost position on the section, likewise the aft-line marks the aftmost position on the section. The B-lines mark the widest part of the section. These terms are internally accepted at Seldén and will be used throughout this project.

Figure 2.1 also defines the orientation of axes where x runs from port to starboard while y runs from aft to fore. While z runs along the length of the mast. This orientation is to be employed throughout this entire project. Bending from aft to fore, i.e bending stiffness around the x-axis, will be denoted EI_x. Bending stiffness around the y-axis, EI_y will be related to the bending from port to starboard.

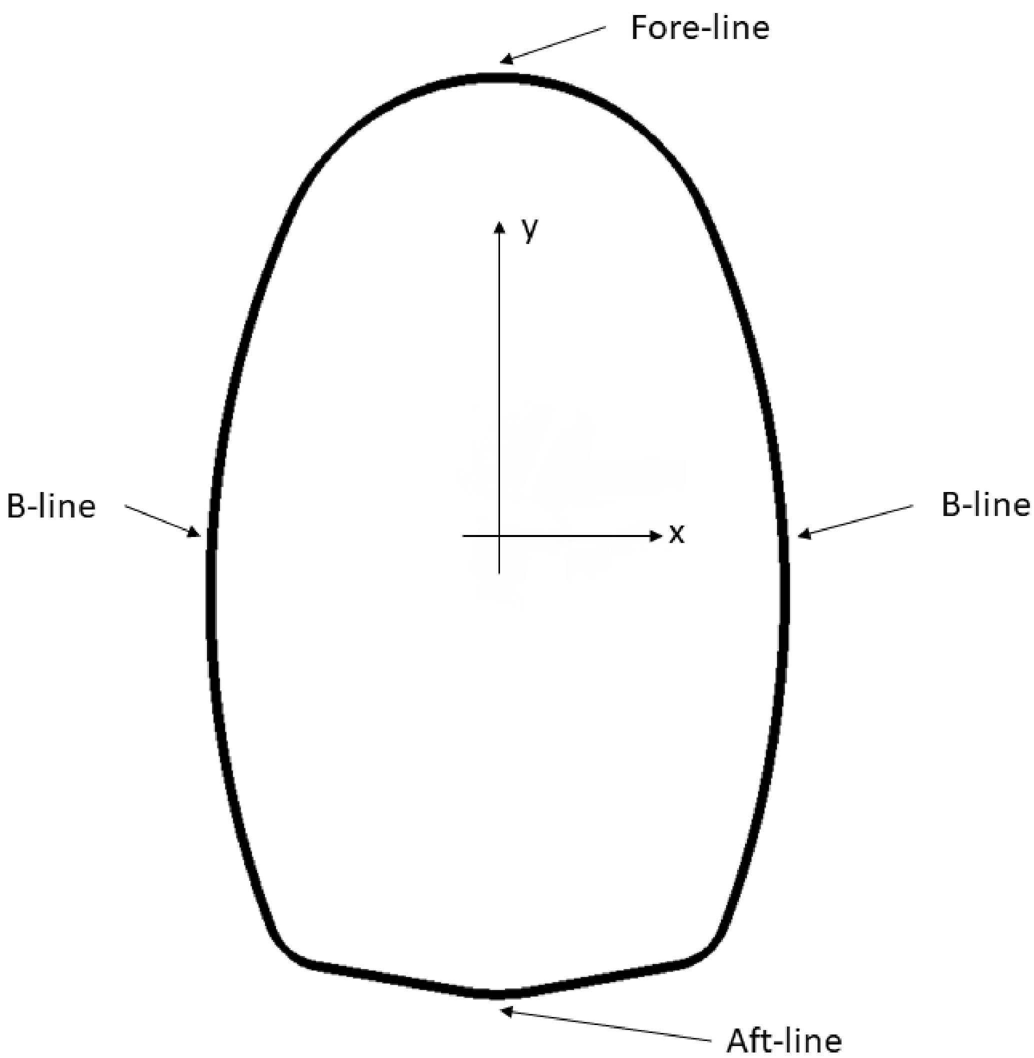

Figure 2.1: Outline of a typical mast section

2.2 Composite laminates

The material from which the masts in this project is made of is a composite laminate. Composite in the sense that two (or more) constituent materials are mixed to form a new material, with the mixed properties of its constituents. Laminate in the sense that several thin layers, also known as plies, of composite material are stacked in sequence to form a laminate with the combined properties of all its plies. In short, several plies stacked in sequence make up a laminate. The plies are in turn made up of several constituents, that make up each ply.

In this specific case, the composite is a carbon fibre reinforced plastic (CFRP). Continuous, unidirectional carbon fibres are embedded in a matrix. The matrix, also known as the resin being a thermosetting polymer bonds the fibres together. In Figure 2.2 the schematics of a single CFRP ply is shown. The Cartesian coordinate system 123 is oriented so that the 1-axis is parallel to the unidirectional fibres of the ply.

The plies are stacked in sequence to form the composite laminate shown in Figure 2.3. By orienting the plies, desired properties of the lamina can be achieved.

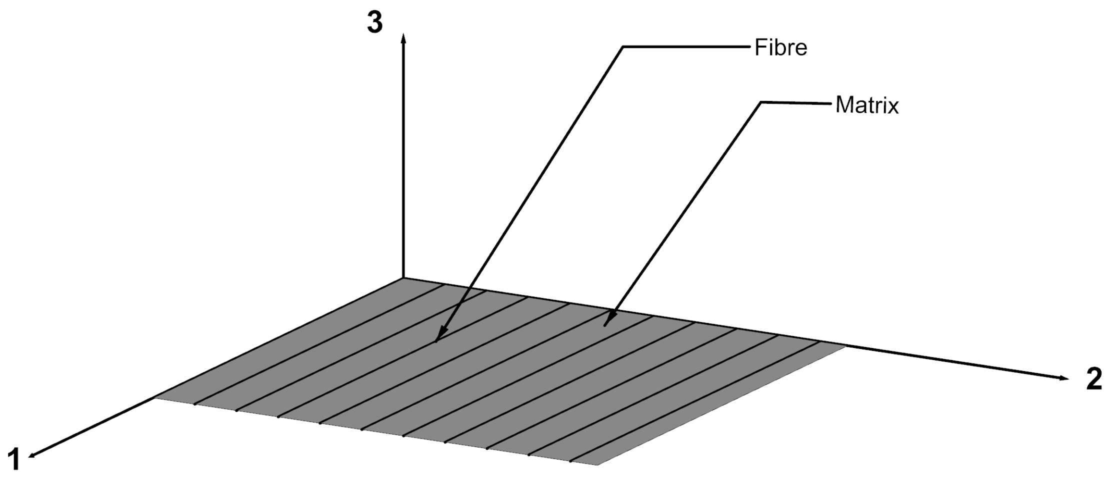

Figure 2.2: Fibre reinforced composite ply

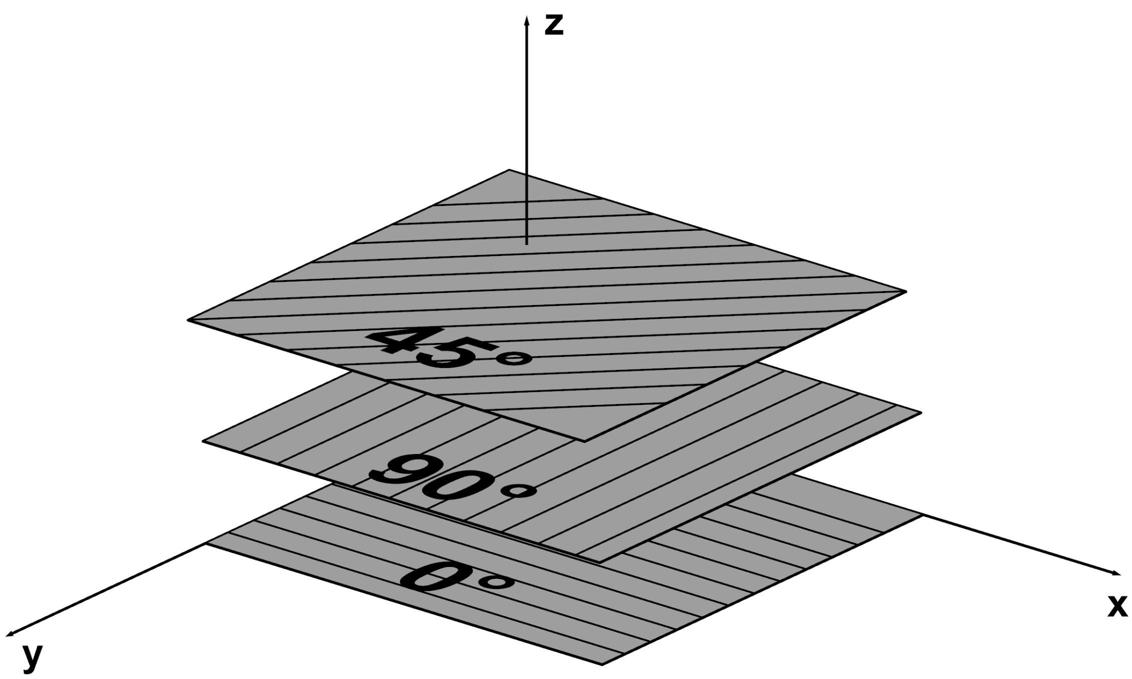

Figure 2.3: Composite laminate

2.2.1 Material properties

The fibre composite falls under the category of specially orthotropic materials. Unlike isotropic materials that exhibits symmetry of the elastic properties in all three planes, the orthotropic material is symmetric with respect to two planes. In the case of fibre composites the symmetry exists around two orthogonal planes, so that the elastic properties does not change when the axis perpendicular to the planes are reversed (Agarwal, Broutman, & Chandrashekhara, 2017).

In addition to this, the fibre composite is often considered to be a transversely isotropic material. Meaning that the 23 plane is a plane of isotropy. The transversely isotropic material has five independent elastic constants. In Equation (2.3) the stiffness matrix of a specially orthotropic, transversely isotropic material can be seen (Agarwal et al., 2017).

$$\begin{Bmatrix} \sigma_1 \\ \sigma_2 \\ \sigma_3 \\ \tau_{23} \\ \tau_{13} \\ \tau_{12} \end{Bmatrix} = \begin{bmatrix} C_{11} & C_{12} & C_{12} & 0 & 0 & 0 \\ C_{12} & C_{22} & C_{23} & 0 & 0 & 0 \\ C_{12} & C_{23} & C_{22} & 0 & 0 & 0 \\ 0 & 0 & 0 & \frac{C_{22}-C_{23}}{2} & 0 & 0 \\ 0 & 0 & 0 & 0 & C_{66} & 0 \\ 0 & 0 & 0 & 0 & 0 & C_{66} \end{bmatrix} \begin{Bmatrix} \epsilon_1 \\ \epsilon_2 \\ \epsilon_3 \\ \gamma_{23} \\ \gamma_{13} \\ \gamma_{12} \end{Bmatrix} \tag{2.3}$$

If the laminate is in plane stress conditions the out of plane stress components are zero

$$\sigma_3 = \tau_{23} = \tau_{13} = 0 \tag{2.4}$$

Thus, the stiffness matrix in the stress-strain relation of Equation (2.3) can be simplified to

$$\begin{Bmatrix} \sigma_1 \\ \sigma_2 \\ \tau_{12} \end{Bmatrix} = \begin{bmatrix} Q_{11} & Q_{12} & 0 \\ Q_{12} & Q_{22} & 0 \\ 0 & 0 & Q_{66} \end{bmatrix} \begin{Bmatrix} \epsilon_1 \\ \epsilon_2 \\ \gamma_{12} \end{Bmatrix} \tag{2.5}$$

where the new stiffness coefficients are defined in Equations (2.6).

$$\begin{aligned} Q_{11} &= C_{11} - \frac{C_{13}^2}{C_{33}} \\ Q_{22} &= C_{22} - \frac{C_{23}^2}{C_{33}} \\ Q_{12} &= C_{12} - \frac{C_{13}C_{23}}{C_{33}} \\ Q_{66} &= C_{66} \end{aligned} \tag{2.6}$$

Since the combined material properties of a laminate will be dependent on the orientation of the plies of which the laminate is made up from, it is necessary to refer the stress and strain of the plies to a common coordinate system. The transformation of stresses from the local coordinate system 123 of the ply into the global coordinate system XYZ can be seen in Equation (2.7) (Agarwal et al., 2017).

$$\begin{Bmatrix} \sigma_x \\ \sigma_y \\ \tau_{xy} \end{Bmatrix} = \begin{bmatrix} \boldsymbol{T_1} \end{bmatrix}^{-1} \begin{Bmatrix} \sigma_1 \\ \sigma_2 \\ \tau_{12} \end{Bmatrix} \tag{2.7}$$

$\boldsymbol{T_1}^{-1}$ is the inverse of the stress transformation matrix $\boldsymbol{T_1}$ seen in Equation (2.8), where θ is the orientation of the ply in relation to the global coordinate system XYZ.

$$[\boldsymbol{T_1}] = \begin{bmatrix} \cos^2\theta & \sin^2\theta & 2\sin\theta\cos\theta \\ \sin^2\theta & \cos^2\theta & -2\sin\theta\cos\theta \\ -\sin\theta\cos\theta & \sin\theta\cos\theta & \cos^2\theta - \sin^2\theta \end{bmatrix} \tag{2.8}$$

Likewise, with the strain transformation matrix $\boldsymbol{T_2}$ in Equation (2.9), the strains can be transformed from 123 to XYZ according to Equation (2.10).

$$[\boldsymbol{T_2}] = \begin{bmatrix} \cos^2\theta & \sin^2\theta & \sin\theta\cos\theta \\ \sin^2\theta & \cos^2\theta & -\sin\theta\cos\theta \\ -2\sin\theta\cos\theta & 2\sin\theta\cos\theta & \cos^2\theta - \sin^2\theta \end{bmatrix} \tag{2.9}$$

$$\begin{Bmatrix} \epsilon_x \\ \epsilon_y \\ \gamma_{xy} \end{Bmatrix} = \Big[\boldsymbol{T_2}\Big]^{-1} \begin{Bmatrix} \epsilon_1 \\ \epsilon_2 \\ \gamma_{12} \end{Bmatrix} \tag{2.10}$$

Substituting Equation (2.7) and (2.10) into (2.5) gives Equation (2.11).

$$\begin{Bmatrix} \sigma_x \\ \sigma_y \\ \tau_{xy} \end{Bmatrix} = [\boldsymbol{T_1}]^{-1} \begin{bmatrix} Q_{11} & Q_{12} & 0 \\ Q_{12} & Q_{22} & 0 \\ 0 & 0 & Q_{66} \end{bmatrix} [\boldsymbol{T_2}] \begin{Bmatrix} \epsilon_x \\ \epsilon_y \\ \gamma_{xy} \end{Bmatrix} \tag{2.11}$$

Thus, the elastic properties of the ply can be related to the global coordinate system. For the sake of simplicity Equation (2.11) is usually expressed as Equation (2.12) where $\bar{\boldsymbol{Q}}$ is given by Equation (2.13).

$$\begin{Bmatrix} \sigma_x \\ \sigma_y \\ \tau_{xy} \end{Bmatrix} = [\bar{\boldsymbol{Q}}] \begin{Bmatrix} \epsilon_x \\ \epsilon_y \\ \gamma_{xy} \end{Bmatrix} \tag{2.12}$$

$$[\bar{\boldsymbol{Q}}] = [\boldsymbol{T_1}]^{-1}[\boldsymbol{Q}][\boldsymbol{T_2}] \tag{2.13}$$

2.2.2 Analysis of the orthotropic laminate

The state of strain in a composite laminate can be described in terms of mid-plane strain and plate curvature of the laminate. The relation between total strain, mid-plane strain and plate curvature is given by Equation 2.14 (Agarwal et al., 2017).

$$\begin{Bmatrix} \epsilon_x \\ \epsilon_y \\ \gamma_{xy} \end{Bmatrix} = \begin{Bmatrix} \epsilon_x^0 \\ \epsilon_y^0 \\ \gamma_{xy}^0 \end{Bmatrix} + z \begin{Bmatrix} k_x \\ k_y \\ k_{xy} \end{Bmatrix} \tag{2.14}$$

Where z is the coordinate through the thickness of the laminate. It can be seen that the strain will vary linearly through the thickness of the laminate. This is due to the assumption that plies does not slip in relation to each other (Agarwal et al., 2017). By substituting Equation (2.14) into Equation (2.12) the state of stress in the i:th ply of a laminate is given by Equation (2.15).

$$\begin{Bmatrix} \sigma_x \\ \sigma_y \\ \tau_{xy} \end{Bmatrix}_i = [\bar{\boldsymbol{Q}}]_i \begin{Bmatrix} \epsilon_x^0 \\ \epsilon_y^0 \\ \gamma_{xy}^0 \end{Bmatrix} + z[\bar{\boldsymbol{Q}}]_i \begin{Bmatrix} k_x \\ k_y \\ k_{xy} \end{Bmatrix} \tag{2.15}$$

It is clear that stress in the ply will be dependent on the direction θ of the ply stiffness matrix $\bar{\boldsymbol{Q}}_i$. Stress will vary linearly within the thickness of each ply. However, across the laminate thickness, and across adjacent plies, the stress gradient will be discontinuous due to the differing directional properties of the plies.

With the stresses in the ply, the forces and moments acting on the cross-section of the i:th ply can be obtained by integrating over the thickness of the ply according to (Agarwal et al., 2017).

$$\begin{Bmatrix} N_x \\ N_y \\ N_{xy} \end{Bmatrix}_i = \int_{h_{i-1}}^{h_i} \begin{Bmatrix} \sigma_x \\ \sigma_y \\ \tau_{xy} \end{Bmatrix}_i dz \tag{2.16}$$

$$\begin{Bmatrix} M_x \\ M_y \\ M_{xy} \end{Bmatrix}_i = \int_{h_{i-1}}^{h_i} \begin{Bmatrix} \sigma_x \\ \sigma_y \\ \tau_{xy} \end{Bmatrix}_i zdz \tag{2.17}$$

The total forces and moments acting on the cross-section of the entire laminate are obtained by summing the contribution from all n plies.

$$\begin{Bmatrix} N_x \\ N_y \\ N_{xy} \end{Bmatrix} = \sum_{i=1}^{n} \begin{Bmatrix} N_x \\ N_y \\ N_{xy} \end{Bmatrix}_i = \sum_{i=1}^{n} \int_{h_{i-1}}^{h_i} \begin{Bmatrix} \sigma_x \\ \sigma_y \\ \tau_{xy} \end{Bmatrix}_i dz \tag{2.18}$$

$$\begin{Bmatrix} M_x \\ M_y \\ M_{xy} \end{Bmatrix} = \sum_{i=1}^{n} \begin{Bmatrix} M_x \\ M_y \\ M_{xy} \end{Bmatrix}_i = \sum_{i=1}^{n} \int_{h_{i-1}}^{h_i} \begin{Bmatrix} \sigma_x \\ \sigma_y \\ \tau_{xy} \end{Bmatrix}_i zdz \tag{2.19}$$

By substituting Equation (2.15) into (2.18) and (2.19), the relation between forces and moments acting on the laminate, and the mid-plane strain and plate curvature of the laminate is obtained.

$$\begin{Bmatrix} N_x \\ N_y \\ N_{xy} \end{Bmatrix} = \sum_{i=1}^{n} \int_{h_{i-1}}^{h_i} \left([\bar{\boldsymbol{Q}}]_i \begin{Bmatrix} \epsilon_x^0 \\ \epsilon_y^0 \\ \gamma_{xy}^0 \end{Bmatrix} + z[\bar{\boldsymbol{Q}}]_i \begin{Bmatrix} k_x \\ k_y \\ k_{xy} \end{Bmatrix} \right) dz \tag{2.20}$$

$$\begin{Bmatrix} M_x \\ M_y \\ M_{xy} \end{Bmatrix} = \sum_{i=1}^{n} \int_{h_{i-1}}^{h_i} \left([\bar{\boldsymbol{Q}}]_i \begin{Bmatrix} \epsilon_x^0 \\ \epsilon_y^0 \\ \gamma_{xy}^0 \end{Bmatrix} + z[\bar{\boldsymbol{Q}}]_i \begin{Bmatrix} k_x \\ k_y \\ k_{xy} \end{Bmatrix} \right) zdz \tag{2.21}$$

From Equation (2.20) and (2.21) three new matrices $\boldsymbol{A}$, $\boldsymbol{B}$ and $\boldsymbol{D}$ can be defined as Equations (2.22) to (2.24)

$$[\boldsymbol{A}] = \sum_{i=1}^{n} \int_{h_{i-1}}^{h_i} [\bar{\boldsymbol{Q}}]_i dz = \sum_{i=1}^{n} [\bar{\boldsymbol{Q}}]_i (h_i - h_{i-1}) \tag{2.22}$$

$$[\boldsymbol{B}] = \sum_{i=1}^{n} \int_{h_{i-1}}^{h_i} [\bar{\boldsymbol{Q}}]_i z dz = \frac{1}{2} \sum_{i=1}^{n} [\bar{\boldsymbol{Q}}]_i (h_i^2 - h_{i-1}^2) \tag{2.23}$$

$$[\boldsymbol{D}] = \sum_{i=1}^{n} \int_{h_{i-1}}^{h_i} [\bar{\boldsymbol{Q}}]_i z^2 dz = \frac{1}{3} \sum_{i=1}^{n} [\bar{\boldsymbol{Q}}]_i (h_i^3 - h_{i-1}^3) \tag{2.24}$$

The constitutive equations (Equations (2.20) and (2.21)) of the laminate are simplified and condensed in to Equation (2.25).

$$\begin{Bmatrix} N_x \\ N_y \\ N_{xy} \\ M_x \\ M_y \\ M_{xy} \end{Bmatrix} = \begin{bmatrix} A_{11} & A_{12} & A_{16} & B_{11} & B_{12} & B_{16} \\ A_{12} & A_{22} & A_{26} & B_{12} & B_{22} & B_{26} \\ A_{16} & A_{26} & A_{66} & B_{16} & B_{26} & B_{66} \\ B_{11} & B_{12} & B_{16} & D_{11} & D_{12} & D_{16} \\ B_{12} & B_{22} & B_{26} & D_{12} & D_{22} & D_{26} \\ B_{16} & B_{26} & B_{66} & D_{16} & D_{26} & D_{66} \end{bmatrix} \begin{Bmatrix} \epsilon_x^0 \\ \epsilon_y^0 \\ \gamma_{xy}^0 \\ k_x \\ k_y \\ k_{xy} \end{Bmatrix} \tag{2.25}$$

Forces are related to the mid-plane strains through the extensional stiffness matrix $\boldsymbol{A}$. Moments are on the other hand related to plate curvature through the bending stiffness matrix $\boldsymbol{D}$. The coupling stiffness matrix $\boldsymbol{B}$ defines the coupling between forces and plate curvature as well as the coupling between moments and mid-plane strains. For a non-zero coupling matrix, this implies that normal and shear forces, in addition to mid-plane strains, will cause the laminate to twist and bend. While moments will cause mid-plane strains in addition to bending and twisting. (Agarwal et al., 2017)

2.2.3 Application to beam theory

To be able to apply the the classical laminate theory presented in the previous section on a laminated cantilever beam, a number of assumptions and simplifications have to be made (Hajianmaleki & Qatu, 2011) (Agarwal et al., 2017). These assumptions and simplifications may not be applicable on the masts analysed in this project, at least not with satisfactory results. Still, the derivation presented here may provide insight on how the stiffness coefficients in Equation (2.25) relates to the stiffness of a mast.

Consider a laminated cantilever beam of length L and width b, loaded so that the resultant forces and moments are according to Equations (2.26) and (2.27).

$$N_y = N_{xy} = 0 \tag{2.26}$$

$$M_y = M_{xy} = 0 \tag{2.27}$$

In addition to the above assumption, if Poisson's effect, shear deformations and twisting curvature of the beam mid surface are neglected so that they are 0, Equation (2.25) can be reduced to Equation (2.29) (Hajianmaleki & Qatu, 2011).

$$\epsilon_y^0 = \gamma_{xy}^0 = k_y = k_{xy} = 0 \tag{2.28}$$

$$\begin{Bmatrix} N_x \\ M_x \end{Bmatrix} = \begin{bmatrix} A_{11} & B_{11} \\ B_{11} & D_{11} \end{bmatrix} \begin{Bmatrix} \epsilon_x^0 \\ k_x \end{Bmatrix} \tag{2.29}$$

It is assumed that the beam is long and slender $L >> b$, so that the stresses and displacements can be considered constant across the width of the beam (Agarwal et al., 2017). Thus, the width b can be included in Equation (2.29).

$$\begin{Bmatrix} N_x b \\ M_x b \end{Bmatrix} = \begin{bmatrix} bA_{11} & bB_{11} \\ bB_{11} & bD_{11} \end{bmatrix} \begin{Bmatrix} \epsilon_x^0 \\ k_x \end{Bmatrix} \tag{2.30}$$

The equations of motion gives the external forces per unit length acting on the beam in the x and z directions, q_x and q_z respectively.

$$\begin{aligned} -q_x &= \frac{\partial}{\partial x}(N_x b) \\ -q_z &= \frac{\partial^2}{\partial x^2}(M_x b) \end{aligned} \tag{2.31}$$

Inserting Equation (2.31) into (2.30) yields

$$\begin{aligned} -q_x &= \frac{\partial}{\partial x}(N_x b) = \frac{\partial}{\partial x}\left(bA_{11}\epsilon^0 + bB_{11}k_x\right) \\ -q_z &= \frac{\partial^2}{\partial x^2}(M_x b) = \frac{\partial^2}{\partial x^2}\left(bB_{11}\epsilon^0 + bD_{11}k_x\right) \end{aligned} \tag{2.32}$$

Mid plane strain and curvature of the beam middle surface are given by

$$\begin{aligned} \epsilon_x^0 &= \frac{\partial u_0}{\partial x} \\ k_x &= -\frac{\partial^2 w}{\partial x^2} \end{aligned} \tag{2.33}$$

Where u is the extension along x and w is the deflection of the beam. Substituting Equation (2.33) into Equation (2.32) gives that

$$\begin{aligned} -q_x &= \frac{\partial}{\partial x}(N_x b) = \frac{\partial}{\partial x}\left(bA_{11}\frac{\partial u_0}{\partial x} - bB_{11}\frac{\partial^2 w}{\partial x^2}\right) \\ -q_z &= \frac{\partial^2}{\partial x^2}(M_x b) = \frac{\partial^2}{\partial x^2}\left(bB_{11}\frac{\partial u_0}{\partial x} - bD_{11}\frac{\partial^2 w}{\partial x^2}\right) \end{aligned} \tag{2.34}$$

Equation (2.34) gives two differential equations with the two unknowns extension and deflection of the beam, u and w respectively. The differential equations can be written as

$$\begin{aligned} bA_{11}\frac{\partial^2 u_0}{\partial x^2} - bB_{11}\frac{\partial^3 w}{\partial x^3} &= -q_x \\ bB_{11}\frac{\partial^3 u_0}{\partial x^3} - bD_{11}\frac{\partial^4 w}{\partial x^4} &= -q_z \end{aligned} \tag{2.35}$$

Different loading and boundary conditions can be applied in Equation (2.35) when finding the solutions for u and w, in this case the coupling between bending and extension will be included.

If it instead is assumed that the laminate of the beam is such that the coupling stiffness matrix is zero $\boldsymbol{B} = \boldsymbol{0}$, i.e a symmetrical laminate. And no axial load of the beam is present, $q_x = 0$. Equation (2.34) can be simplified to

$$\frac{\partial^2}{\partial x^2}\left(bD_{11}\frac{\partial^2 w}{\partial x^2}\right) = q_z \tag{2.36}$$

The similarity with Equation (2.2) is obvious. The bending stiffness of the laminated beam is governed by bD_{11} much like the bending stiffness of an ordinary beam is governed by EI. If this reasoning is applied to a pinned-end column, the equation of elastic behaviour will become (Agarwal et al., 2017)

$$bD_{11}\frac{\partial^2 w}{\partial x^2} + P_x w = 0 \tag{2.37}$$

The assumptions made to arrive at Equations (2.36) and (2.37) renders the application of these equations to be restricted, making it necessary to perform the analysis of mast stiffness through the use of FE-software in this project.

2.2.4 Calculation of hybrid laminate properties

Seldén has incorporated a method of mixing different types of fibres in some of their products, creating what is referred to in this report as a hybrid laminate. This laminate will have a new set of properties based on the individual properties of the different fibres.

The hybrid laminate evaluated is a combination of glass and carbon fibres. The material properties for each separate material are known through previous material testing performed by Seldén. However, no testing has been performed on the hybrid material. The hybrid material properties therefore need to be calculated. Equation 2.38 was used for this purpose. An initial calculation to get a reference value produced the values shown in Table 2.1, where the hybrid Young's modulus was simply calculated as the mean of the carbon and glass composites' Yong's modulus.

A more detailed calculation of the Young's modulus can also be done based on the filament properties of the different tows. Data found online for the carbon fibre and glass fibre tows respectively give the information shown in Table 2.2.

Table 2.1: Hybrid laminate constituents properties

	Young's modulus [GPa]	Volume fraction[1]
T700 Carbon composite	-	-%
E-glass composite	43	-%
Hybrid composite	-	

Table 2.2: Properties of the different tows of the hybrid laminate

	T700 Carbon fibre tow (T700SC-12K-60E)	E-glass fibre tow (158B-AB-450)
Number of filaments	12000	2000
Filament diameter [μm]	7	16.4
Resin content (RC)	0.32	0.25

By measuring the tow cross-section area, it is possible to calculate the actual ratio between the tow composites. The total tow area of each composite can be calculated using Equation (2.38) assuming the area fraction A_f is equal to the volume fraction $V_f = 1-RC$.

$$A_{tow} = \frac{A_{filament} \times n_{filament}}{1 - RC} \tag{2.38}$$

The actual ratio between carbon and glass fibres is then found to be the ratios stated in Table 2.3 together with the actual theoretical Young's modulus.

Table 2.3: Hybrid laminate

	Young's modulus [GPa]	Actual volume fraction[1]
T700 Carbon composite	-	-%
E-glass composite	43	-%
Hybrid composite	-	

It is seen that the difference between the simplified Young's modulus and the theoretically correct one is small. The Young's modulus shown in Table 2.3 is the one that has been used in the hybrid laminate FE-simulations covered in Section 5.1.3.

2.3 Filament winding

The chosen production method for the composite masts at Seldén Mast is that of filament winding. Traditionally, filament winding is used for rotationally symmetric objects and is commonly used in the production of pressure vessels and tubes. The object is produced by winding fibres and resin onto a rotating mandrel. The fibres can either be pre-impregnated with resin (pre-preg) or led through a resin bath before being wound onto the mandrel. The fibres are deployed to the mandrel via a carrier running back and forth along the length of the mandrel. An image showing the resulting wind pattern as well as the fibre application is shown in Figure 2.4. The fibre angle and placement is controlled by varying the speed with which the carrier traverses the mandrel. The process is most often

[1] Sensitive information has been censored in the published version of this thesis.

numerically controlled which allows for a highly controllable process and a final result of consistent quality (Agarwal et al., 2017).

Figure 2.4: A carbon fibre mast during production. Photograph courtesy of Seldén Mast Ltd.

2.3.1 Filament winding at Seldén

An exception to the process described above is when the product is not rotationally symmetric, as in the case of most larger sail boat masts. A normal mast cross-section has more of an oval shape such as the one previously shown in Figure 2.1, which leads to some deviations in the final result compared to circular cross-sections.

The deviations in fibre angle can be derived from the fact that the winding machine at Seldén treats the mast as a tube with a circular cross-section, and a fixed nominal radius, while the actual mast will have a varying radius from the centre of rotation to the surface of the fibres. An example of this is shown in Figure 2.5. It is not entirely clear how the nominal radius is chosen in production, but it is assumed to be equal to or larger than the maximum distance from the centre of the mandrel.

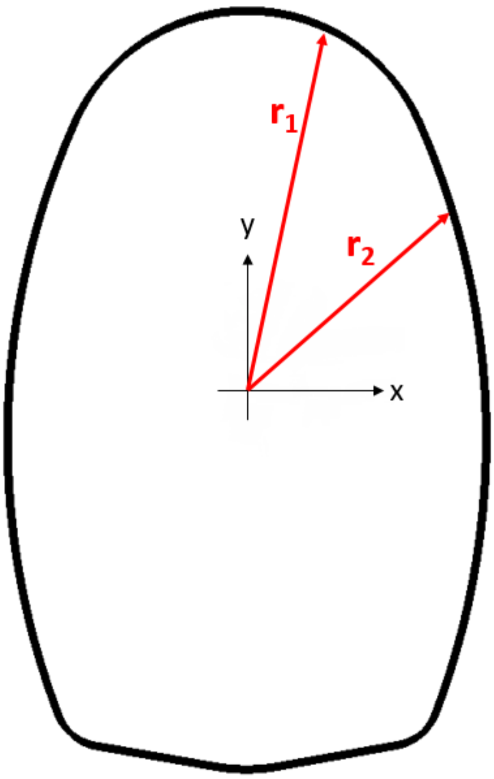

Figure 2.5: Illustration of the varying radius of a mast section.

When studying existing literature about filament winding, little is written about the winding of non-circular geometries. The effects of the geometry on the fibre misalignment is therefore largely unknown.

2.4 Effect of fibre out of plane waviness on compressive strength

In Fleck (1991) it is stated that fibre kinking, also referred to as micro buckling even though it has been proved not to be caused by instability, is the dominant compressive failure mechanism of a fibre composite. The fibre kinking is initiated by an initial out of plane misalignment of the fibre (Shu & Fleck, 1997). The kinking failure mechanism is governed by the ability of the matrix to support the fibres under compressive loading. Thus the shear limit τ of the resin, together with the magnitude of the initial fibre misalignment angle will be the governing parameters of fibre kinking. A failure criteria for fibre kinking was formulated by Argon as a ratio between the shear yield limit τ and the initial fibre misalignment angle θ Argon (1972).

$$X_c = \frac{\tau}{\theta} \tag{2.39}$$

It was shown by Wilhelmsson, Gutkin, Edgren, and Asp (2018) that it is possible to measure the fibre misalignment θ through image analysis of micrographs of the fibre composite.

The measured maximum misalignment angle can then be used as input in Equation (2.39) to predict the compressive strength of the composite. In the work of Wilhelmsson et al. (2018) a method of characterising the fibre out of plane waviness was developed. The method was applied to non crimp fabric (NCF) composites. The definition of NCF composites is covered in the work of Lomov (2011). In this project, the same method will be applied to characterise the out of plane waviness of the filament wound composite.

2.5 Effect of fibre out of plane waviness on stiffness

Wilhelmsson, Asp, Gutkin, and Edgren (n.d.) found a correlation between reduced stiffness and the magnitude of fibre out of plane waviness during compressive loading. This reduction was formulated as a knock down factor η.

$$\eta = \left(1 - \frac{E_{exp}}{E_{ROM}}\right) \times 100 \tag{2.40}$$

In Equation (2.40) the experimentally measured stiffness E_{exp} is compared to the stiffness predicted by the rule of mixtures (ROM) E_{ROM} (Agarwal et al., 2017). Wilhelmsson et al. (n.d.) approximated the stiffness reduction to approximately 7% per degree for the mean misalignment angle.

3 Material specifications

A critical part of any FE analysis is accurate material data in order for the model being evaluated to give results that are as close to reality as possible.

3.1 Carbon Fibre Laminate Properties

The composite material properties of the carbon fibre laminate are given by Seldén and are presented in Table 3.1. The material data was supplied from the Seldén office in England, Seldén Mast Ltd., usually referred to as SML. It is still unclear how the material data was obtained. Note that the value for G_{23} is missing. The corresponding value shown in Table 3.2[2] has been used for both datasets in calculations and simulations.

Table 3.1: T700SC/UF3325 TCR Composite material properties

	[GPa]		[-]		$[t/mm^3]$
E_1	-	ν_{12}	-	ρ	-
E_2	-	ν_{13}	-		
E_3	-	ν_{23}	-		
G_{12}	-	V_f	-		
G_{13}	-				
G_{23}	-				

This data can be compared to the calculated data based on the suppliers' data sheets, shown in Table 3.2.

Table 3.2: T700SC/UF3325 TCR Composite material properties, calculated using Suppliers' data.

	[GPa]		[-]		$[t/mm^3]$
E_1	157	ν_{12}	0.164	ρ	1.61E-9
E_2	19	ν_{13}	0.164		
E_3	19	ν_{23}	0.40		
G_{12}	3.33	V_f	0.68		
G_{13}	3.33				
G_{23}	6.78				

[2]Sensitive information has been censored in the published version of this thesis

4 Methods

The methods used in the project vary between the different research fields. It is composed of a combination of computer modelling and practical tests. The following sections will give a detailed description of the computer modelling and test methods used.

4.1 Modelling stiffness of circular cross-sections

The stiffness modelling of circular cross-sections is performed by the use of FE-simulations, where the development of the FE-modelling method is developed using benchmark tests as references, most of which are made on two types of spinnaker poles. The method is then tested on a third tube produced with a hybrid laminate of glass and carbon fibres, in order to see if the method is applicable also in that case by the use of modified material properties.

4.1.1 Benchmarking bend tests of spinnaker poles

In this work, the tests have been performed using equipment available at Seldén. The size of the test specimens make it difficult or impossible to use conventional test rigs for three-point bend tests. Therefore, it was decided that a non-conventional testing method is to be applied. The schematics of the test can be seen in Figure 4.1. The same test setup is used for both pole 39 and pole 88. The pole is simply supported with a concentrated force F located at the middle of the span. During the tests the deflection is measured at 5 locations (AL, BL, C, BR and AR) along the pole while the force F is gradually increased. The deflection is calculated by measuring the distance between the deflected pole and a laser beam positioned above the pole. It should be noted that points AL, AR and BL, BR are placed with equal distances from the midpoint C. This is done to verify the test results since theoretically, two points with equal distance from the mid-point should have identical deflection in three-point bending. The simply supported configuration is achieved by letting the pole rest in two slings attached to an overhead crane. By anchoring the midpoint of the pole to a forklift, load can be applied by moving the overhead crane in the vertical direction. The two slings are raised in a synchronised manner, thereby avoiding excessive tilting of the pole. A spring and a scale is connected between the forklift and the pole. The scale is used to measure the force applied by lifting the blocks, and thus also the slings, of the overhead crane. The deflection relative the laser beam can be measured with a ruler.

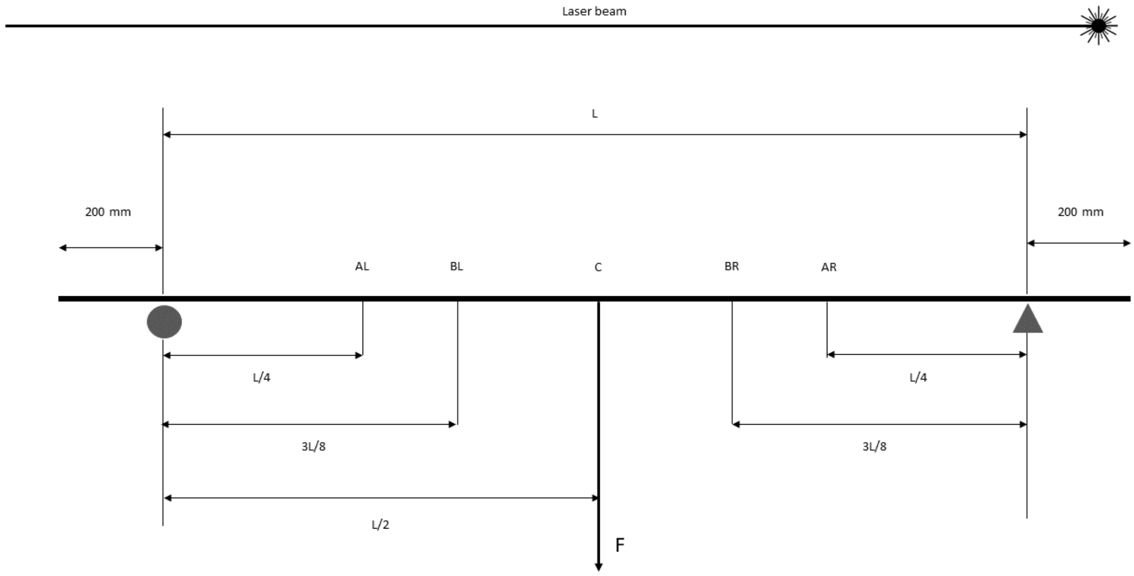

Figure 4.1: Schematic sketch of test setup

Figure 4.2 gives an overview of the test setup and the measuring procedure. The procedure is: as the blocks of the overhead crane are moved a distance Δz in the vertical direction, the scale reading is noted. This gives the force F, which the pole is loaded with at the mid-span. To get the deflection w of the pole under this load, the distances between the supports and the laser beam (z_{LS} and z_{RS}) are measured. By measuring these values, the distance z_0 between the laser beam and undeformed pole can be calculated by drawing a straight line between the two supports, marking the position of the undeformed pole, shown as a dashed line in Figure 4.2. Once the distance z_{laser} between the deformed pole and the laser beam is measured, the deflection of the pole is simply calculated using Equation (4.1).

$$w = z_{laser} - z_0 \tag{4.1}$$

Three point bending tests are performed on two different spinnaker poles, hereafter referred to as pole 39 and pole 88. Both spinnaker poles are produced by Seldén using the filament winding method. The principal dimension of the poles are presented in Table 4.1.

Table 4.1: Principal dimensions of the spinnaker poles

	Length [mm]	Outer diameter [mm]	Wall thickness [mm]
Pole 39	2600	39	1.5
Pole 88	4700	88	2.4

Both poles are filament wound with the T700SC fibre pre-preg to a fibre volume fraction of $V_f = 0.68$ with the UF3325 TCR resin, both produced by TORAY. The poles employ the layups presented in Table 4.2.

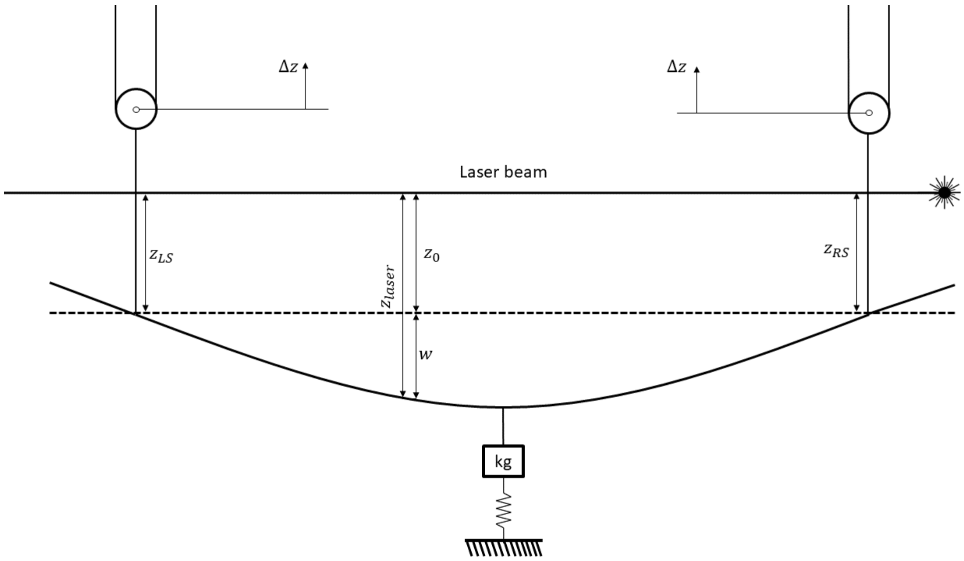

Figure 4.2: Test setup and measuring procedure.

Table 4.2: Spinnaker pole layups

	Layup[3]
pole 39	[−° −° −° −° −°]
pole 88	[−° −° −° −° −° −°]

4.1.2 Benchmarking bend test of hybrid laminate tube

As part of an internal quality control at Seldén bend tests had already been performed on the hybrid laminate tubes. It should be noted that these tests were not performed by the authors. However, the results were made available for the purpose of this project. The test consisted of letting the tube rest on two trestles, one at each end of the tube. A force is applied mid span of the simply supported mast. A principal sketch of the test setup is shown in Figure 4.3.

The overall length L_{OA}, the length of the span between the supports L_{span} and the force F located at the mid-span are presented in Table 4.3.

Table 4.3: Variables of the hybrid tube test.

L_{OA} [mm]	L_{span} [mm]	F [N]
3583	3540	245.5

In total, 53 identical hybrid laminate tubes were tested in this fashion. The deflection under the load specified above were measured at 1/4, 1/2 and at 3/4 of the free span. The average deflection and the standard deviation of all measured deflections are presented in Table 4.4 below.

The average deflection $\overline{w}$, is calculated using Equation (4.2) and the standard deviation σ_w according to Equation (4.3).

[3]Sensitive information has been censored in the published version of this thesis.

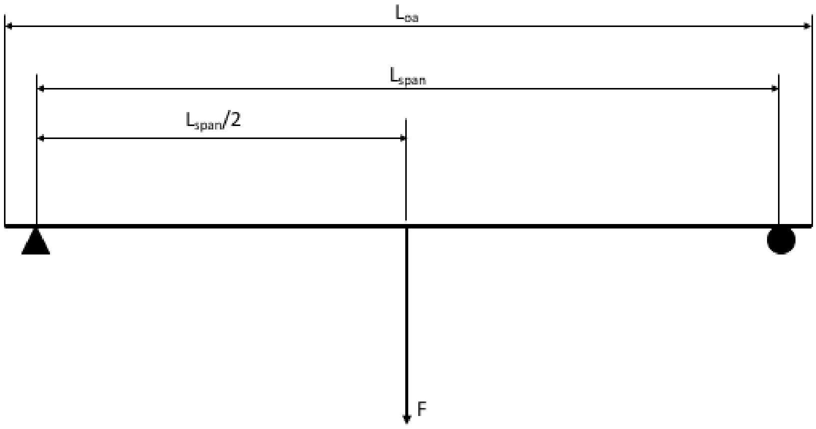

Figure 4.3: Test setup of hybrid laminate tube.

Table 4.4: Results of Seldén hybrid laminate tube tests.

	$L_{span}/4$	$L_{span}/2$	$3L_{span}/4$
$\overline{w}$ [mm]	26.3	38.5	26.3
σ_w [mm]	0.47	0.55	0.45

$$\overline{w} = \frac{1}{n}\sum_{i=1}^{n} w_i \tag{4.2}$$

$$\sigma_w = \sqrt{\frac{\sum\left(w_i - \overline{w}\right)^2}{(n-1)}} \tag{4.3}$$

The results in Table 4.4 are to be compared to a FE-model simulating the three-point bend test described in this section.

The hybrid tube, as the name suggests is made from a hybrid laminate. A hybrid laminate is defined in this project as a laminate composed of at least three material components, as opposed to the usual two. The evaluated hybrid laminate is composed of glass and carbon fibres together with a common matrix. Like the spinnaker poles the hybrid tube has a constant circular cross-section. The principal dimensions of the tube is presented in Table 4.5.

Table 4.5: Principal dimensions of the hybrid laminate tube

Length [mm]	Outer diameter [mm]	Wall thickness [mm]
3583	50	2.5

The hybrid laminate of the tube is arranged in the layup presented in Table 4.6.

Table 4.6: The layup of the hybrid laminate tube.

Hybrid laminate tube layup[4]
[–° –° –° –° –° –° –° –° –°]

4.1.3 Fibre angle measurement

An important property of any fibre reinforced laminate is the in-plane fibre orientation (angle). Every laminate is designed with a nominal fibre angle to optimise performance. This applies to Seldén's composite products as well. The actual fibre angle of a composite part may however differ from the nominal angle due to unintentional variations in production, which will affect the performance of the part.

One part of this project is to evaluate if there is a difference between nominal and actual fibre angle, and how large the difference is. If there is a difference, a fibre angle sensitivity check will be performed in LUSAS to see how large the loss in performance is.

The actual fibre angle of the circular tubes was measured by tracing tape along one of the fibre tows visible on the outside of the tube. A translucent sheet of plastic was then wrapped around the tube, showing the tape underneath. It was also made sure that the bottom edge of the sheet was perpendicular to the longitudinal axis of the tube when it was wrapped around the circumference. A line was then drawn on the paper, following the edge of the tape. The result is a diagonal line with the same angle relative to the bottom of the paper as the fibres have to the longitudinal axis of the tube.

A large set of coordinates were then measured along the diagonal coordinates, using the bottom of the sheet as the x-axis and the side edge as the y-axis. The measured coordinates were then used as input in Matlab for further analysis of the angle variation.

4.1.4 FE model

The FE-models are made entirely in the FE-software LUSAS provided by Finite Element Analysis Ltd. The poles are modelled as a surface making up a cylinder with constant circular cross-section. The surface is then meshed with an 8-noded thick shell element, QTS8 (LUSAS, 2017). The size of the elements is decided by conducting a convergence study on the smallest pole, where the element size is decreased incrementally. The result of the convergence study is shown in Figure 4.4. Based on the results, the element size was set to $15 \times 15\ mm$ in all models. Since the convergence study was performed on the smallest pole, it was decided that the element size was suitable for and would be used in all simulations for the sake of simplicity, even if it meant that the simulations would take slightly longer time to run. An illustration of the finnished FE-model can be seen on page 5 in Appendix B.

The supports are modelled as simple supports in a single point at the locations of the supports in the tests. The load is applied as a distributed force, on the top half of the cylinder on a single line located mid-span between the two supports. The type of supports was chosen since it best represented the actual setup used in the benchmarking tests.

[4]Sensitive information has been censored in the published version of this thesis.

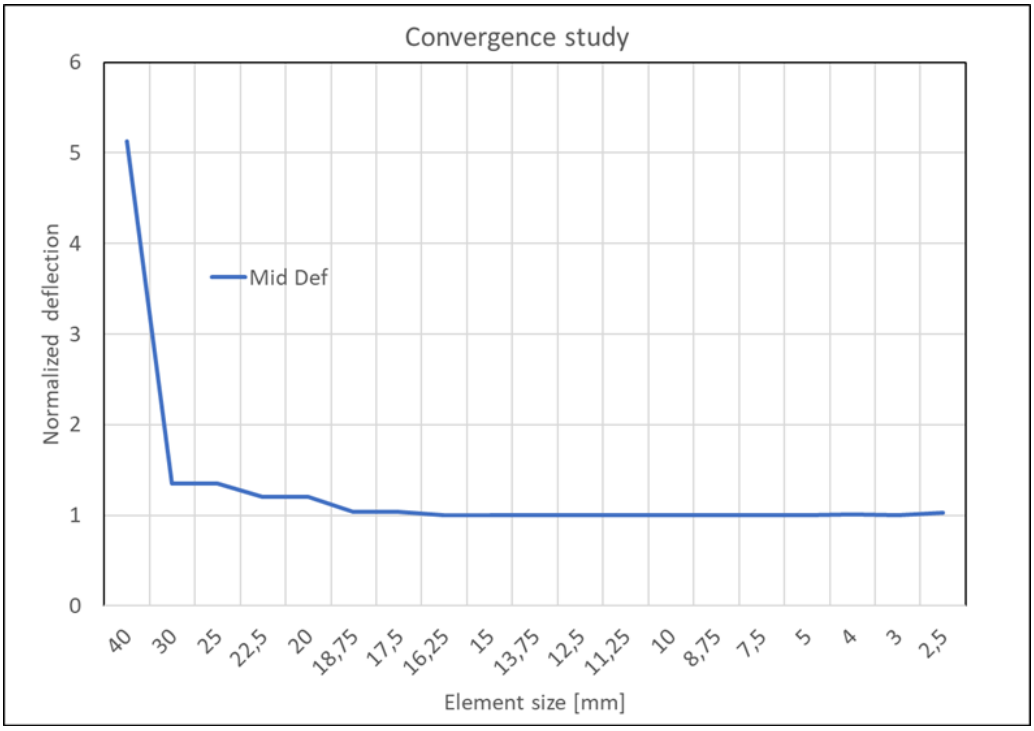

Figure 4.4: Convergence study of mesh element size.

To take any geometrical non-linearity into consideration the Total Lagrangian formulation is applied. A complete step by step guide describing how the modelling is performed can be found in Appendix B. This guide was written in conjunction to this project on request by Seldén.

4.1.5 Method for comparing model and tests

After the deflection has been measured in the test, linear regression is used to find the correlation between the applied load F and the deflection of the pole w. The midpoint deflection is of certain interest. Therefore, linear regression is performed on the test results, as well as the results of the LUSAS model covered in Section 4.1.4. The correlation coefficient is calculated using Equation (4.4).

$$\rho(w_{mid}, F) = \frac{1}{N-1} \sum_{i=1}^{N} \left(\frac{\overline{w_{mid,i} - \mu_{w_{mid}}}}{\sigma_{w_{mid}}} \right) \left(\frac{F_i - \mu_F}{\sigma_F} \right) \tag{4.4}$$

N is the number of data points, μ denotes a mean value and σ denotes a standard deviation. With the correlation coefficient ρ the inclination k of the straight line describing the relationship between load and mid-point deflection is found as Equation (4.5).

$$k = \rho \left(\frac{\sigma_{w_{mid}}}{\sigma_F} \right) \tag{4.5}$$

The mid-point deflection can now be approximated for any applied load, within reasonable limits, as the expression in Equation (4.6).

$$w_{mid,est} = kF \tag{4.6}$$

4.2 Modelling of non-circular cross-sections

The modelling of non-circular cross-sections follows the same procedure as for the circular cross-sections in general, with some specific problems arising from the irregular shape of the cross-sections. The masts are modelled in LUSAS and the results from the FE-models are compared to practical tests.

The irregular shape in combination with Seldén's choice of winding method will lead to variations in the manufactured mast, which in turn will affect the stiffness properties of the mast so that they differ from the intended properties. Major variations that have been observed in this project are:

- *Variations in fibre angle.* Since the mast has a non-circular cross-section the fibre angle of the laminate will vary around the circumference of the mast. In Section 4.2.2 it is explained how attempts to measure these variations are performed.
- *Over consolidation of corners.* Around sharp corners of the mast the thickness of the laminate is drastically decreased, as shown in Figure 4.5. This will have a geometric effect on the area moment of inertia of the section as well as the material properties of the laminate. Since no fibres have disappeared and the laminate is clearly thinner, it is reasoned that the volume fraction of the matrix is reduced.

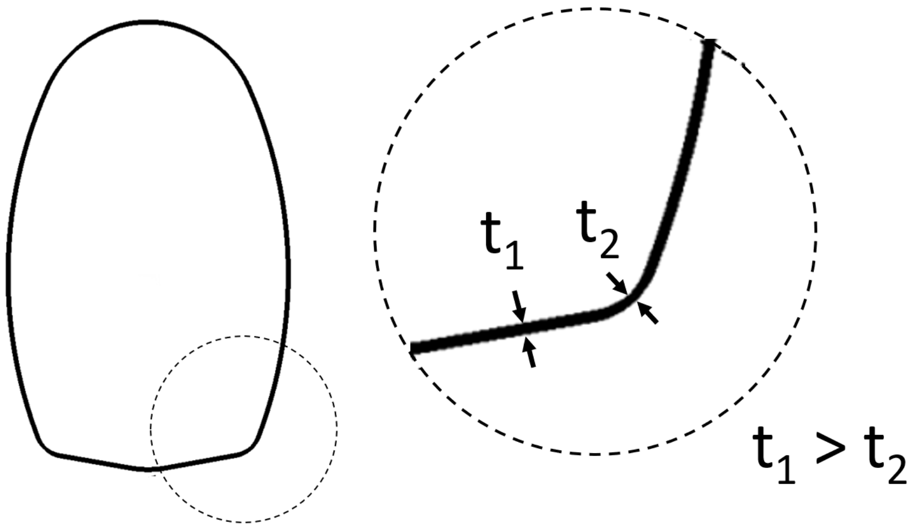

Figure 4.5: Over consolidation.

- *Fibre waviness.* Since the tows of fibres are overlapped in a diamond shaped pattern during the winding process, out of plane waviness of the fibres will occur. This is illustrated in Figure 4.6 where the waviness of a fibre comes as a result of the weaving.

All of the above mentioned variations will affect the stiffness properties of the mast.

Figure 4.6: Fibre waviness.

4.2.1 Benchmarking bend tests of masts

As part of the validation of the FE results, three different masts, all of which are in production and used on dinghies and larger sail boats, have been tested in bending. These tests have been performed at Seldén's carbon fibre mast production facilities in England. They have all been tested and modelled including reinforcements along the length of the masts. The principal dimensions of these masts are summarised in Table 4.7. L_{OA} denotes the overall length of the mast, L_{PA} is the parallel length of the mast, i.e the length where the cross-section is constant. L_{top} gives the length of the tapered section. The cross-section of the tapered part of the mast, tapers off from the nominal into the smallest cross-section at the very top of the mast. These variables and a rough sketch of a mast are shown in Figure 4.7.

Figure 4.7: Sketch of a mast.

Table 4.7: Principal dimensions of modelled masts

	L_{OA} [mm]	L_{PA} [mm]	L_{top} [mm]	t_{nom} [mm]	m [kg]
Sea Racer 35	16338	13973	2365	3.0	43.8
Farr 58	14662	11807	2855	6.6	124.0
J70	8910	6875	2035	2.4	11.7

The nominal wall thickness of the cross-section is given by t_{nom}. The variable m denotes the mass of the entire mast. The layups of the masts above are presented in Table 4.8.

The layups in Table 4.8 are the nominal layups. The Sea Racer 35 and J70 has UD tape reinforcements in the mast. The UD tapes are located at the B-lines, fore-line and aft-line of the mast. The UD tapes are added into the layup at these locations during the winding process. A summary of the reinforcements for each mast can be found in Table 4.9.

The masts were tested in three-point bending, with the masts resting on wooden trestles to achieve sharp and accurate support points. The tapered ends of the masts were put outside the supports in order to only test the deflection of the regular cross-section. The

Table 4.8: Nominal layups of the masts

	Nominal layup[5]
Sea Racer 35	[–° –° –° –°]
Farr 58	[–° –° –° –°]
J70	[–° –° –° –°]

Table 4.9: UD tape reinforced layups

Sea Racer 35[5]	
Port & starboard	[–° –° –° –° –° –°]
Fore & aft	[–° –° –° –° –°]
Width of UD tapes	– mm
J70[5]	
Port & starboard	[–° –° –° –° –° –°]
Width of UD tapes	– mm

load was incrementally applied mid-span, and the deflection was measured using a laser as a reference.

Each mast was tested in bending in three directions, with the mast laying on its port, starboard or aft side. The only exception is the Farr 58 mast which was not tested with the aft side resting on the supports. This was due to the geometry of the cross-section. After the bend tests were performed, the weight and centre of gravity of the masts were also obtained.

4.2.2 Fibre angle measurement

The fibre angles of the non-circular masts are measured using the same method as for the circular tubes - by tracing fibre tows with tape and transferring the line to a paper. The difference is that the non-circular sections have an irregular fibre angle distribution along its circumference due to the production method.

Since both the mandrel and the fibre tow cart are rotating and traversing with a constant speed, the fibre angle will vary in every point of the circumference, depending on the local radius from the rotational axis.

4.2.3 FE model

The masts are modelled in the same manner as for the spinnaker poles in Section 4.1.4. It is assumed that the modelling method applied on circular cross-sections can be adapted and applied also to non-circular cross-sections. The procedure follows the steps described in Appendix B.

4.2.4 Comparison of model and tests

The masts are modelled in LUSAS according to the test setup, using the same type of supports and loading. The obtained deflections are then compared to the test results in

[5]Sensitive information has been censored in the published version of this thesis.

order to see how close the analyses gets to the tests, where the result of the comparison is a percentage showing the difference.

4.3 Analysing fibre out of plane waviness

The second part of this thesis treats the laminate strength properties in compression. The idea is that the compressive strength can be predicted using a recently developed methodology for assessment of CFRP aeroengine components loaded in compression (Wilhelmsson et al., 2018).

The first part of this subject is to fibre waviness of an authentic Seldén laminate using a Matlab script developed at Chalmers which analyses digital pictures obtained from microscopy of the laminate.

The method is based on characterising the fibre waviness in a section plane parallel to the mode of failure, which in this case is out-of-plane. Thus, focus has been on characterising the out-of-plane fibre waviness.

4.3.1 The samples

Samples of the laminate was cut from a spinnaker pole. The pole in question is the same pole 39 mentioned in Section 4.1.1. A portion of the circumference of the spinnaker pole section was cut out. In Figure 4.8 the cuts are symbolised by the dashed lines marked A and B. It was made sure that the cut at A, was made perpendicular to the tangent of the circle. The two arrows in Figure 4.8 marks the surface that will be examined in the microscope. No measures were taken to make sure that the cut at line B was perpendicular to the tangent. Therefore, no analysis is performed on this surface.

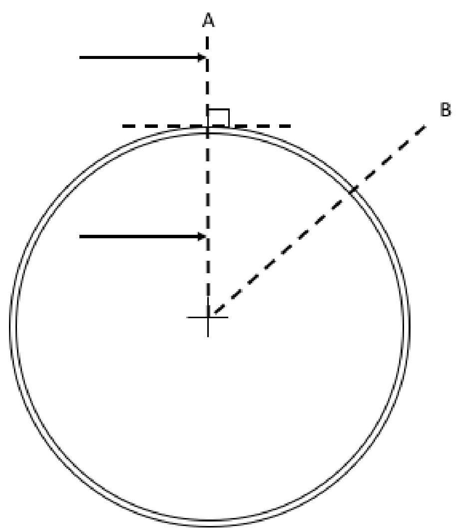

Figure 4.8: Schematics of test specimen cutting.

In total 6 specimens were manufactured. The samples were then cast in a clear epoxy resin. The surface that was to be examined under the microscope was gradually ground and polished using semi-automatic grinding and polishing equipment from Struers. This was done until a satisfying surface finish had been achieved.

4.3.2 Image processing of micrographs

Through a microscope, micrographs off the laminate were taken with 100 times magnification. Several images are taken so that the entire specimen is covered. The images are then joined to form a single panorama of each specimen. A cropped area of one of the micrographs is shown in Figure 4.9 where each individual fibre is easily observed.

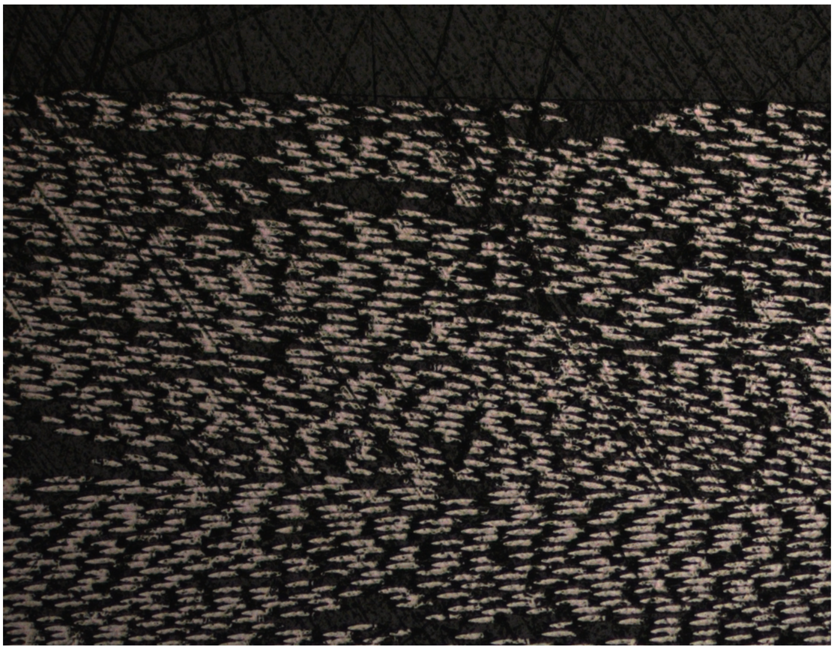

Figure 4.9: Part of a micrograph showing the cut fibres of the specimen.

An existing method has been used for measuring fibre misalignment in fibre waviness through image processing of micrographs (Wilhelmsson & Asp, 2018). The method is referred to as high resolution misalignment analysis (HRMA). This function is used to measure the fibre out of plane waviness.

The micrograph panorama is read into the HRMA script. The script divides the micrograph into regions called *cells*. The size of these cells determine the spatial resolution. In this analysis the cell size of 50×50 μm was applied. With the pixel resolution of 0.55 $\mu m/pixel$, the cell size becomes 91 *pixels*. The thickness of each ply in the sample is approximately 300 μm, or 545 *pixels*, with the given pixel resolution. Thus, the resulting spatial resolution is approximately 6 cells through the thickness of each ply. The global fibre mean misalignment angle, across the entire micrograph panorama is then calculated according to (Wilhelmsson & Asp, 2018)

$$\bar{\theta} = \frac{1}{n}\sum_{i=1}^{n} |\bar{\theta_i}| \tag{4.7}$$

Where $|\bar{\theta_i}|$ is the absolute value of the fibre mean misalignment in the i:th cell, and n is the total number of cells measured.

4.4 Compression strength analysis

Once the laminate stiffness knockdown factor mentioned in the previous section has been obtained, several compression tests are performed to find the compressive stiffness and strength of the same part.

4.4.1 Test specimens design

Previous compression tests of composite tubes have shown that the failure tends to initiate on the edge of the tube, closest to the load cell. Crushing of the ends will not give a representative result.

An alternative method of testing is proposed, where the point of failure initiation is controlled by a local decrease in cross-sectional area of the tube. This decrease in area is achieved by milling two slots parallel to the rotational axis of the tube, as shown in Figure 4.10.

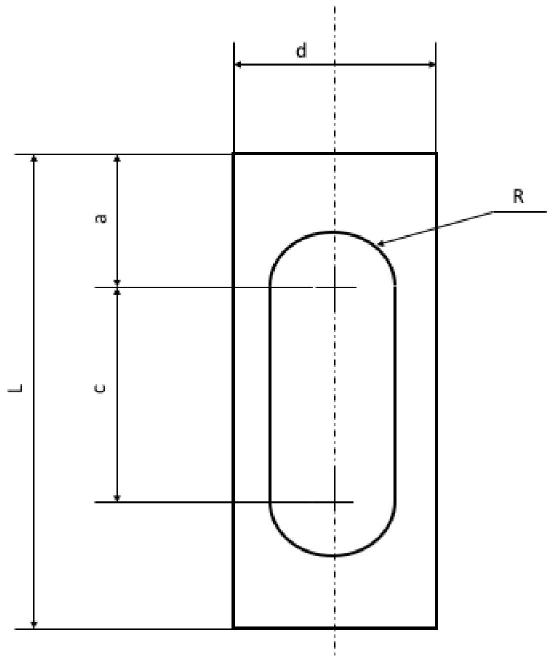

Figure 4.10: Dimensions and position of the slots.

The theory behind the design of the specimen is that the slots will force the failure to initiate at the thinnest point of the test sections. An important design criteria for the test specimen has been to minimise any bending of the test sections in order to obtain a unidirectional stress state. The magnitude of the bending is calculated in Equation (4.8) according to (ASTM D3410/D3410M-16, 2016). The same standard states that the bending of the test specimen has to be less than 10% at failure strain for the strength and strain–to–failure data to be considered valid.

$$\text{Bending} = \frac{\epsilon_1 - \epsilon_2}{\epsilon_1 + \epsilon_2} \times 100 \tag{4.8}$$

In Equation (4.8), ϵ_1 and ϵ_2 is the strain at the inner and outer surface of the laminate.

The design has been tested and analysed in LUSAS in order to check the bending at half of the tube length and the inevitable stress concentrations that will arise due to the slots. The variables L, c, a and R were adjusted systematically and the influence of these changes were analysed in the FE-simulations.

The designs that fulfilled the criterions were manufactured and a preliminary compression test was performed. The intentions of this test was to see whether the failure would occur at the test section or not. If the failure were to occur at any other location, such as at the edges of the tubes, the design would have to be discarded.

Two different specimen designs passed the preliminary compression test. The preliminary test showed that these two specimen designs failed at or near the middle of the test sections. The specimen dimensions are shown in Table 4.10, together with the bending, according to Equation 4.8, estimated by the LUSAS FE-model.

Table 4.10: Test specimen dimension variables

	Dimensions [mm]					Bending [%]
	L	R	c	a	d	
Specimen design 1	90.0	30.0	20.0	37.5	39.0	38.2
Specimen design 2	90.0	20.0	20.0	37.5	39.0	6.6

The reasoning behind choosing two different specimen designs is that specimen design 1, with the larger hole radius will have less influence from the stress concentrations caused by the slots, explaining why it was decided to keep the design even though large values of bending had been predicted by the FE-model. While specimen design 2 has a smaller hole radius and wider test sections. This should cause more stress concentrations from the slot. At the same time the wider test sections should allow for less bending during the test. The method used to evaluate the bending is covered in Section 4.4.2.

In addition to the two specimen types with slots, tubes without slots were also tested in order to find the compression stiffness of the laminate.

4.4.2 Compression test procedure

The final compression tests were performed at Chalmers University of Technology using an Instron 400RD compression testing machine. The machine was configured to apply a load at a constant crosshead displacement rate of 1.3 mm/min, according to the ASTM D695 standard (ASTM D695-15, 2015). The load was then measured by the machine's software at a sample frequency of 10 Hz. During the tests, strain gauges are mounted on the inside and outside of the test sections to measure the bending during the tests, Figure 4.11. The data from these strain gauges was logged with a sample frequency of 50 Hz.

The specimen with slots were loaded until a significant load drop occurred, accompanied by a loud cracking noise, the load F_{max} is documented at failure. From the strain gauge data the compressive strength and bending (Equation (4.8)) of the specimens were calculated. The strain at the tabs was calculated for port and starboard side of the specimen, as the mean of the strain at the inner and outer surfaces. Port and starboard is denoted by the index P and S respectively.

$$\epsilon_i = \frac{\epsilon_{1_i} + \epsilon_{2_i}}{2} \qquad i = P, S \tag{4.9}$$

With the strain at the tabs the load at each tab was calculated

$$F_i = \frac{\epsilon_i}{\epsilon_P + \epsilon_S} \qquad i = P, S \tag{4.10}$$

Finally the compressive strength is determined by dividing the maximum force acting on either of the tabs, with the cross section area of a single tab, A_{tab}.

$$X_C = \frac{\max\left(F_S, F_P\right)}{A_{tab}} \tag{4.11}$$

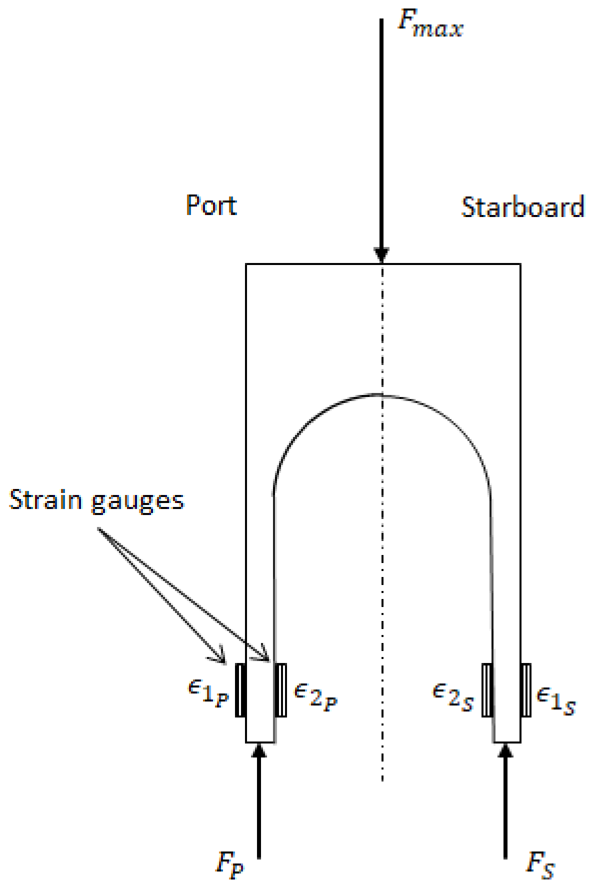

Figure 4.11: Schematics of strain gauges and loads acting on test specimen.

No strain gauges were fitted on the tubes without slots. The load and displacement of the load cell was logged during the tests of the solid tubes.

5 Results

5.1 Circular cross-sectional models

Regarding the results from the simulations and benchmark tests of the circular cross-sections, it has been reasoned that the FE-simulations, the benchmark tests and the comparison between the two serves as a proof of concept. In the following sections it will be shown that a good correlation between simulations and benchmark tests has been shown to exist. The statement is true for both spinnaker poles, and the hybrid laminate tube. This indicates that material properties of the laminates have been approximated sufficiently accurate and that the FE-models are accurate enough to produce results that predict the stiffness of the cross-sections in a consistent and satisfying way.

5.1.1 Spinnaker poles benchmark test results

In Table 5.1 and 5.2 the test results for pole 39 and pole 88 is presented, respectively. During the testing of pole 39, a loud and clear cracking sound was heard when the load reached approximately 1700 N. The load was immediately decreased once the noise was heard. No damage indicating failure could be seen on the pole. After the test the pole was checked for internal damage by tapping a coin on the surface to hear differences in the sound due to delamination. No damaged zone could be found with this method. Further investigations will be required to find the cause of the cracking sounds. As for pole 88, no cracking sounds or other indications of failure were noted during the test.

It can be seen in Tables 5.1 and 5.2 that the deflection is more or less identical for AL/AR and BL/BR in every load increment. It can be concluded from the tables that symmetric deflection around the mid-point has been achieved with satisfactory accuracy. Therefore, the mean deflection of both sides is calculated for each load increment according to Equations (5.1) and (5.2).

Table 5.1: Pole 39 test results

	Deflection [mm]				
Load [N]	AL	BL	C	BR	AR
265	15	20	22	20	15
452	24	33	37	33	25
658	37	49	54	49	37
913	49	66	72	65	48
1120	63	82	90	82	63
1375	75	100	112	101	76
1591	88	118	130	118	89
1159*	65	87	95	87	65

* measured after cracking sound

Table 5.2: Pole 88 test results

	Deflection [mm]				
Load [N]	AL	BL	C	BR	AR
1061	24	31	35	31	24
1611	37	48	52	47	36
2121	47	62	69	62	46
2612	57	76	84	77	57
3084	69	91	100	90	67
3683	82	108	119	109	82
4193	93	124	137	124	93
4812	108	144	157	143	107
6030	136	181	198	180	136

$$A_i = \frac{AL_i + AR_i}{2} \tag{5.1}$$

$$B_i = \frac{BL_i + BR_i}{2} \tag{5.2}$$

The results of Equation (5.1) and (5.2) are presented in Tables 5.3 and 5.4. Since the mean values are nearly identical with the original measured values of AL, AR and BL, BR all further analysis and comparison of test results will be according to these values.

Table 5.3: Pole 39 mean values of test results

	Deflection [mm]		
Load [N]	A	B	C
265	15	20	22
452	25	33	37
658	37	49	54
913	49	66	72
1120	63	82	90
1375	76	101	112
1591	88	118	130
1159*	65	87	95

* measured after cracking noise

In Figures 5.1 and 5.2 the values of Tables 5.3 and 5.4 are plotted against the load for both poles.

In Figure 5.1 the load and deflection follow a linear relation. In Figure 5.2 this linear relation is more obvious. Since both poles are of the same material, shape and loaded in the same configuration it can be concluded that a linear relation between load and deflection exists in both cases. Larger deviations from this linear relation in Figure 5.1, is most likely explained by measuring errors. Since it was concluded in Table 5.1 and 5.2 that near exact symmetric deflection around the mid-point has been achieved, the mean of AL and AR will simply be referred to as the deflection in point A. Likewise the mean of BL and BR will be referred to as deflection in point B.

Table 5.4: Pole 88 mean values of test results

	Deflection [mm]		
Load [N]	A	B	C
1061	23	31	35
1611	36	48	52
2121	47	62	69
2612	57	77	84
3084	68	91	100
3683	82	109	119
4193	93	124	137
4812	108	144	157
6030	136	181	198

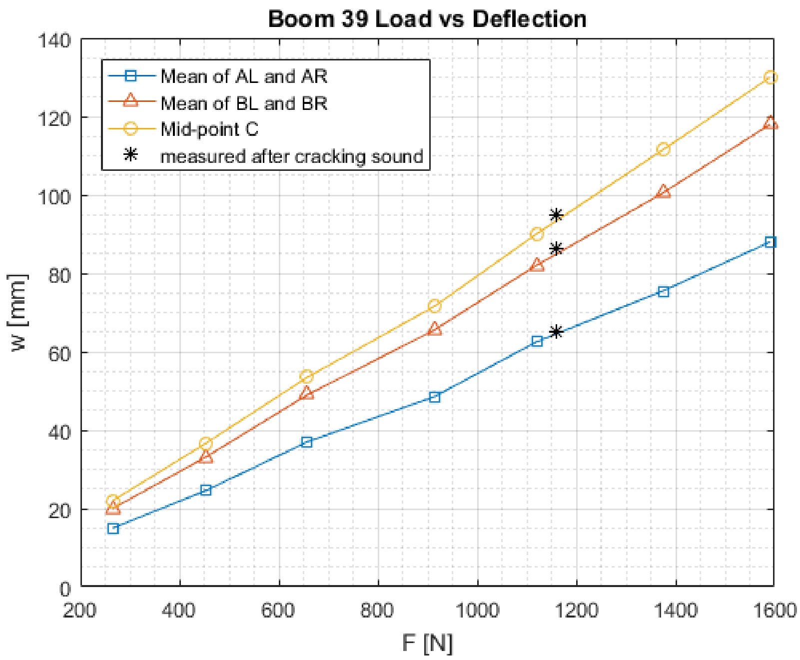

Figure 5.1: Pole 39 load vs deflection test results.

5.1.2 Comparison of spinnaker poles test results and FE-simulations

In Figures 5.3 and 5.4 the extrapolated test data can be seen plotted together with the results from the FE-model explained in Section 4.1.4. Further, in the previous section, it was concluded that the load and deflection follows a linear relation the load-curves can be extrapolated so that they originate from the origin. In Figures 5.5 and 5.6 the normalised difference between LUSAS and test results in points A, B and C are plotted according to Equation (5.3).

$$\delta = \frac{w_{i,FE} - w_{i,test}}{w_{i,FE}} \tag{5.3}$$

The variable w_{FE} is the deflection calculated by the LUSAS model and w_{test} is the deflection measured in the tests. Thus positive values indicate that the deflection predicted by the LUSAS model is larger than test results, and vice versa for negative values.

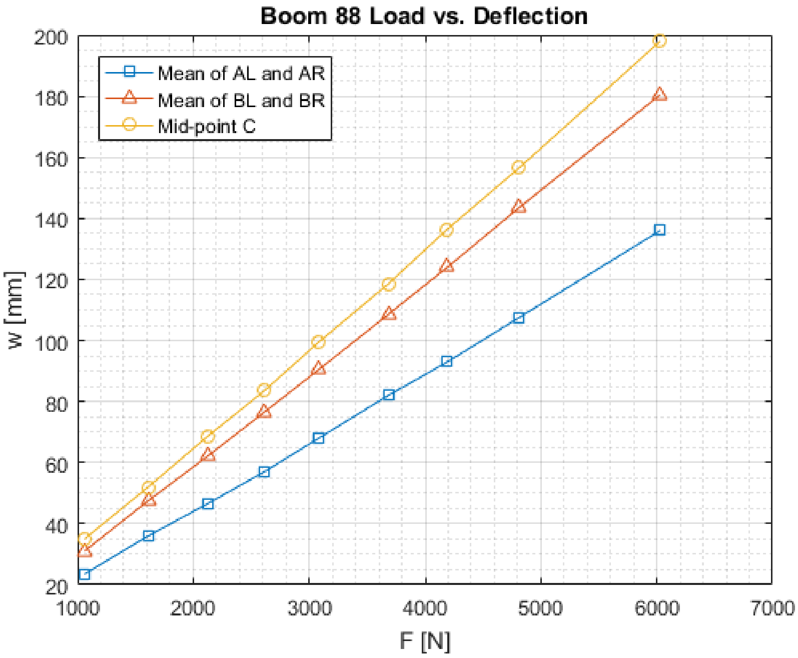

Figure 5.2: Pole 88 load vs deflection test results.

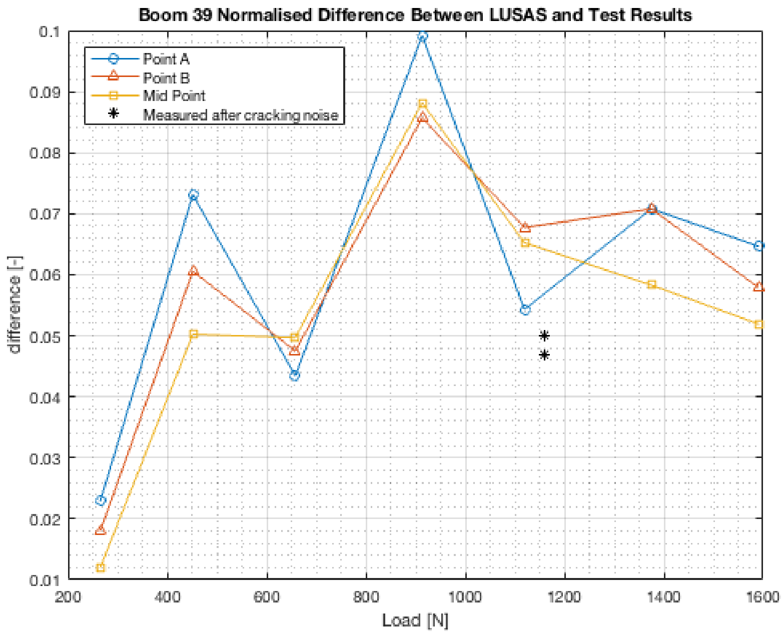

Figure 5.5: Pole 39 normalised difference between LUSAS and test results.

In Figure 5.5 the difference between the LUSAS model and the measured test results for pole 39 varies between 1.2% to 10.0%. The 10.0% peak in difference at 913 N of load is probably due to a measurement error. The other exception is the relatively small difference of 1.2% to 2.2% recorded at the lowest load of 265 N. However, for remaining load increments the difference varies between 4.5% to 7.2% which has to be considered to be within acceptable margins.

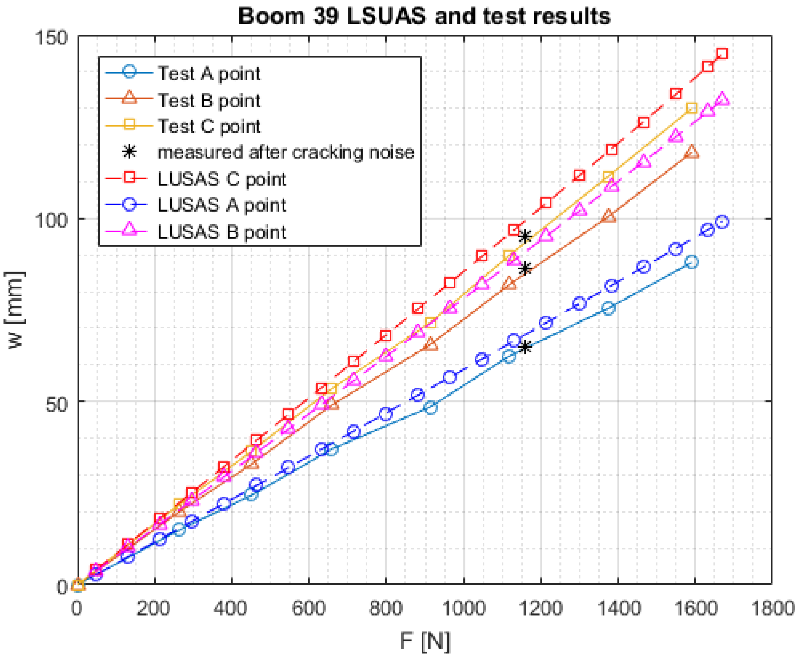

Figure 5.3: Pole 39 test results and LUSAS results.

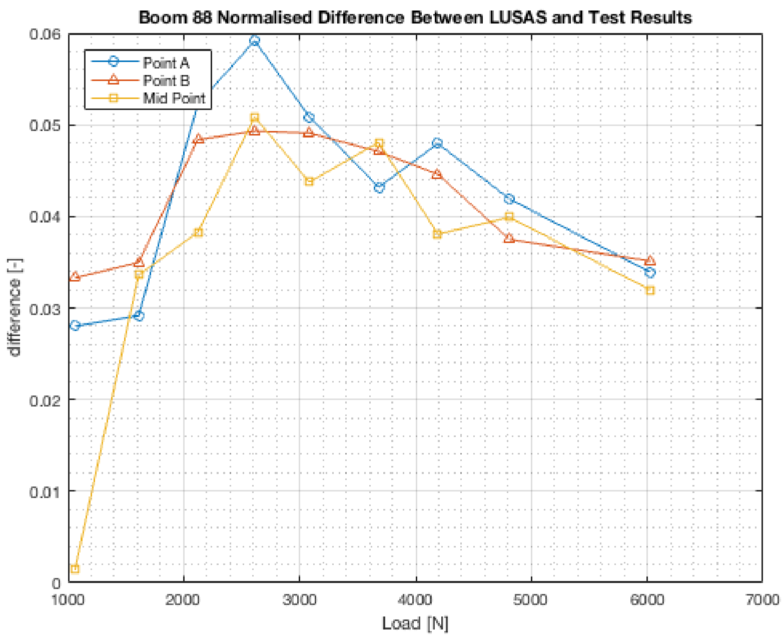

Figure 5.6: Pole 88 normalised difference between LUSAS and test results.

For pole 88 the differences vary less compared to pole 39. The same trend can be seen with small differences for the smallest load applied in the test. However no clear peak in differences is recorded here. If the minimum of 0.2% for the midpoint at 1061 N and the maximum 6.0% for point A at 2612 N is excluded, the difference between LUSAS model and test results varies between 2.8% and 5.1%. Again the LUSAS model is considered to match the test results with acceptable accuracy.

In Table 5.5 the results of the linear regression on the mid-point deflection is shown. In

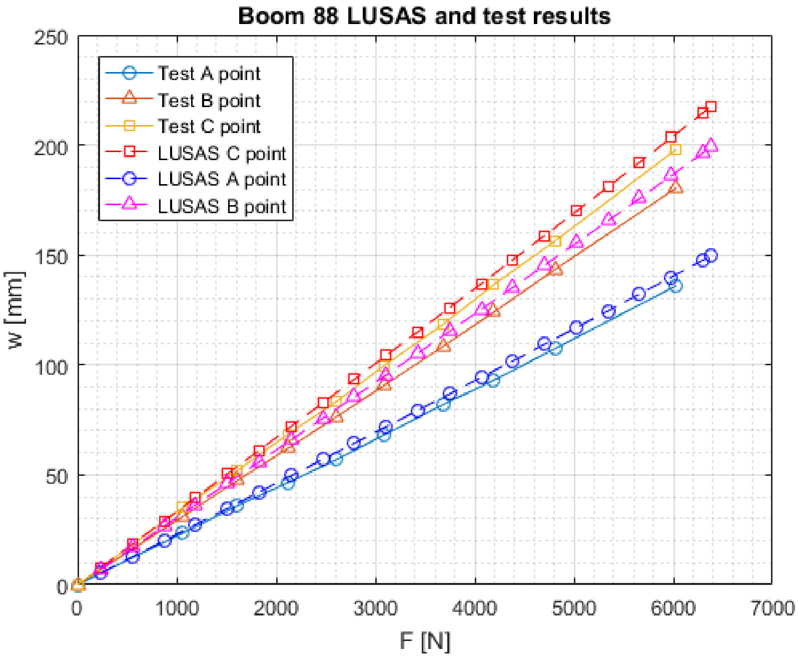

Figure 5.4: Pole 88 test results and LUSAS results.

the table it can be seen that the load and deflection follows a linear relation, since ρ is close to 1 for both poles.

Table 5.5: Results of linear regression of test results.

Test results	$\mu_{w_{mid}}$ [mm]	$\sigma_{w_{mid}}$ [mm]	μ_F [N]	σ_F [N]	ρ [-]	k [mm/N]
pole 39	76.26	37.30	95.88	46.62	0.9995	0.7997
pole 88	105.34	52.45	330.44	162.74	0.9999	0.3223

In Table 5.6 the linear regression of the LUSAS results is shown. The results show that the LUSAS results follow a linear relation.

Table 5.6: Results of linear regression of LUSAS results.

LUSAS results	$\mu_{w_{mid}}$ [mm]	$\sigma_{w_{mid}}$ [mm]	μ_F [N]	σ_F [N]	ρ [-]	k [mm/N]
pole 39	75.46	44.56	89.52	52.37	1.0000	0.8508
pole 88	115.38	66.92	347.82	199.79	1.0000	0.3350

Figures 5.7 and 5.8 shows the mid-point deflection linear regressions of LUSAS and test results, plotted together with Equation (4.6) for pole 39 and pole 88.

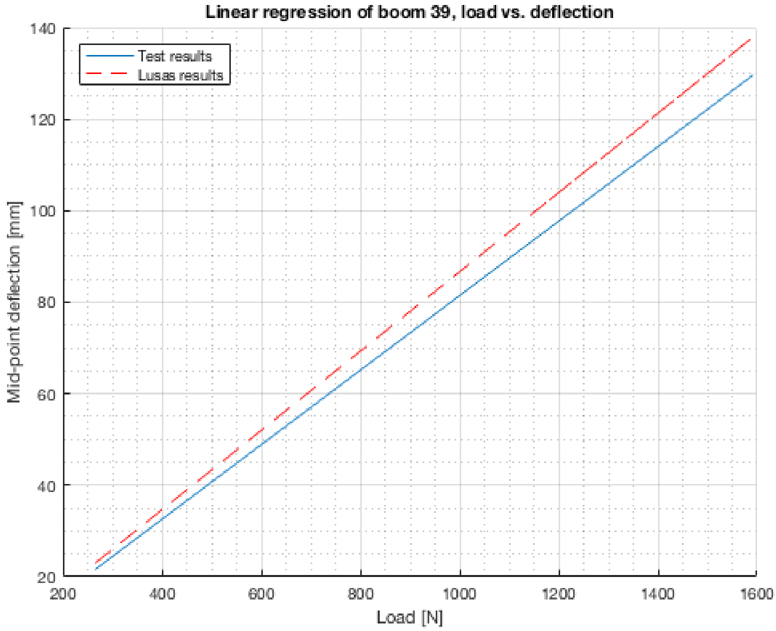

Figure 5.7: Pole 39 linear regression of LUSAS and test results.

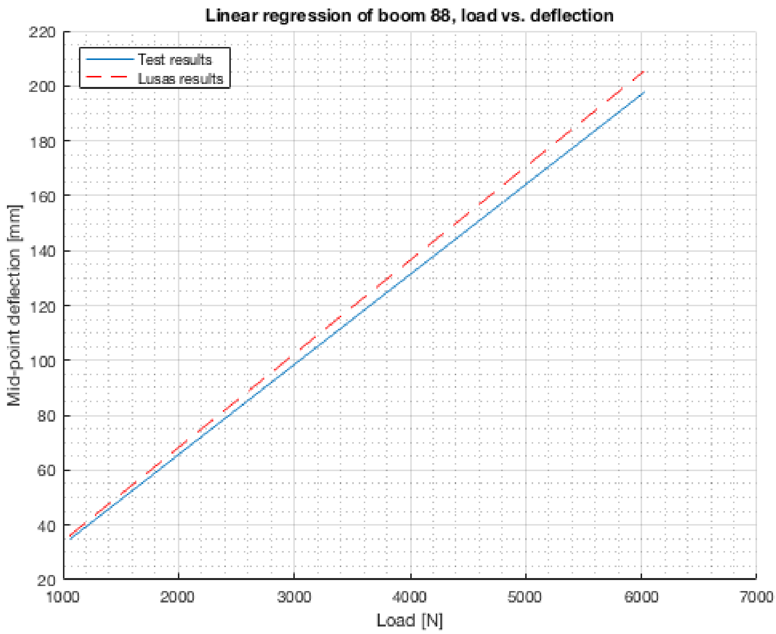

Figure 5.8: Pole 88 linear regression of LUSAS and test results.

With the values in Tables 5.5 & 5.6 and Equations (4.5) & (4.6), the difference between test results and LUSAS results can also be represented using Equation (5.4).

$$\Delta = \left(\frac{k_{LUSAS}}{k_{test}}\right) - 1 \tag{5.4}$$

Equation (5.4) gives the results presented in Table 5.7.

Table 5.7: Difference between LUSAS and test results

	Δ [%]
Pole 39	6.39
Pole 88	3.94

5.1.3 Comparison of hybrid laminate tube test results and FE-simulations

In Section 4.1.2 test results from three point bend tests performed on a hybrid laminate tube were presented. In this section a comparison between these test results and the results of the FE-simulations is made. In Table 5.8 the results from the tests and FE-simulations are presented and compared. In Table 5.8 the average deflections of all 53 bend tests are presented.

Table 5.8: Results of Seldén hybrid laminate tube tests and simulations.

	$L_{span}/4$	$L_{span}/2$	$3L_{span}/4$
$\overline{w}_{test}$ [mm]	26.3	38.5	26.3
w_{FE} [mm]	27.9	41.0	27.9
Difference [%]	6.08	6.49	6.08

It can be seen that the difference between simulation and test results are small and on the same side as the previous results obtained for the circular poles. Since the hybrid laminate tube FE-model was modelled using the same methodology as applied to the spinnaker poles, one can argue that the results is another argument that the FE-models are accurate for determining stiffness. Furthermore, in Section 2.2.4 material properties for the hybrid laminate were calculated. These properties have now been shown to produce deflections in the FE-simulations that are close to the measured deflections in the test. This indicates that the method to calculate the properties of the hybrid laminate in Section 2.2.4 is a valid method in this case. However to implement the method on an arbitrary hybrid laminate, i.e. a laminate with three constituents instead of the usual two, more tests should be performed.

5.1.4 Fibre angle analysis

After measuring the fibre angles of the tubes according to the method described in Section 4.2.2 it was concluded that the nominal wind angle and the actual wind angle was the same with very small variations. The actual wind angle was within one degree of the nominal wind angle in all observations.

5.1.5 Summary of circular cross-section results

The results of the circular cross-section models and tests have shown that the FE-simulations of the benchmark test have produced results that are close to the measured values. It is concluded that the methodology applied to create the FE-model is sufficiently accurate to be applied, with confidence, also to the non-circular cross sections.

However, minor modifications will have to be made to take some of the features of the non-circular cross-section into consideration. It has also been shown that the material properties used in the FE-models produce results that gives good correlation with the tests. It can be concluded that these material properties are sufficiently accurate to determine the bending stiffness of the laminates. This statement can be considered to be true for the T700SC/UF3325 TCR material properties that were supplied by Seldén as well as the hybrid laminate material properties that were calculated in Section 2.2.4.

5.2 Non-circular cross-section model

The tests performed at SML show an interesting behaviour where two of the three masts deflect asymmetrically on port and starboard side. Possible explanations for this will be discussed further in Section 6.2. Tables 5.9 to 5.11 show the results for all three masts tested at SML.

Table 5.9: Loads and deflections for the Sea Racer 35 mast, showing the asymmetric deflection.

Deflection of Sea Racer 35 mast [mm]			
Load [N]	Port down	Starboard down	Aft down
0	54	65	26
98.2	78	95	38
196.4	110	124	51
294.6	139	152	63

Table 5.10: Loads and deflections for the Farr 58 Maiden mast, showing the asymmetric deflection.

Deflection of Farr 58 mast [mm]			
Load [N]	Port down	Starboard down	Aft down
0	8	13	-
117.9	9	15	-
216	12	18	-
314.2	13	20	-
412.4	16	23	-
510.6	18	25	-
608.8	20	27	-
741.4	23	30	-

The three masts have also been analysed in LUSAS where the bending was tested with the mast laying on its aft for the Sea Racer and the J70, and on its sides for all three masts. The FE-model was only tested on one side since the results proved to be entirely symmetric for both port and starboard. This symmetry was confirmed by varying the thickness and fibre angles in LUSAS according to the observed variations that the masts showed in reality. The results from the FE-models are shown in Figures 5.9 to 5.11.

The diagrams show a a fairly good match between the test results and the FE-results, with some deviations due to initial deflection. The conclusion is that comparing the deflections

Table 5.11: Loads and deflections of the J70 mast.

	Deflection of J70 mast [mm]		
Load [N]	Port down	Starboard down	Aft down
0	0	0	0
117.8	13	14	10
216	24	25	18
314.2	36	38	25
412.4	48	50	33
608.8	-	-	50

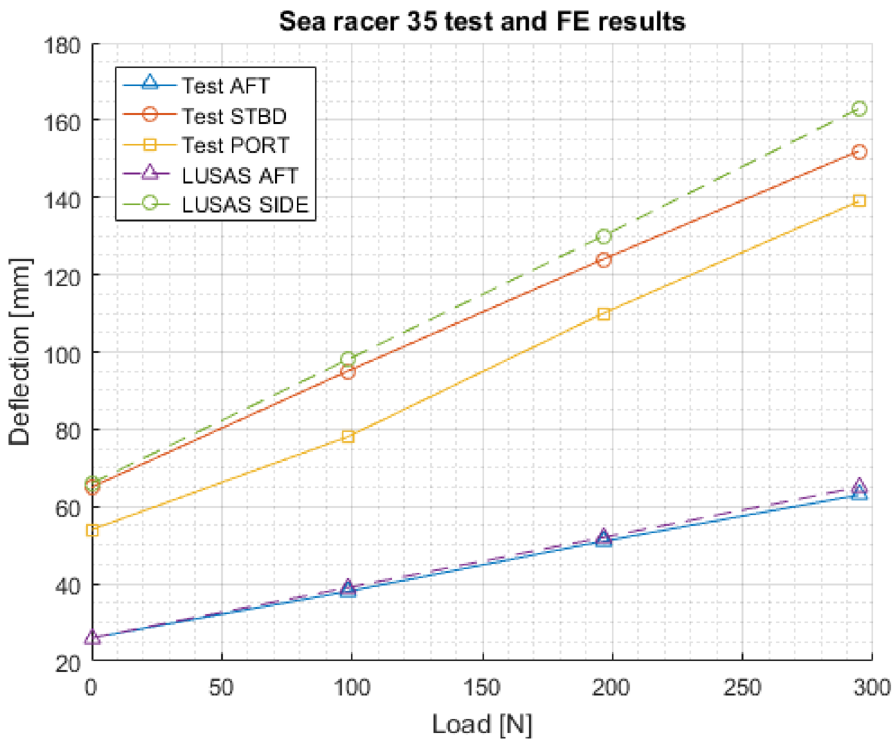

Figure 5.9: Sea racer 35 bend test results

in absolute numbers is not representative for the stiffness of the masts. Instead, a linear regression analysis identical to the one in Section 5.1.2 is performed on the test and FE-results. Assuming that the deflection curves, and thus also the stiffness, are still linear or close to linear for the non-circular sections, the regression will give k-values that will be directly comparable as a measure of the stiffness. Table 5.12 shows the results of this comparison, calculated using Equation (4.5).

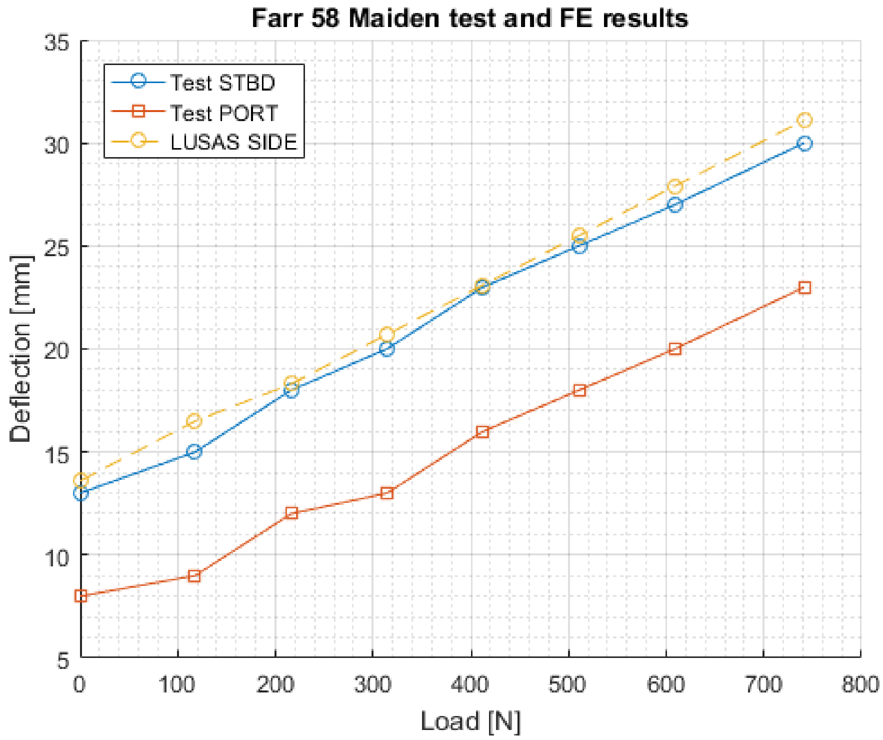

Figure 5.10: Farr 58 Maiden bend test results

Table 5.12: Stiffness comparison, FE vs. tests

Load case	Difference in stiffness [%]
Searacer 35 - Aft	4.8
Searacer 35 - Starboard	11.4
Searacer 35 - Port	12.5
Farr 58 - Starboard	0.3
Farr 58 - Port	12.4
J70 - Aft	0.0
J70 - Starboard	10.5
J70 - Port	15.1

The values in Table 5.12 indicate that the FE-results are consistently less stiff than the test results, which was also the conclusion from the circular cross-sections. Unfortunately, the difference for the non-circular cross-sections are larger and vary from 0 to 15%.

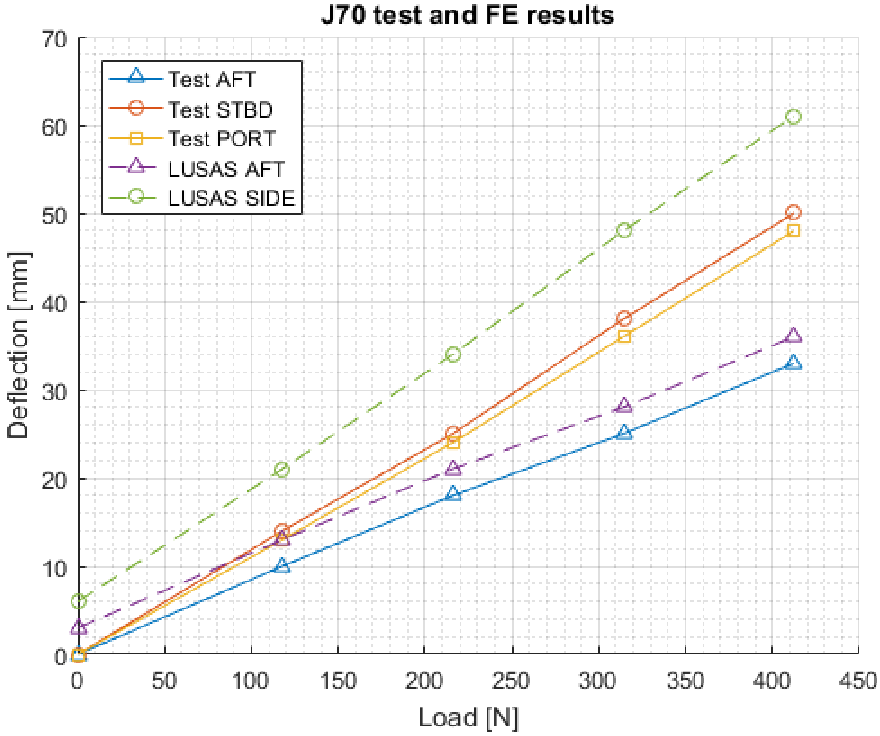

Figure 5.11: J70 bend test results

5.2.1 Fibre angle analysis

The results of the fibre angle analysis of the non-circular tubes proved to be harder to interpret than for the circular tubes. Several tracings were made on different tubes, and the conclusion was that the fibre angle does change slightly around the aft corners of the mast section. It was concluded that the fibre angle in this area may change between $\pm 4°$.

This variation in fibre angle was taken into consideration and tested in LUSAS, but the results showed negligible effect on the overall stiffness of the masts. It was decided to simply use the nominal wind angle in all simulations.

5.3 Out of plane waviness of fibres

Portions of the micrograph specimens of the laminate are shown in Figure 5.12. These are the micrographs that are analysed with the HRMA method (Wilhelmsson & Asp, 2018). When observing the micrographs the five layers, one $-°$[6] and two $-°$, can be distinguished. The $-°$ ply can be seen in the bottom of each micrograph. The fibres in the $-°$ layers appear light and oval shaped in the micrographs while the resin surrounding the fibres appear in a darker shade. These micrographs are then assembled into one, where approximately 40 individual micrographs were required to capture the entire specimen.

In Figure 5.13 the distribution of the fibre misalignment in each specimen is plotted. In these plots the magnitude of the fibre misalignment is shown. The difference in fibre misalignment direction between $-°$ and $-°$ layers is clearly visible, especially in specimen

[6]Sensitive information has been censored in the published version of this thesis

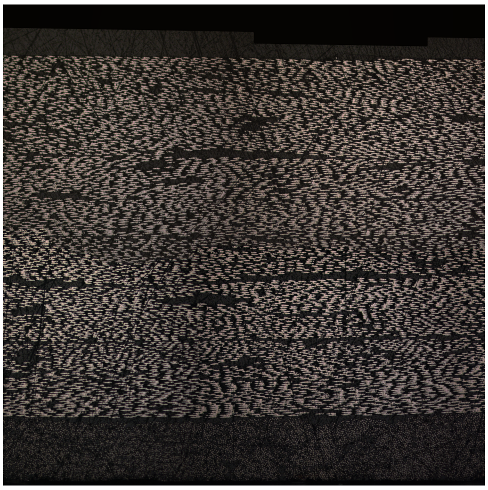

(a) Specimen A1

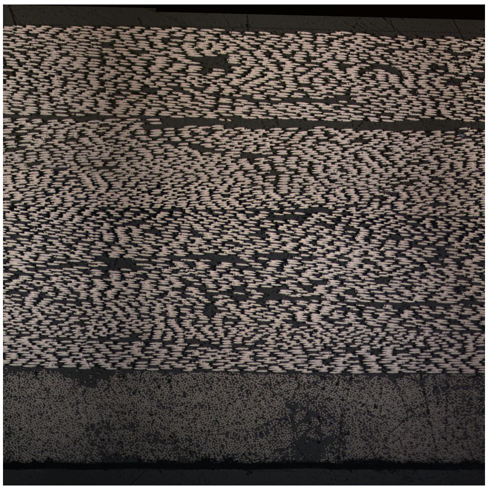

(b) Specimen A2

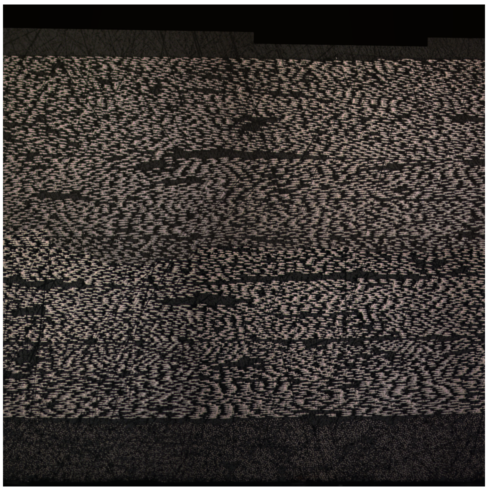

(c) Specimen B1

(d) Specimen B2

Figure 5.12: The micrographs sample

A1. The nature of the filament winding process creates this pattern where the direction of the fibre misalignment is related to the fibre direction in each layer. At the bottom of each plot it can be seen that only a few measurements are taken in the $-^{\circ}$[7] layer. This is expected since the HRMA is capable of identifying fibres that are oriented in the sectioned plane.

From the distributions in Figure 5.13[7] the mean fibre misalignment angle $\overline{\theta}$ and standard deviation of fibre misalignment angles σ_θ can be calculated. The maximum fibre misalignment angle θ_{99} is calculated as the 99-percentile of the distribution of angles as proposed by Wilhelmsson et al. (2018). The results are presented in Table 5.13[7] below.

[7]Sensitive information has been censored in the published version of this thesis

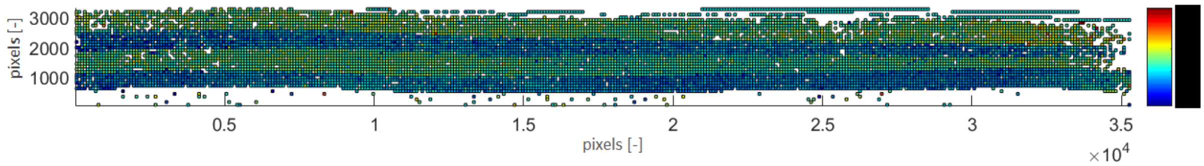

(a) A1

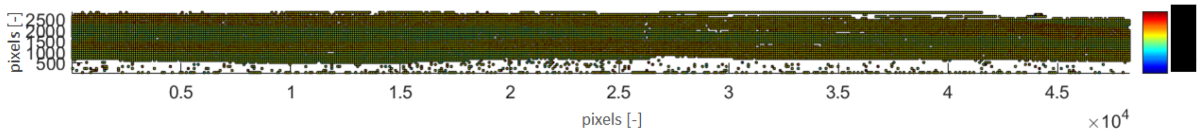

(b) A2

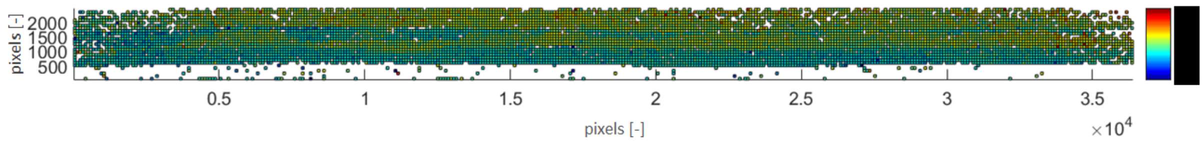

(c) B1

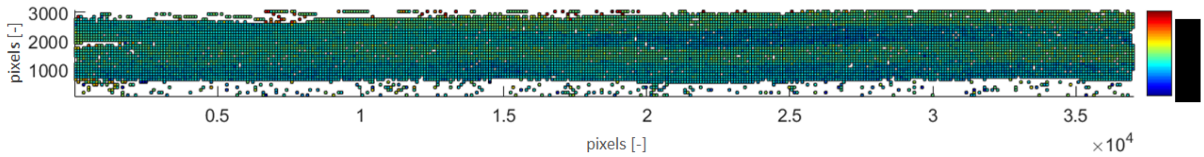

(d) B2

Figure 5.13: Distribution of fibre misalignment in the laminates.

Table 5.13: Results of fibre misalignment image analysis

	Specimen[8]			
	A1	A2	B1	B2
$\overline{\theta}$ [°]	-	-	-	-
σ_θ [°]	-	-	-	-
θ_{99} [°]	-	-	-	-

The mean misalignment $\overline{\theta}$ and maximum fibre misalignment θ_{99} vary between $-^\circ - -^\circ$[8] and $-^\circ - -^\circ$[8] respectively. This variation is to be expected due to the local variations of the fibre waviness in the masts, and also due to the fact that the mast has been sampled at different locations. The angles presented in Table 5.13 can be related to the classification of waviness magnitude levels in the study by Wilhelmsson and Asp (2018), where a distinction is made between moderate and high levels. The angles in Table 5.13 would then be considered as very high.

[8]Sensitive information has been censored in the published version of this thesis.

5.4 Compression test results

The results from the compression tests can be divided into three groups, one for each type of specimen geometry. The data consists of a load/displacement diagram as well as a strain/time diagram. The solid tubes were tested without strain gauges and will therefore not have any measured data on strain. The stress at failure for each specimen is presented in Table 5.14.

The three test specimens with a 30 mm slot diameter behave similarly in two of the three tests with a failure load between — kN[9]. One of the test specimens appears to have another stiffness with a slightly higher failure load of almost - kN as shown in Figure 5.14[9]. This is possibly due to the fabrication method not being exact. The outlying results may therefore be misleading.

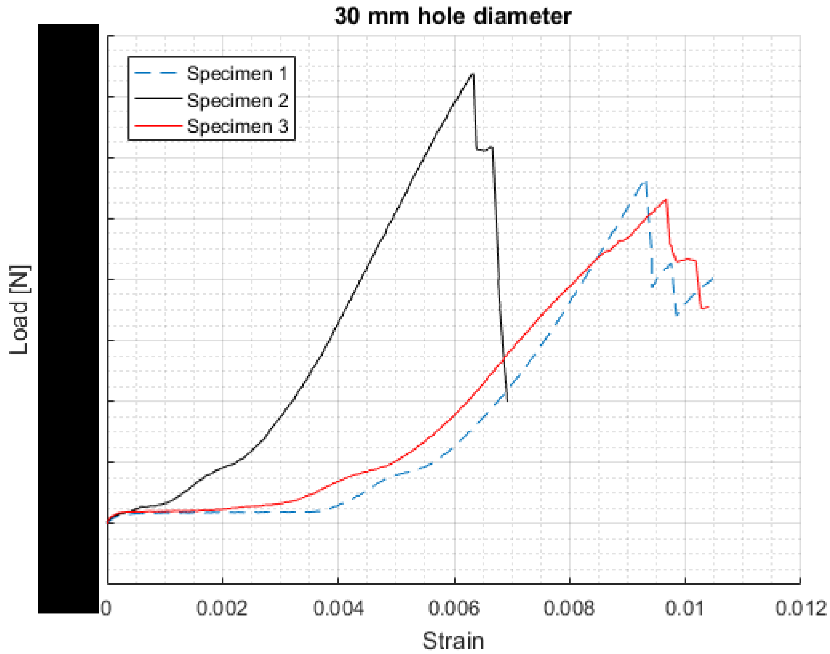

Figure 5.14: Load curves for 30 mm specimen

After measuring the width of the specimen test sections, the total cross-sectional area in the point of failure was calculated. The strain in each side of the specimen was found and the failure load was divided proportionally based on the strain. The strain data is found in Appendix A. The maximum of the two stresses obtained from each specimen is then considered to be the failure stress.

Figure 5.15[9] shows that the 20 mm slot diameter specimen behave similarly regarding the failure load, where the load is almost twice as high as for the 30 mm specimen. The same method of finding the failure stress that was used for the 30 mm specimen is used here.

The solid tubes without slots were primarily tested to find the compressive stiffness of the tube. This was done by first calculating the strain as the displacement (i.e. the distance the load cell has moved) divided by the specimen length. The slope of a line close to

[9]Sensitive information has been censored in the published version of this thesis.

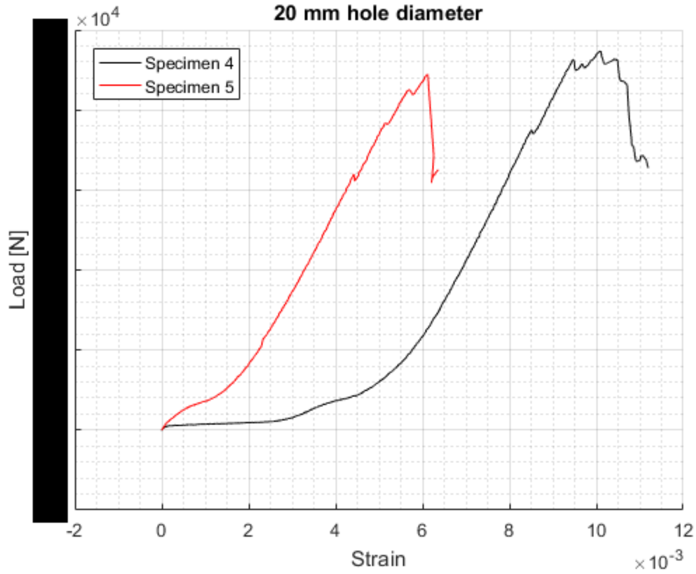

Figure 5.15: Load curves for 20 mm specimen

the maximum load, where the slope is linear or close to linear, was then calculated using Equation (5.5). The value obtained is the Young's modulus for the specific specimen. It is clear from Figure 5.16[10] that this should give a quite accurate result since the curves straighten out almost completely well before failure occurs.

$$E_{spec} = \frac{\Delta\sigma}{\Delta\epsilon} \tag{5.5}$$

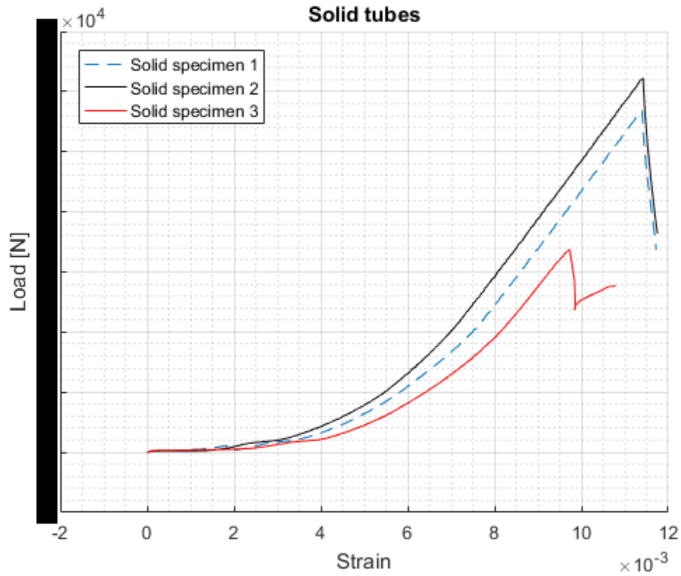

Figure 5.16: Load curves for solid tube specimen

[10] Sensitive information has been censored in the published version of this thesis.

5.4.1 Summary of compression test results

The compressive stress and bending at failure of the slotted tubes are presented in Table 5.14[11]

Table 5.14: Compressive stress and bending at failure

	X_c [MPa]	Bending [%]
Specimen 2 - 30 mm	-	79.8
Specimen 3 - 30 mm	-	44.2
Specimen 4 - 20 mm	-	1.0
Specimen 5 - 20 mm	-	8.7

The specimen with 30 mm hole diameter shows excessive bending at failure. The large bending of these specimens make the results questionable. Specimen 2 is closer to being subjected to pure bending than to pure compression. However, Specimen 4 and 5 fulfils the criteria of less than 10% stated in (ASTM D3410/D3410M-16, 2016).

Figure 5.17[11] shows the compressive strength plotted against the maximum fibre misalignment angle. The Argon criteria has been plotted with an assumed lower and upper bound of the composite shear yield limit. Except for specimen 3, the results seem to agree with the lower bound of 50 MPa. Table 5.14 shows that specimen 4 and 5 are the only specimens with allowable amounts of bending, 1.0% and 8.7% respectively. If only these two specimens are considered valid, the experimental compressive strength of the laminate is - MPa, calculated as the mean compressive strength of the two specimens.

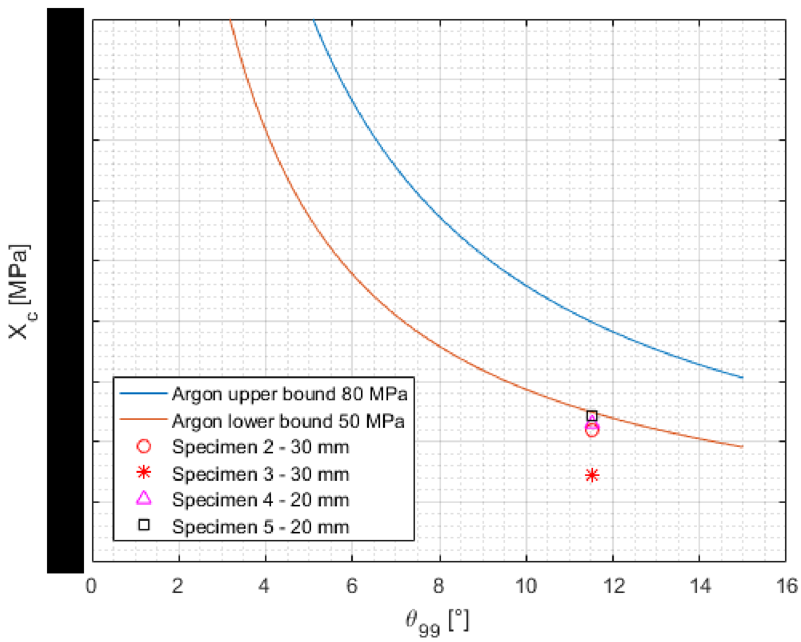

Figure 5.17: Compressive strength plotted again the maximum angle together with the Argon criteria.

[11] Sensitive information has been censored in the published version of this thesis.

The stiffness found in the compression tests, shown in Table 5.15[12], is quite close to the given Young's modulus of[12] - GPa used in the FE-simulations for all three specimen.

Table 5.15: Experimental Young's modulus in compression

	E_{exp} [GPa]
Specimen 1	-
Specimen 2	-
Specimen 3	-
Mean value	-

[12]Sensitive information has been censored in the published version of this thesis.

6 Discussion

This chapter will treat some of the questions and thoughts that have appeared during the project.

6.1 Circular cross-section model

Both the carbon fibre laminate poles as well as the hybrid laminate poles show consistent bending behaviour in the tests, and the FE simulations manage to match the stiffness of the poles within 6.5%. In all cases, the calculated stiffness is lower than the tested stiffness. One could argue that lowering the stiffness in the FEA would make it possible to match the tested stiffness even better. This would however mean that one of the initial limitations of only using provided material data from Seldén would be disregarded. We choose not to do this, but instead see the deviation in stiffness as an added safety factor since if the maximum deflection is used as a design criteria, the FE simulations will always show a larger deflection.

6.2 Non-circular cross-section model

The results covered in Section 5.2 show that the developed modelling method works consistently for the non-circular mast when looking in the longitudinal direction. However, the FE results and the test results can differ substantially when looking at port and starboard side separately. It was also clear that the difference could be reduced by comparing the slopes of regression lines obtained from the raw test data. Using this way of comparing stiffness reduced the difference between FE and reality to between 0 to 15%. However, the numbers still show a difference between port and starboard, a fact that is made even clearer by comparing the stiffness of the test data between the sides, as shown in Table 6.1.

Table 6.1: Difference in stiffness between port and starboard of the test data.

	Difference [%]
Searacer 35	1.0
Farr 58	12.1
J70	4.2

There is no clear answer to what is causing this asymmetric stiffness, but there are some possible causes that have been observed during the thesis work. The simplest explanation is that there may be inaccuracies in the test method. The masts that have been tested may have been placed differently between measurements, and the measurements may have some errors as well. A solution to this problem would be to conduct more tests on masts to get an even larger sample population.

Other explanations that are not as simple have to do with the geometry of the mast itself.

Some variations in the cross-sectional geometry as well as the global mast geometry has been observed. One such variation is the laminate thickness around the circumference, where some mast sections have shown different thickness in port and starboard sides. FE-simulations have been made trying to take this asymmetric thickness into account, but the results were symmetric. Another possible variation is the twist of the mast. A mast should be as straight as possible after manufacturing, but some twist may still be introduced during handling of the mast before curing the epoxy resin. Further investigations are needed to reach a final conclusion regarding all of these theories.

6.3 Out of plane waviness of fibres

The HRMA method used to measure the out of plane waviness of the fibres was written with the intent to measure the waviness of UD 0° fibres. In this project the waviness of −[13] plies was measured. The ability of the function to also be applicable to these type of laminates is promising. The length of the projection of the fibres was enough to make proper use of HRMA, a larger angle in plane would have made measurements impossible.

6.4 Compressive strength and stiffness

Due to the rather small number of specimens tested for compressive properties it is hard to draw any certain conclusions. The higher failure load in combination with the low percentage of bending indicates that the 20 mm hole diameter specimen produced a more reliable result. This fact is also apparent in Figure 5.17 where specimen 4 and 5 lie close to or within the approximated span of composite shear strength. If further testing was to be performed, this geometry in combination with more precise machining would most likely produce even better and more reliable results.

The compression test results over all are quite interesting, especially when compared to previous research in the field. Argon proved in 1972 that there exists a relation between the maximum angle and the resin shear limit of a composite (Argon, 1972). Argon based his theory on an infinite rigid kink-band, the results obtained in this study show that this theory is also applicable to a real composite. This study confirms the observations by Wilhelmsson et al. (2018) in the sense that the maximum fibre misalignment angle characterised with HRMA can be used in the Argon formula to accurately predict the compressive strength in a robust manner. It is assumed and strongly believed here that the kinking is out-of-plane, although this has not yet been verified.

6.5 Effects of corner over consolidation and varying laminate thickness

The effects of over consolidation in the corners of the mast section and variations in the laminate thickness around the section have also been studied during the thesis work. The effect of these variables were found to have very little to no effect on the stiffness of the mast when taken into consideration in the FE-simulations.

[13]Sensitive information has been censored in the published version of this thesis.

As for the over consolidation of the corners, the small influence of this phenomena can be explained by the fact that even though the laminate is thinner in the corner, the same amount of fibres must be present here, and that the reduction of thickness is caused by the fibres being more tightly packed in the laminate. This means that the same amount of fibres are acting on approximately the same distance from the neutral axis as if the corner had retained its nominal thickness throughout the corner. Therefore, one can argue that the thinning of the laminate should not have any significant influence on the overall stiffness. Unfortunately there was no time to examine the over consolidation with microscopy.

The same argument can be brought on to any variation of the thickness around the section. Even if the laminate is thicker or thinner at any location, the amount of fibres in the laminate must remain the same and the effect of varying distance to the neutral axis can be neglected. In conclusion, it is possible to model the mentioned variations. However, the time required and the added complexity to the model can not be motivated with the small influence on the results.

7 Conclusion

One of the main tasks in this master's thesis was to develop a method for modelling composite masts in the FEA software LUSAS. This has been achieved, where the method can predict the bending of a pole or mast with an accuracy of more than 85%. The method works consistently for circular poles, and for non-circular masts with some exceptions. A modelling guide has also been written for future use at Seldén Mast. It will help the company in future design work.

A consistent method to incorporate a second type of fibres to create a hybrid laminate has also been developed. This opens up the possibility for Seldén to design mid range products that have the benefits of a composite, but are not as expensive as the high end, pure carbon fibre laminates. It also means that Seldén can experiment with the stiffness of their products to tailor their behaviour to certain uses.

The use of micrography to measure the fibre waviness of a sample laminate from Seldén, in combination with the HRMA method, gave a result that confirms the observations by Wilhelmsson et al. (2018) in the sense that the maximum fibre misalignment angle characterised with HRMA can be used in the Argon formula to accurately predict the compressive strength in a robust manner. This is especially interesting since the tested laminate comes from a regular product of Seldén's, and not a laminate specifically made for testing.

The method of obtaining the compressive strength of Seldéns filament wound laminates was developed by the authors and the results indicate that the method may produce relevant results. Of the two types of slotted specimens that were tested, the strain readings show that the specimens with the smaller 20 millimetre slot were a lot less prone to bending and thus closer to pure compression. Although it is a newly developed method, it may still be of interest to further refine it.

8 Future work

There are several aspects in both parts of the thesis that are yet to be investigated. These aspects have been left out due to lack of time, or due to the fact that they lie outside of the scope of the thesis.

8.1 Stiffness modelling

As mentioned in Section 5.2, a difference in stiffness between starboard and port was noticed when testing the masts. The reason for this behaviour was not entirely established, which is why this question needs further investigation.

8.2 Compressive strength

Although the compressive tests showed signs of fibre kinking, it still needs to be confirmed that fibre kinking is the failure mode in order to validate the assumed failure criteria.

8.3 Dynamic simulations of mast and rig

Dynamic loads are accounted for in the design process of a mast at Seldén. However, simulations of the rig together with dynamic loads deriving from the sea-keeping properties of the hull in waves, as well as wind loads from the sails, is an area where further developments can be done. Such a project would require the use of theories in computational fluid dynamics (CFD), as well as in finite element analysis. Loads can be derived from CFD analysis of a hull moving in waves as well as from the pressure distribution around the sails. These loads can then be simulated in a FE software to find the response of the mast and rig. Such investigations would improve the understanding of how hull shapes and sail design influences the mast and rig. In addition, it would open up the possibility of optimisation of mast and rig, taking into account the design of hull and sails.

8.4 Modelling of torsional stiffness

Even though today, torsional stiffness of the mast is not considered to the same extent as the bending stiffness, it does, to some extent; influence the behaviour and performance of the mast. Better understanding of how the laminate can be optimised with regard to both bending and torsion would open up the possibility of cheaper, more lightweight and better performing masts. Similarly to how the bending stiffness was modelled using FE-software, and benchmarked against three point bend tests, in this project. Tests and models can be developed to derive the torsional stiffness of a carbon fibre laminate mast. Masts of special interest in such a project would be masts with an open cross-section. Such a cross-section could possibly exhibit significant warping effect, owning to the open cross-section. Investigations should be done, taking into account warping induced by the laminate coupling stiffness matrix, as well as the warping due to the properties of the open cross-section.

References

Agarwal, B. D., Broutman, L. J., & Chandrashekhara, K. (2017). *Analysis and performance of fiber composites.* John Wiley & Sons.

Argon, A. (1972). Fracture of composites. *Treatise on materials science and technology*, *1*, 79–114.

ASTM D3410/D3410M-16 Standard Test Method for Compressive Properties of Polymer Matrix Composite Materials with Unsupported Gage Section by Shear Loading (Vol. 2016; Standard). (2016). West Conshohocken, PA, USA: ASTM International.

ASTM D695 - 15 Standard Test Method for Compressive Properties of Rigid Plastics (Vol. 2015; Standard). (2015). West Conshohocken, PA, USA: ASTM International.

Bethwaite, F. (2008). *Higher performance sailing: Faster handling techniques.* Bloomsbury USA.

Fleck, B., N. A.and Budiansky. (1991). Compressive failure of fibre composites due to microbuckling. In G. J. Dvorak (Ed.), *Inelastic deformation of composite materials* (pp. 235–273). New York, NY: Springer New York.

Hajianmaleki, M., & Qatu, M. S. (2011). *Mechanics of composite beams, advances in composite materials - analysis of natural and man-made materials.* InTech.

Larsson, L., Eliasson, R., & Orych, M. (2014). *Principles of yacht design.* Bloomsbury Publishing Plc.

Lomov, S. V. (2011). *Non-crimp fabric composites - manufacturing, properties and applications.* Woodhead Publishing.

LUSAS. (2017). *LUSAS Modeller Reference Manual.* Retrieved from `http://www.lusas.com/`

Shu, J., & Fleck, N. (1997). Microbuckle initiation in fibre composites under multiaxial loading. *Mathematical, Physical and Engineering Sciences*, *453*(1965), 2063–2083.

Ugural, A. C., & Fenster, S. K. (2011). *Advanced mechanics of materials and applied elasticity.* Pearson Education.

Wilhelmsson, D., & Asp, L. (2018). A high resolution method for characterisation of fibre misalignment angles in composites. *Composites Science and Technology*, *165*, 214 - 221.

Wilhelmsson, D., Asp, L., Gutkin, R., & Edgren, F. (n.d.). *Compressive strength and waviness charaterisation of undidirectional ncf composites.* (Submitted for review)

Wilhelmsson, D., Gutkin, R., Edgren, F., & Asp, L. (2018). *An experimental study of fibre waviness and its effects on compressive properties of unidirectional ncf composites.*

A - Strain data

The strain data contains the data from all four strain gauges on one test specimen. It has been adjusted to only show the strain during the actual load application until failure.

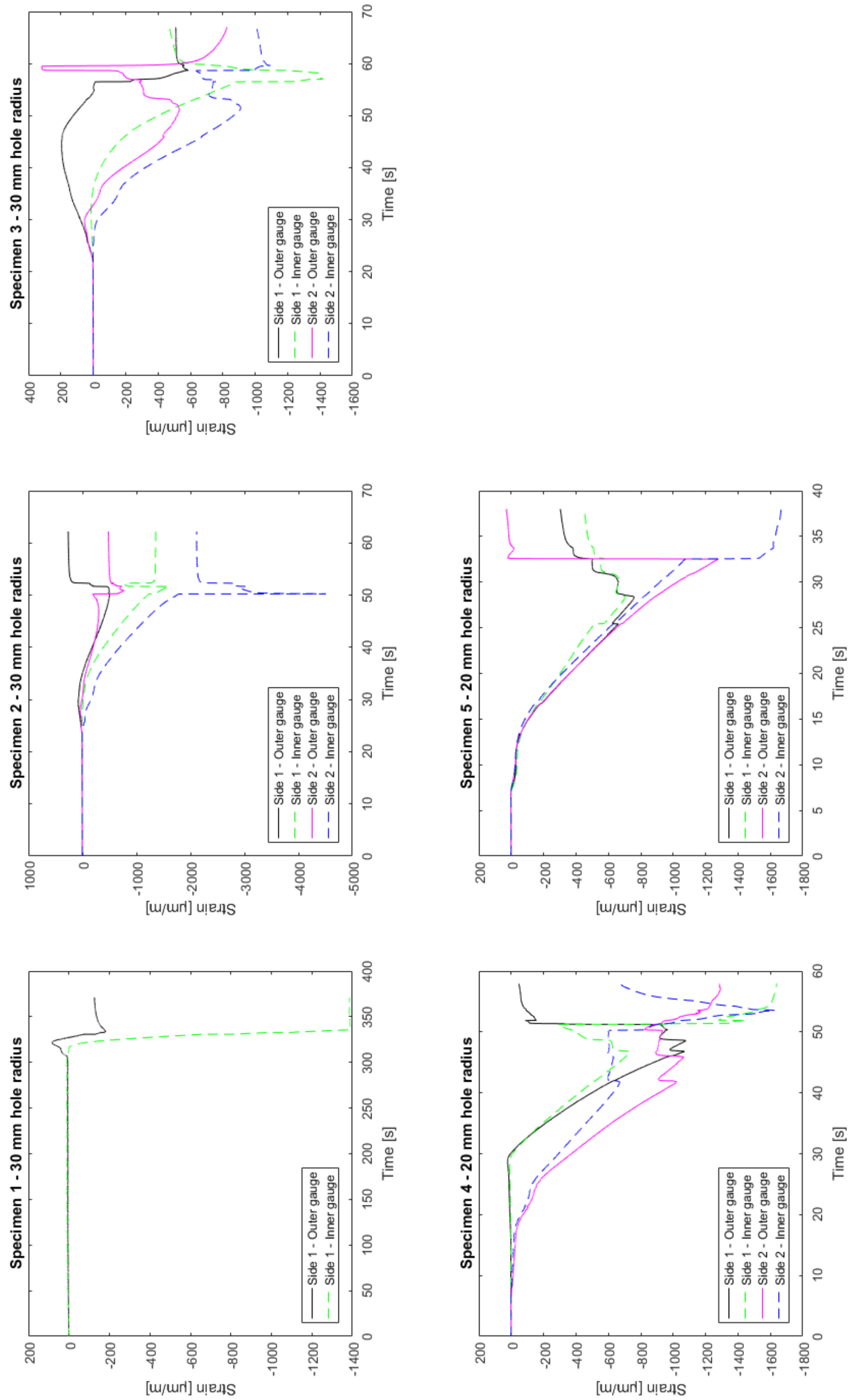

Figure A.1: Strain data for all 5 specimen with slots.

B - LUSAS Modelling Guide

Bending stiffness modelling of composite mast sections in LUSAS

Eric Eriksson

Emanuel Werner

CHALMERS UNIVERSITY OF TECHNOLOGY
Gothenburg, Sweden 2018-05-25

Contents

1 Introduction

This document will give a step-by-step instruction on how to model bending stiffness of composite mast sections in LUSAS, following the procedure developed by Eric and Emanuel in the master's thesis work in 2018.

The instruction covers everything from importing and/or creating and defining the initial geometry, applying loads and boundary conditions, to post-processing and finding the values of interest. However it is recommended to do the tutorials available in LUSAS first in order to learn the basics of the software.

In the end of the document there will be a short guide on how to use the results in hand calculations to verify the results. There is also a checklist for checking your own setup for errors or mistakes.

2 Preprocessing

In this section the FE-modelling of a thin-walled composite structure subjected to bending will be explained. The method is first and foremost meant to explain the method of modelling stiffness of a mast or a spinnaker boom. However, the method could be applied to any structure similar to these.

2.1 Geometry and Attributes

When modelling the geometry of the mast, the starting point is the geometry of the mandrel on which the mast in question is wound on. The outline of the mandrel section is imported into LUSAS. Figure 1 shows the mandrel outline, as it is when imported into LUSAS

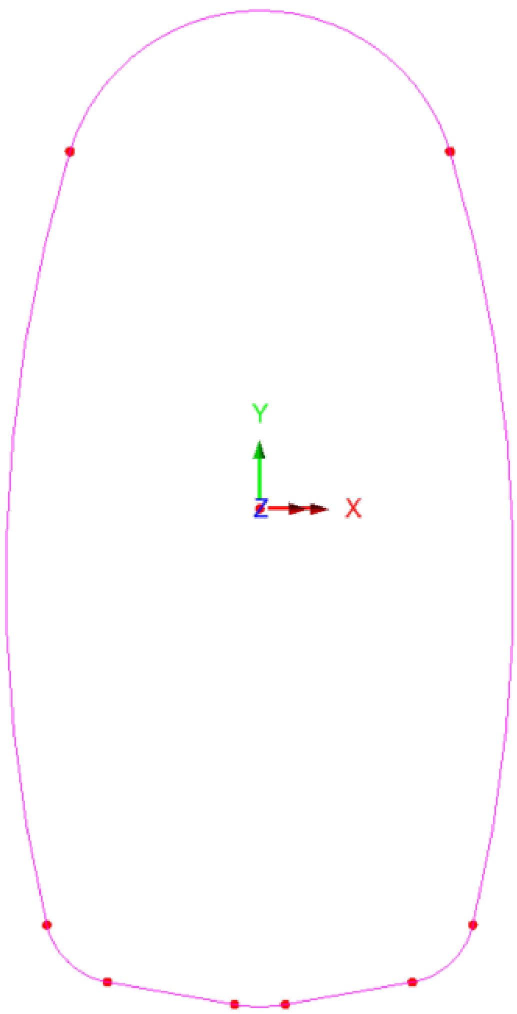

Figure 1: Mandrel outline as imported into LUSAS.

LUSAS might experience some difficulties with the imported geometry. According to the LUSAS support this is a known issue when importing geometry from AutoCAD into LUSAS. LUSAS says that they have initiated a change request to solve this problem. Hopefully in future versions of the software this is not an issue anymore. However, the easiest way to solve this problem at the moment is simply to redraw the geometry using the imported geometry as a template.

As the outline is redrawn points are added on the section sketch to represent the B-lines, the fore line and the aft line. Further points are also added to represent the areas of the mast that are reinforced with UD tapes. Figure 2 shows the original points, together with all the points added in the redrawing.

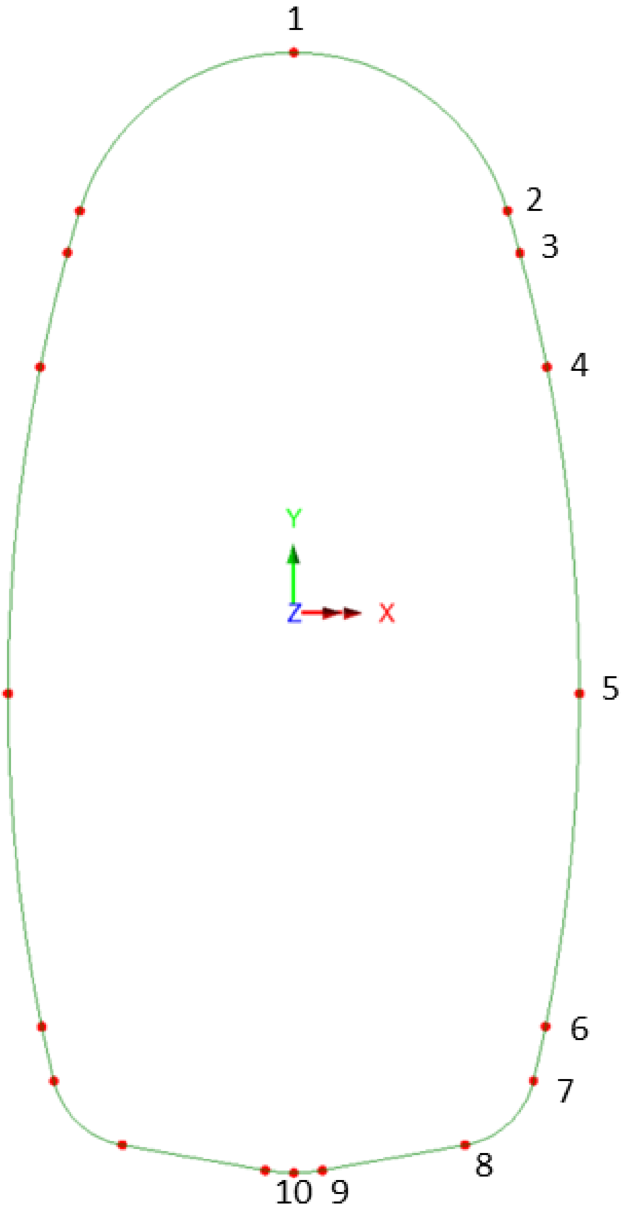

Figure 2: Redrawn mandrel outline.

Some of the points in Figure 2 are the original points from the imported geometry while others are added in the process of redrawing the outline in LUSAS. The mast section shown in Figure 2 has UD tape reinforcements on all four sides. The width of these reinforcements is known, why they can be defined in the section geometry. Later on, composite layups will be defined to represent the UD reinforcements, see Section 2.4 for more on defining composite layups. Further, both aft, forward and B-lines are added into the section geometry as points. Below follows a list with detailed information on each point in Figure 2.

Point 1 defines the forward line of the mast.

Point 2 defines the width of the forward UD tape reinforcements.

Point 3 is a point from the original imported geometry.

Point 4 together with **Point 6** defines the width of the starboard and port UD tape reinforcement.

Point 5 defines the location of the B lines.

Point 6 see **Point 4**. Also defines the width of the aft UD tape reinforcements.

Point 7 Point from the original imported geometry.

Point 8 Point from the original imported geometry.

Point 9 Point from the original imported geometry.

Point 10 Defines the aft line of the mast.

Since the structure can be considered to be thin-walled it will be modelled using surfaces. The surfaces are created by sweeping the lines and points that make up the cross-section of the mast to the desired length. When creating the surfaces by sweeping, it is important to keep in mind where the loads and supports are located. Most often, to be able to apply either a load or a support at a certain location on the geometry, either a point or a line will be needed at this location. In Figure 3, a mast is shown where the load is applied on a line located at the mid-span between the supports. In the same figure the supports are defined by points located on the bottom surface of the mast. The figure shows one example on how points and lines can be used to create geometry that later on will be used to define loads and supports. In Figure (3) the geometry was created by sweeping the lines of the mast section four times.

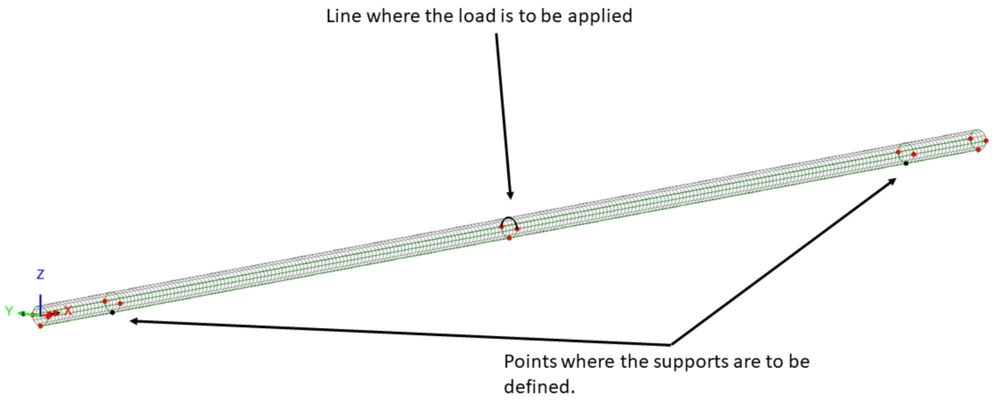

Figure 3: Lines and points used to define load and supports.

The surfaces need to be assigned a thickness. To do this got to: *Attributes > Geometric > Surface*. The dialog window in Figure (4) below will appear.

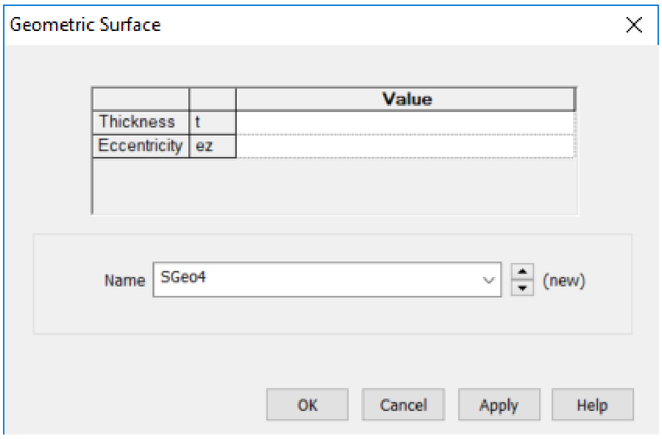

Figure 4: Definition of surface thickness and eccentricity.

The wall thickness of the mast section is entered in the field *Thickness*. Since the mast section was drawn with the mandrel as reference, all surfaces will automatically be the inner surfaces of the section. LUSAS will model the laminate using these surfaces as mid-surfaces if nothing else is specified. This means that surfaces need to be given an eccentricity of half the laminate thickness. In the field *Eccentricity* enter the value:

$$ez = \frac{-t}{2}$$

In this equation, t is the wall thickness of the surface. The normals of the surfaces should be pointing outwards and away from the midpoint of the mast section. If this is the case, given that the eccentricity is negative, the thickness of the surface is moved outwards, as intended. See Section 2.6.3 on how to orient the normals of the surfaces. To check if eccentricity is correct turn on *Fleshing* and observe in what direction the thickness of the surface is moved when the eccentricity value is entered. Figure 5 below shows the surfaces of a section with the correct eccentricity. The red points reveal the location of the surfaces.

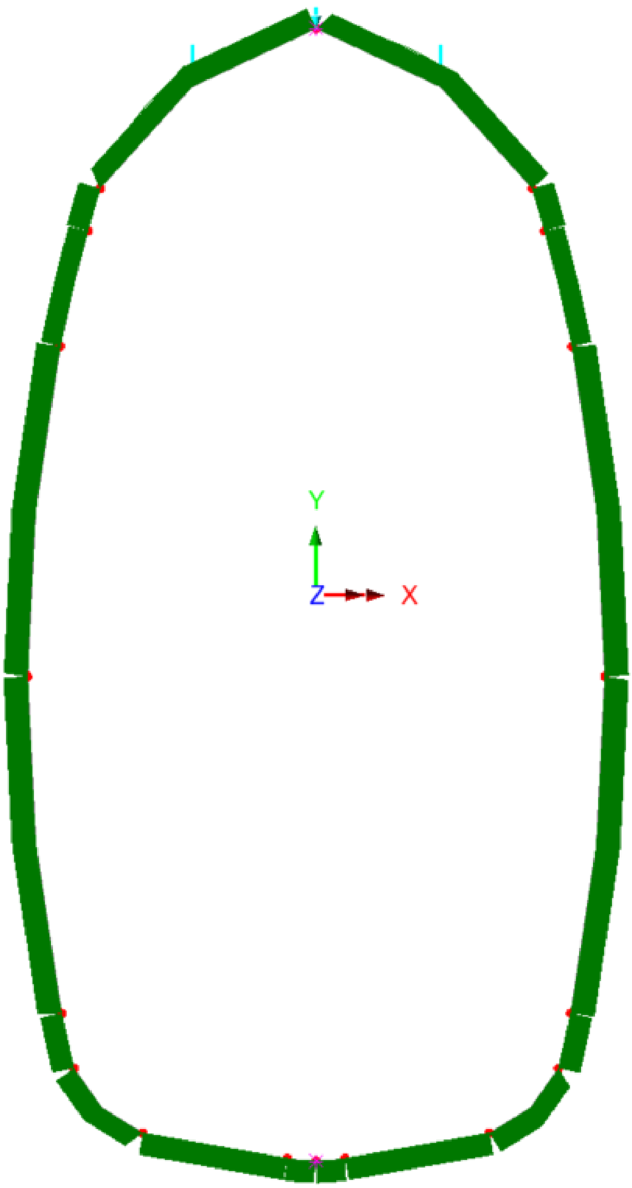

Figure 5: Correctly defined eccentricity.

2.2 Effects of corner over consolidation and varying laminate thickness

In the master thesis work written in ad junction to this modelling guide the effects of over consolidation in the corners of the mast section and variations in the laminate thickness around the section was studied. The effect of these variables were found to have very little to no effect on the stiffness of the mast.

As for the over consolidation of the corners, the small influence of this phenomena can be explained by the fact that even though the laminate is thinner in the corner, the same amount of fibres must be present here, and that the reduction of thickness is caused by the fibres being more tightly packed in the laminate. This means that the same amount of fibres are acting on approximately the same distance from the neutral axis as if the corner had retained its nominal thickness throughout the corner. Therefore one can argue that the thinning of the laminate should not have any significant influence on the overall stiffness.

The same argument can be brought on to any variation of the thickness around the section. Even if the laminate is thicker, or thinner; at any location the amount of fibres in the laminate must remain the same and the effect of varying distance to the neutral axis can be neglected. In conclusion, it is possible to model the variations mentioned in this section. However, the time required and the added complexity to the model can not be motivated with the small influence on the results.

2.3 Composite Material Definition

The carbon reinforced plastic is defined as a solid orthotropic material in LUSAS. To do this go to: *Attributes > Material > Orthotropic*

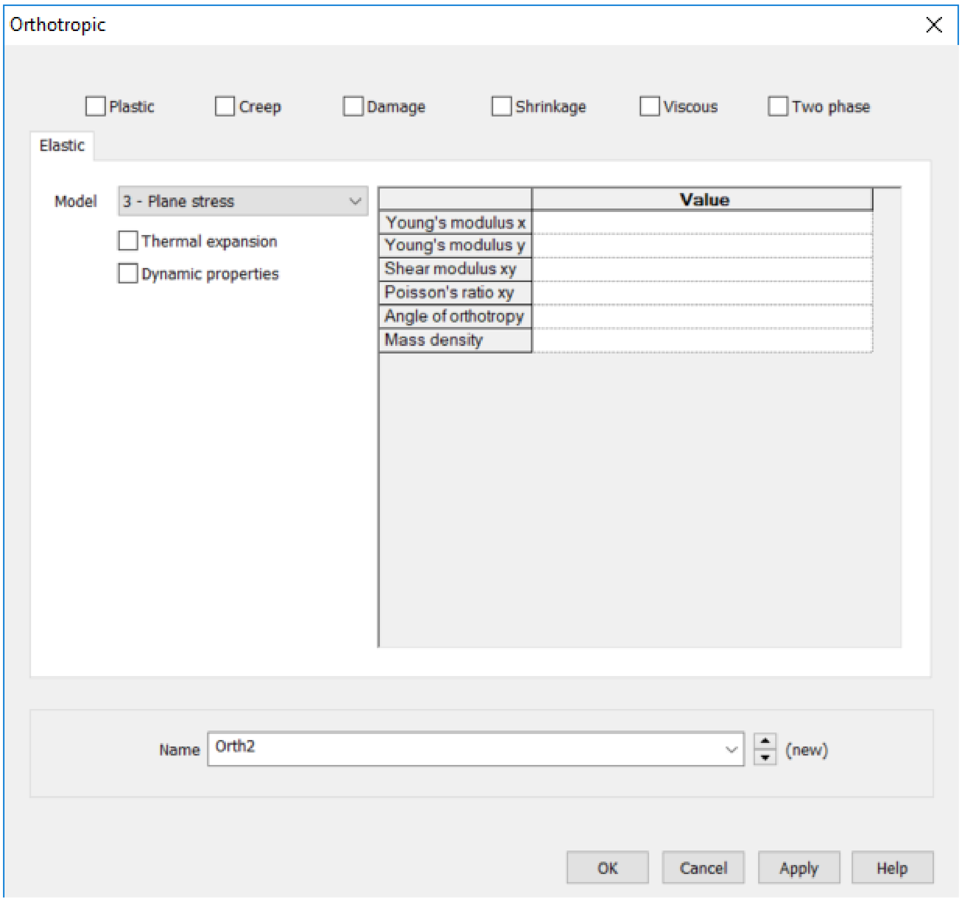

Figure 6: Plane stress orthotropic material definition dialog window.

By default LUSAS will open the dialog window for a Plane stress material model shown in Figure 6. Change the material model to *Solid* from the drop down menu to the left in the window.

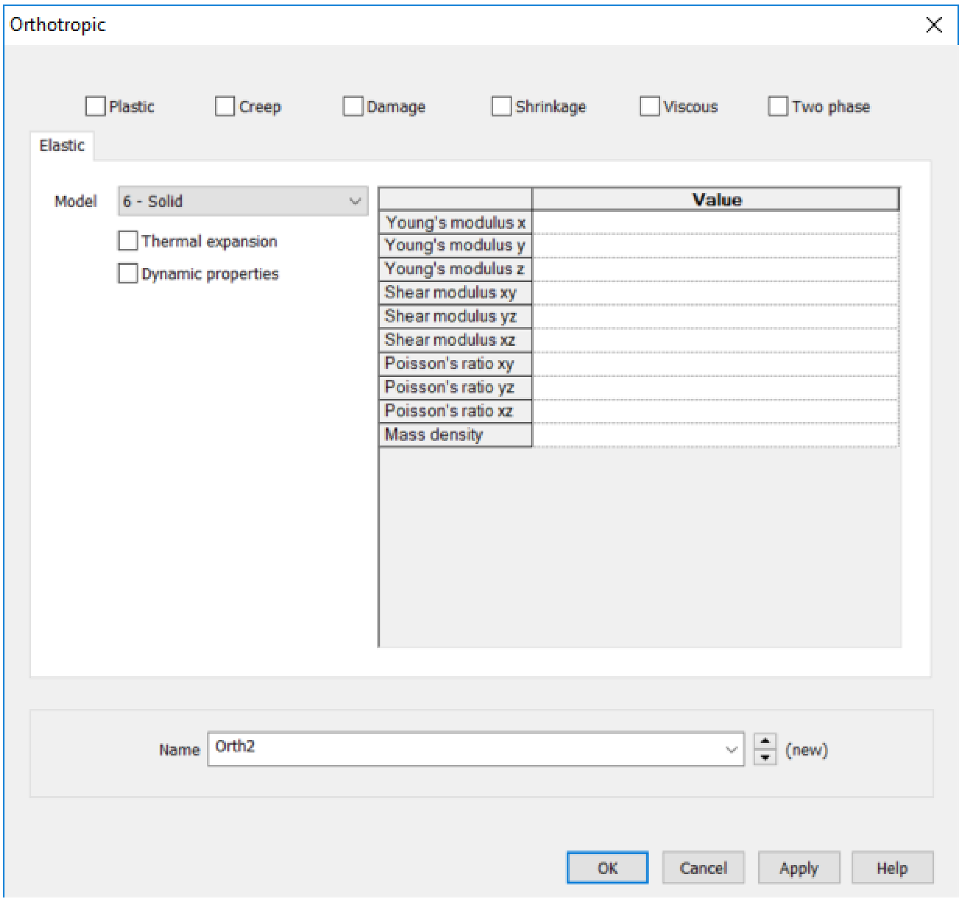

Figure 7: Solid orthotropic material definition dialog window.

This will open the dialog window shown in Figure 7. In Table 1[1] the material data to be entered into the window in Figure 7 is shown. If the model is in millimeters (which is usually the case), be aware that *Mass density* must be entered in the unit t/mm^3 and the modulus must be entered in MPa here.

Table 1: T700/UF3325 Material data

	Value
Young's modulus x	- MPa
Young's modulus y	- MPa
Young's modulus z	- MPa
Shear modulus xy	- MPa
Shear modulus yz	- MPa
Shear modulus xz	- MPa
Poission's ratio xy	-
Poission's ratio yz	-
Poission's ratio xz	-
Mass density	- t/mm^3

[1] Censored for publication.

Name the laminate material after its constituents i.e *fibre name/resin name*. To finish editing the material click OK in the dialog window.

2.4 Composite Layup Definition

To define a composite layup go to: *Attributes > Composite*.

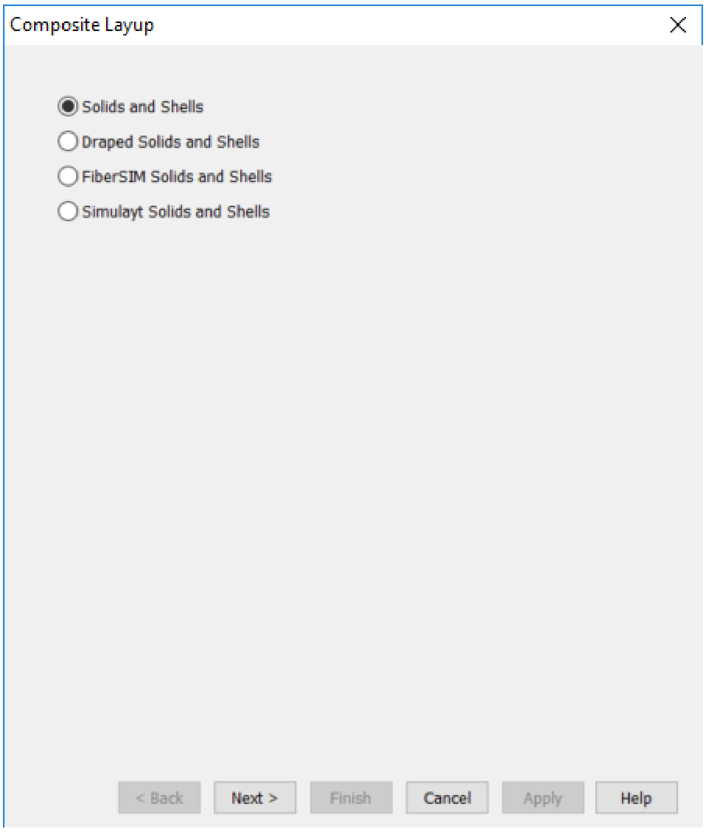

Figure 8: Selecting the type of composite layup to be created

The window shown in Figure 8 will appear. Select *Solids and Shells* and click *Next* to proceed.

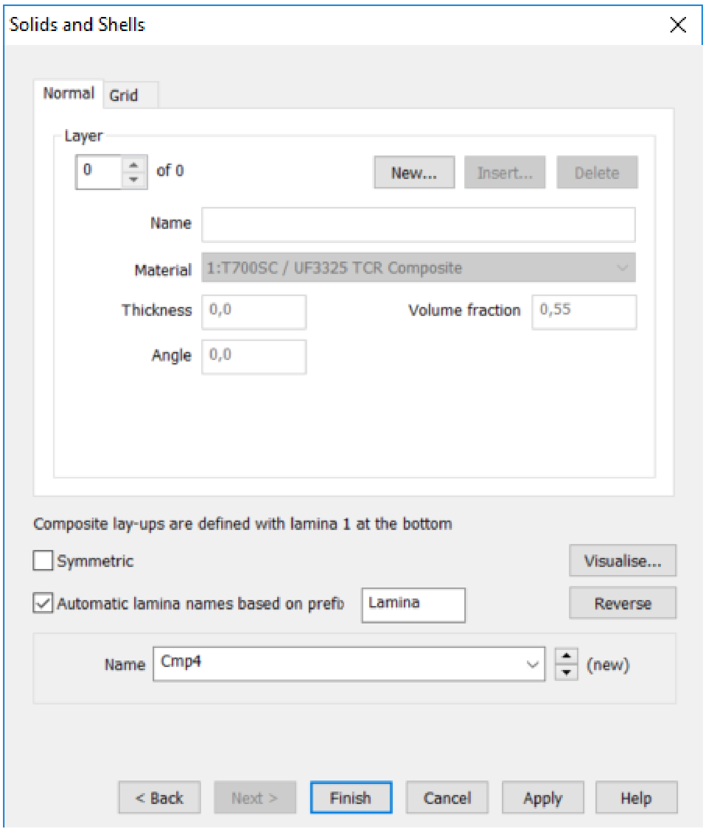

Figure 9: Composite definition dialog window

Figure 9 shows the composite layup definition dialog window. In LUSAS layups are defined from bottom to top in the same direction as the normal of the surface that the layup is assigned to. See Section 2.6.3 for more on normals and normal orientation.

Start defining the first layer by clicking *New* at top right. To define a layer, enter a name for each layer in the *Name* field. From the *Material* drop down list select the material to be assigned to the layer. In the *Thickness* field enter the layer thickness as a fraction of the total number of layers according to:

$$\text{Thickness} = \frac{1}{\text{Total no. of layers}}$$

In *Angle* enter the fibre orientation of the current layer in degrees, relative the long axis of the mast. The *Volume fraction* field is optional and will not influence the solution in the analysis intended for this model. To finish the current layer and start defining next click *Apply* in the bottom right of the window and repeat the process for the next layer. When all layers have been defined click *Finish* to close the dialog window. To inspect or change the definition of the layup right click on the layup in the *Attributes* tree to open the dialog window again. In the top right corner it is possible to toggle through the layers to view or edit them individually. *The Visualize* button gives a visual overview of the layup.

To assign the layup to a surface simply select the surface to which the layup is to be assigned and drag and drop the layup from the *Attributes* tree. The dialog window shown in Figure 10 will appear.

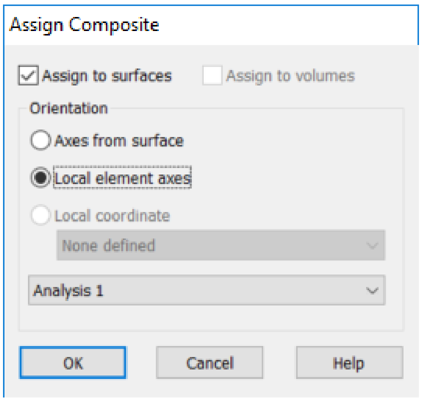

Figure 10: Composite assignment dialog window

Important! Make sure that *Assign to surfaces* is selected and that the orientation of layup is set to *Local element axes* as shown in Figure 10. This option makes sure that the layup uses the orientation of the element axes as reference for the fibre angles. Consequently, the orientation of the element axes must be correct for the fibre angles to be correct. See Section 2.6.3 on how to orient the element axes.

If the mast has UD reinforcements the easiest way to include these in the model is to create several composite layups, following the same procedure as previously. In Figure 28a[2] a nominal layup is shown next to an UD reinforced layup in Figure 28b[2] where the UD reinforcements are visualized as yellow blocks in the stack.

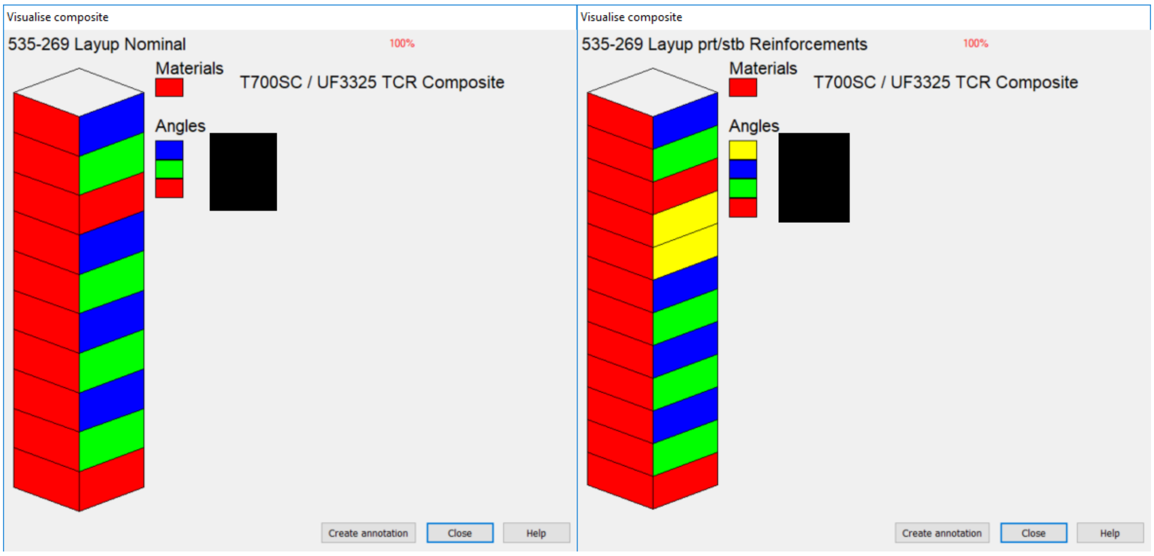

(a) Nominal composite layup **(b)** Reinforced composite layup

Figure 11: Examples on nominal and reinforced composite layups

The layup including the reinforcements is then assigned to the surfaces where the UD tapes are located on the mast, and the nominal layup is assigned to all surfaces with no reinforcements. In Section 2.1

[2] Censored for publication.

surfaces where UD reinforcements are located were defined by adding points on the geometry of the mast section. Remember to also adjust the thickness in the areas where additional fibre layers have been applied.

2.5 Loadcase

The loadcase is defined as the applied load and the boundary conditions of the geometry. In this section only the load types and boundary conditions used in the thesis will be described. They are based on a beam that is freely supported at both ends, loaded in three-point bending by hanging a weight in a strap around the circumference of a mast or boom. The load is applied centered between the supports.

2.5.1 Boundary Conditions

To avoid any distortions or unnatural behaviour of the mast close to the supports, the boundary conditions are applied in single points (such as Point 10 or 5 in Figure 2), instead of along a line or on a surface.

One support will be fixed in translation in all directions, as well as rotation around the long axis of the mast. The other support will have the same settings except that it will be allowed to translate along the axis of the mast. In Figures 12 and 13 the z-axis aligned with the long axis of the mast.

To define a support, go to *Attributes > Support* and apply the settings shown in Figures 12 and 13.

Figure 12: Settings for right support.

Figure 13: Settings for left support.

2.5.2 Applied Loads

The load is applied as a line load in the position on the mast where the actual load would be applied. In the case of a circular cross-section, the line would run across the tube along the upper half of the circumference. If the line is not split in several parts, the load can be applied as *Global Distributed*.

To create a load, go to *Attributes > Loading* and pick *Global Distributed*. The dialog window should look similar to the one shown in Figure 14.

Example: If the load is 20 kg, the load will be defined as a total global load of 196.4 N. LUSAS will then take care of the distribution along the line.

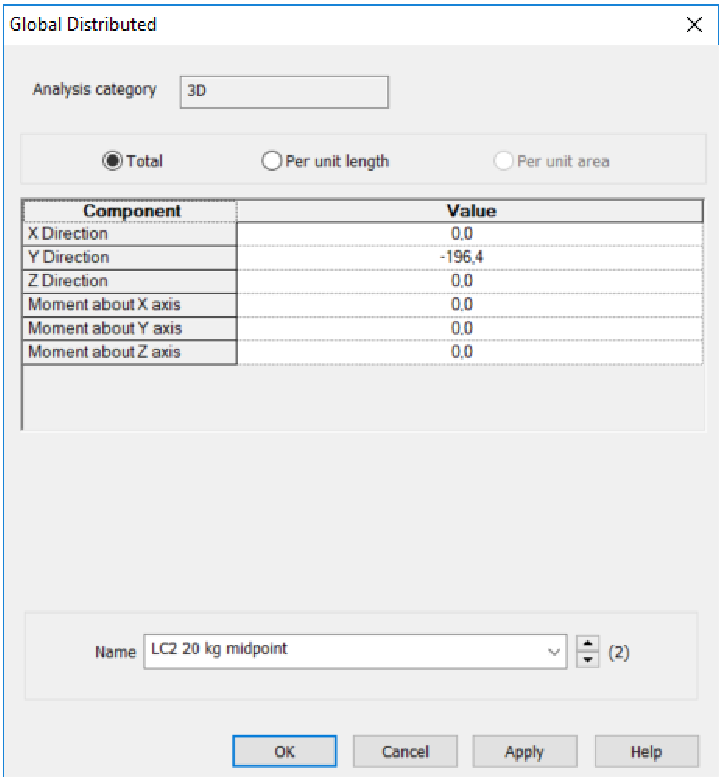

Figure 14: dialog window for defining a load.

If the upper half of the circumference of any cross-section is split into several smaller lines of differing size as in Figure 15, the easiest way to apply the load is to sum the length of the lines, divide the total applied force per unit length and then define the applied load as *Per unit length*. The load distribution will then be correct for that specific group of lines. To see the length of a line, hover the mouse pointer on top of it. This is also shown in Figure 15.

Example: The applied load is 20 kg. Several smaller lines make up a total length of 85 mm. The load per unit length is then 196.4 N divided by 85 mm, 2.31 N per unit length. To apply this load correctly, select all the lines that make up the total line, and apply the unit length load.

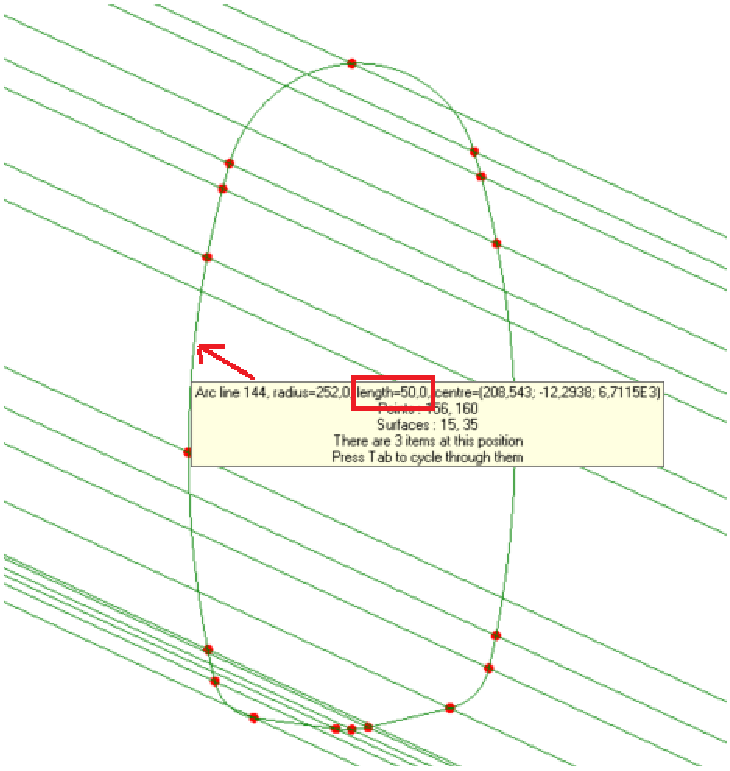

Figure 15: Division of lines and how to see their length.

If desired, gravity can also be applied on the entire model. Gravity is defined by clicking *File > Model Properties*. The dialog window in Figure 16 should appear. Gravity is defined in mm/s^2. In order for the analysis to take gravity into account, it also needs to be explicitly applied in the loadcase. Do this by right-clicking the loadcase in the Analysis tree and mark *Gravity*.

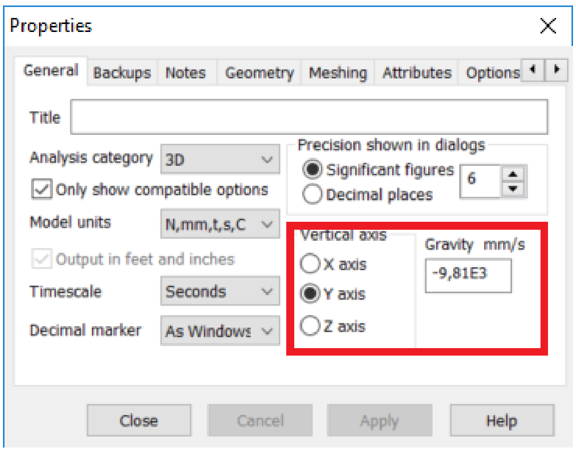

Figure 16: Dialog window for defining model gravity.

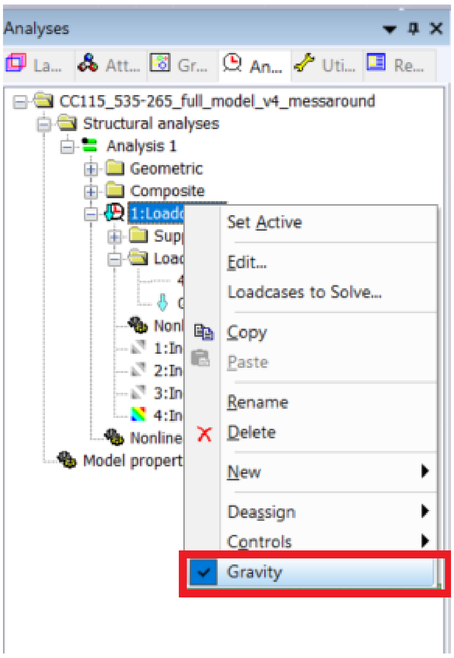

Figure 17: Applying the gravity option to the loadcase.

Note! Applying gravity demands a correct density of the material used in the model to give a correct result.

When defining any load, make sure that it is applied in the desired direction. Check along which axis it is applied, and if it should be defined as negative or positive.

2.6 Meshing

The meshing of the model defines the element type to be used in the analysis as well as the grid size of the mesh. Making a bad choice for the mesh can give bad results.

2.6.1 Elements and Limitations

The elements that have been used in all analyses are quadrilateral shell elements with quadratic integration points (QTS8). These elements are suitable for thick-shelled geometry with little or no out-of-plane stresses.

To define the elements to be used in the mesh, go to *Attributes* > *Mesh* > *Surface*. Apply the setting according to Figure 18.

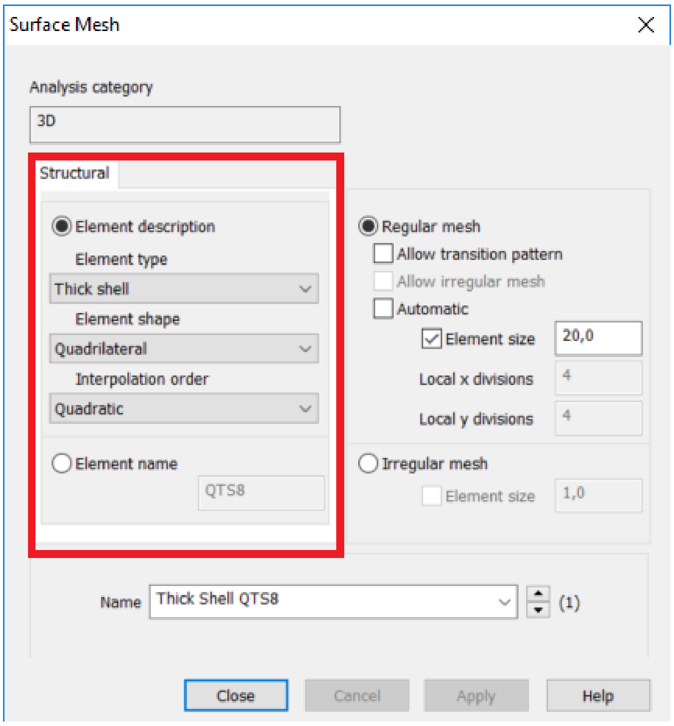

Figure 18: Mesh settings dialog window.

2.6.2 Element size and Convergence

The element size should be chosen such that the elements do not have an aspect ratio that is too large, i.e. one side should not be excessively larger than the other. If this is the case in any point of the mesh, the solver will give warnings. Choose element size so that the elements are close to square and the solver gives no warnings.

The grid size should also be chosen such that the results have converged and are size-independent. To check this it is recommended to do a convergence check where the element size is incrementally lowered until the results do not change with a change in element size. The result to be checked can be any result, e.g. the mid-point deflection or maximum stress.

The grid size of the mesh is controlled with the settings shown in Figure 19, found by going to *Attributes > Mesh > Surface*, or by editing an already existing mesh attribute. Figure 20 shows an element that will most likely render a warning in the solver due to the high aspect ratio.

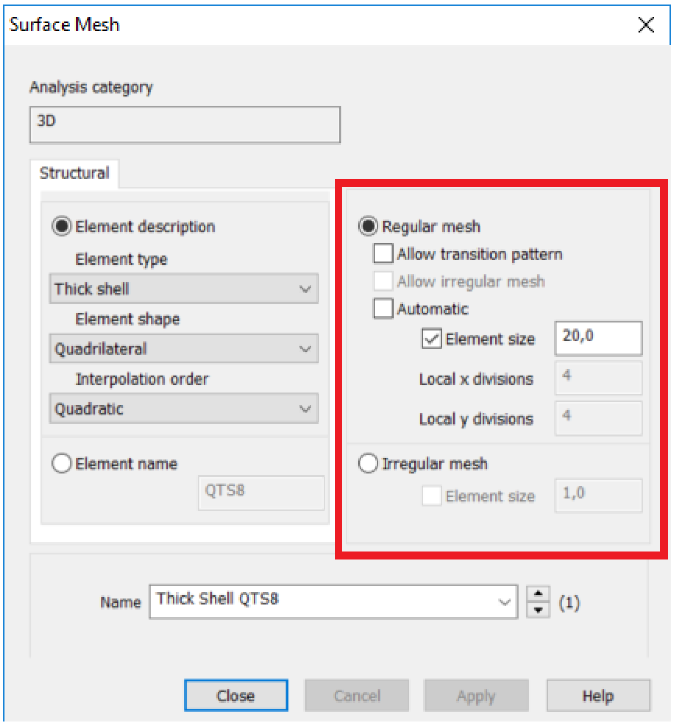

Figure 19: Mesh element axes.

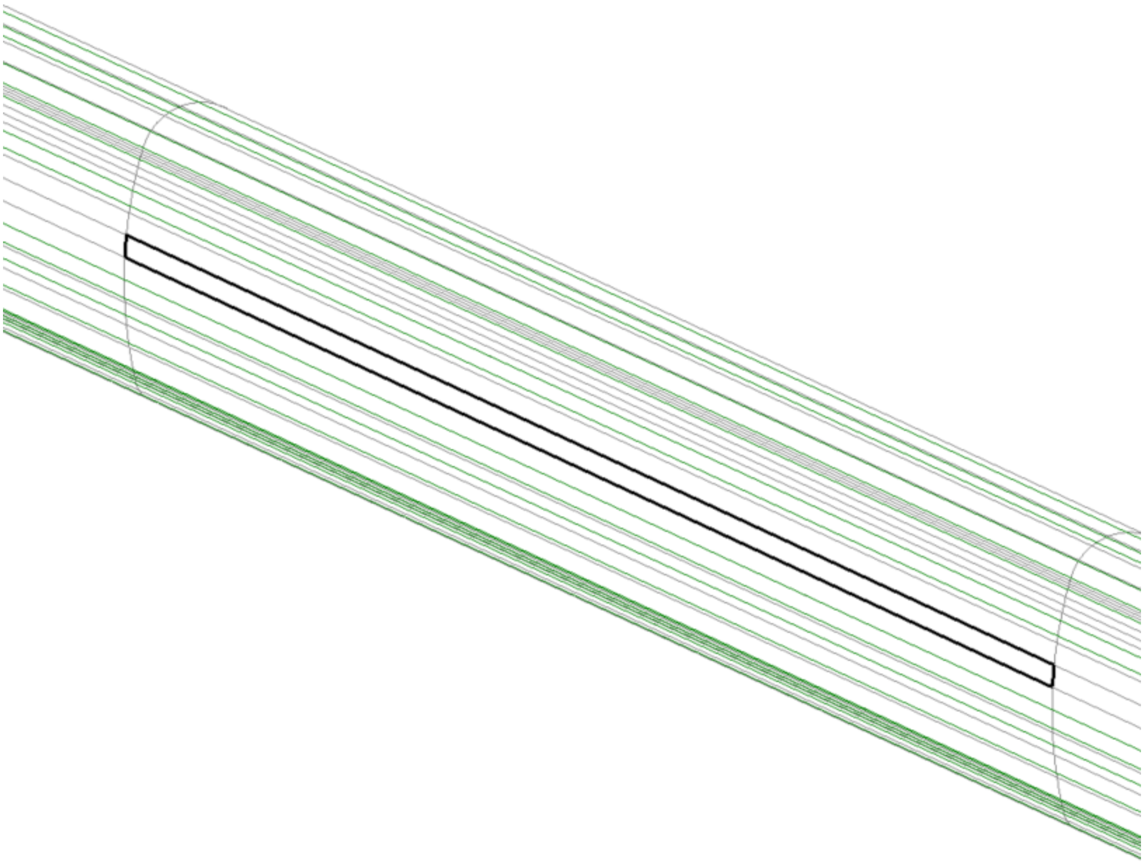

Figure 20: Bad element with high aspect ratio.

2.6.3 Element orientation

In Section 2.4 the Composite layup was set to use the local element axes as reference for the fibre angle. To visualize the element axes *make sure that the model is meshed.* Right click on *Mesh* in the *Layers tree* and select *Properties.* The following window will appear Figure 21

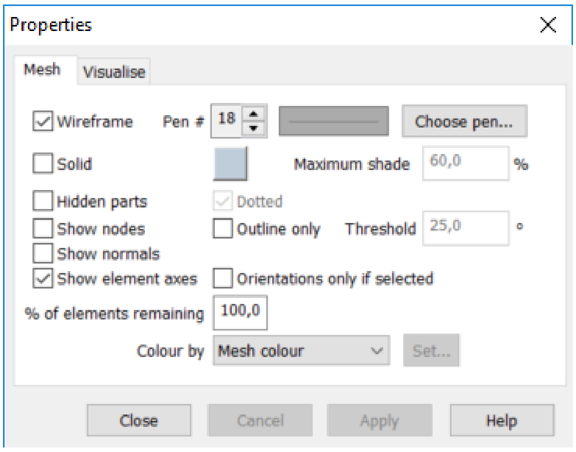

Figure 21: Mesh element axes.

Make sure that the *Show element axes* box is selected and click *Apply*. The element axes will now appear on the mesh as shown in Figure 22.

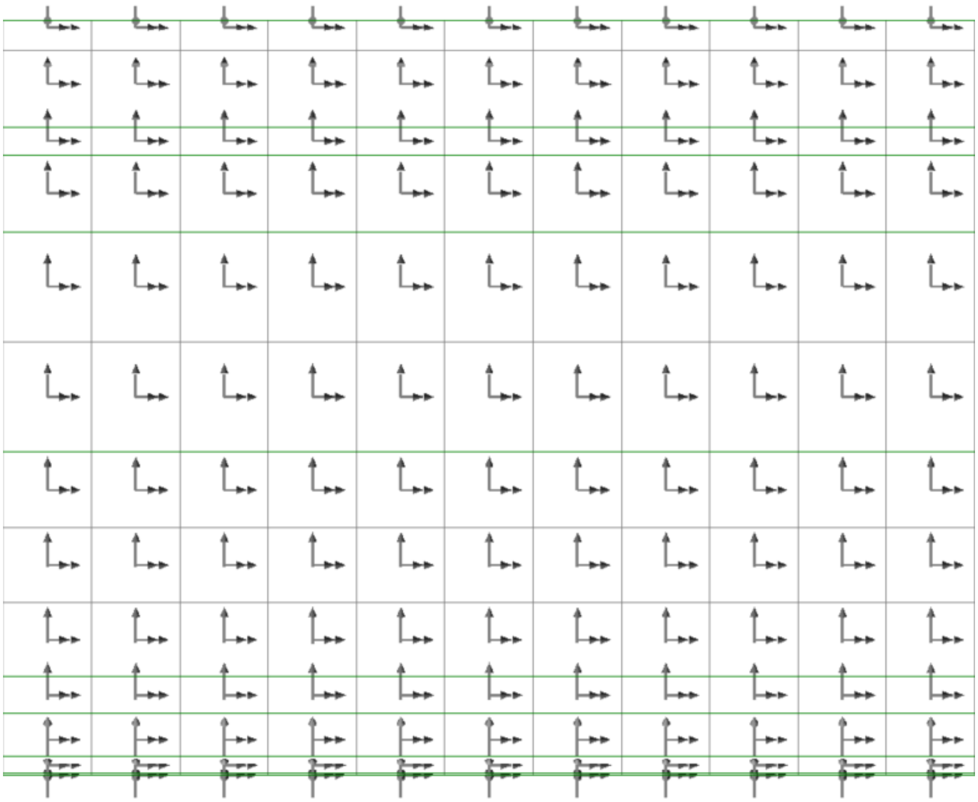

Figure 22: Mesh element axes.

For consistent modelling reasons the normal's of all surfaces on the mast should be pointing outwards away from the midpoint of mast section. To reverse the normal of a surface: *select the surface* you wish to reverse and go to: *Geometry > Surface > Reverse.* Repeat the process until all surfaces are pointing outwards as shown in Figure 23

Tip! Every time a surface is reversed (or cycled) the mesh has to be recalculated. To reduce the calculation time of each reverse operation, temporarily change the mesh size to a larger element size.

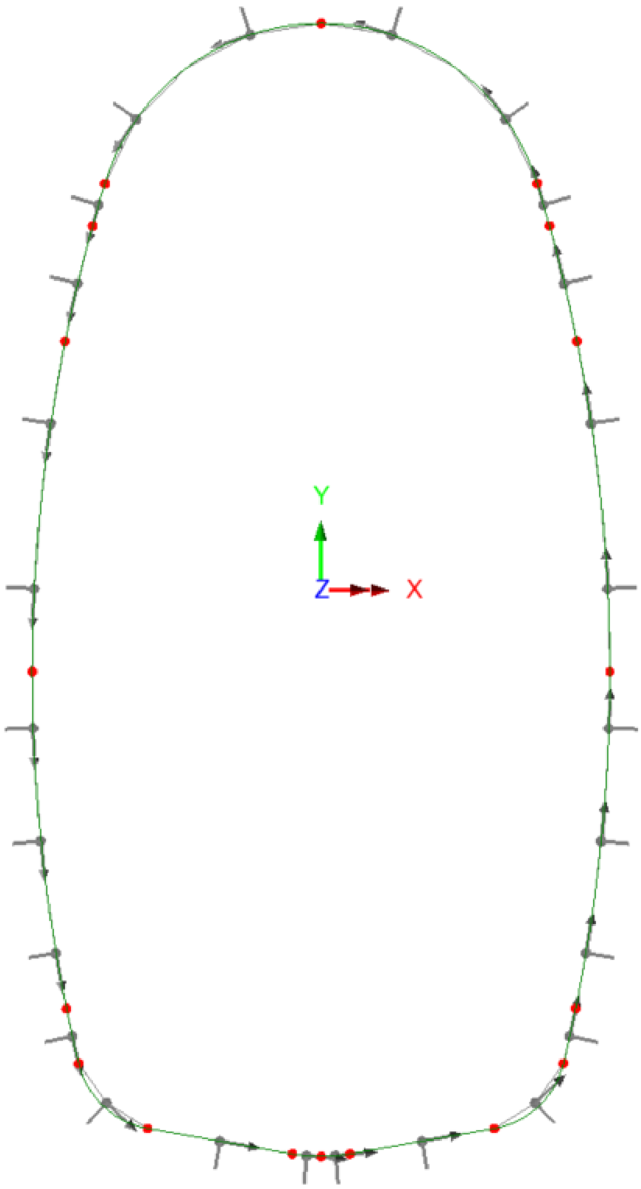

Figure 23: Correct surfaces normal orientation.

In Section 2.4 the fibres of the composite was set to use the orientation of the element axes as reference. Consequently, to get the correct orientation of the fibres, correct orientation of the element axis must be achieved. To have consistent fibre orientation in the model, all double headed arrows (Figure 22) must be aligned with the long axis of the mast. Usually this is achieved by manually changing the orientation of all surfaces in the model. To change the orientation of a surface: *select the surface* you wish to change the orientation of, and go to *Geometry > Surface > Cycle*. The following window will appear:

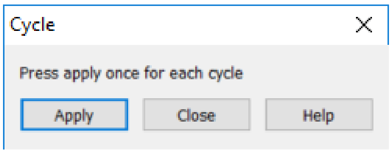

Figure 24: Surface cycle dialog window.

Click *Apply* to cycle the surface until the double headed arrow is aligned with the long axis of the mast. Repeat the process until the double headed arrow of all surfaces in the model is aligned, in the same direction, with the long axis of the mast.

With the settings specified in this document, LUSAS uses the axis marked with a double headed arrow as reference for the fibre angle. This means that a composite layer with 0° fibre angle will be aligned with the double headed arrows as shown in Figure 25, where the fibre direction is visualized with purple arrows, on top of the element axes plotted with grey arrows.

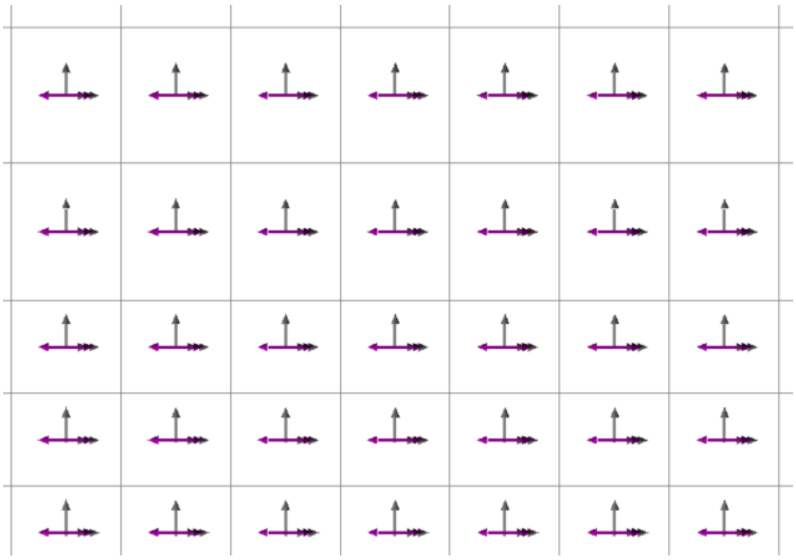

Figure 25: Composite 0° fibres .

Figure 26 on the other hand shows a surface with −° fibres visualized with purple arrows.

Figure 26: Composite −° fibres .

To visualize the fibre orientations as in Figure 25 and 26 right click on *Attributes* in the *Layers* tree and click on *Properties*. In the window that appears click on the *Composite* tab to get to the window shown in Figure 27 below.

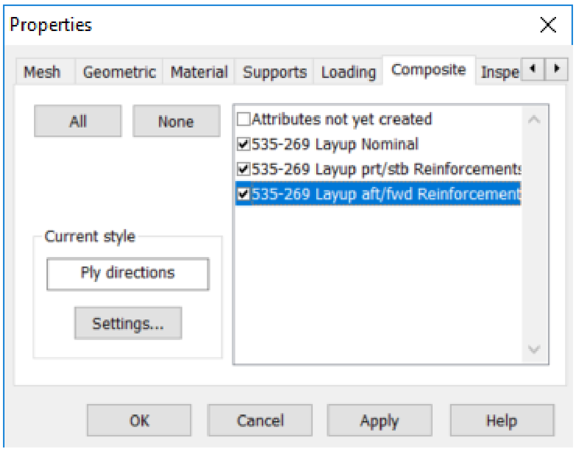

Figure 27: Fibre visualization dialog window.

Select all the Layups in the list and click *OK*. Then go to the *Attributes tree* and expand the layup you wish to visualize by clicking on the plus sign next to the name of the layup. Right click on the layer you wish to visualize in that layup and select *Set Lamina Active* as shown in Figure 28[3]

[3]Censored for publication.

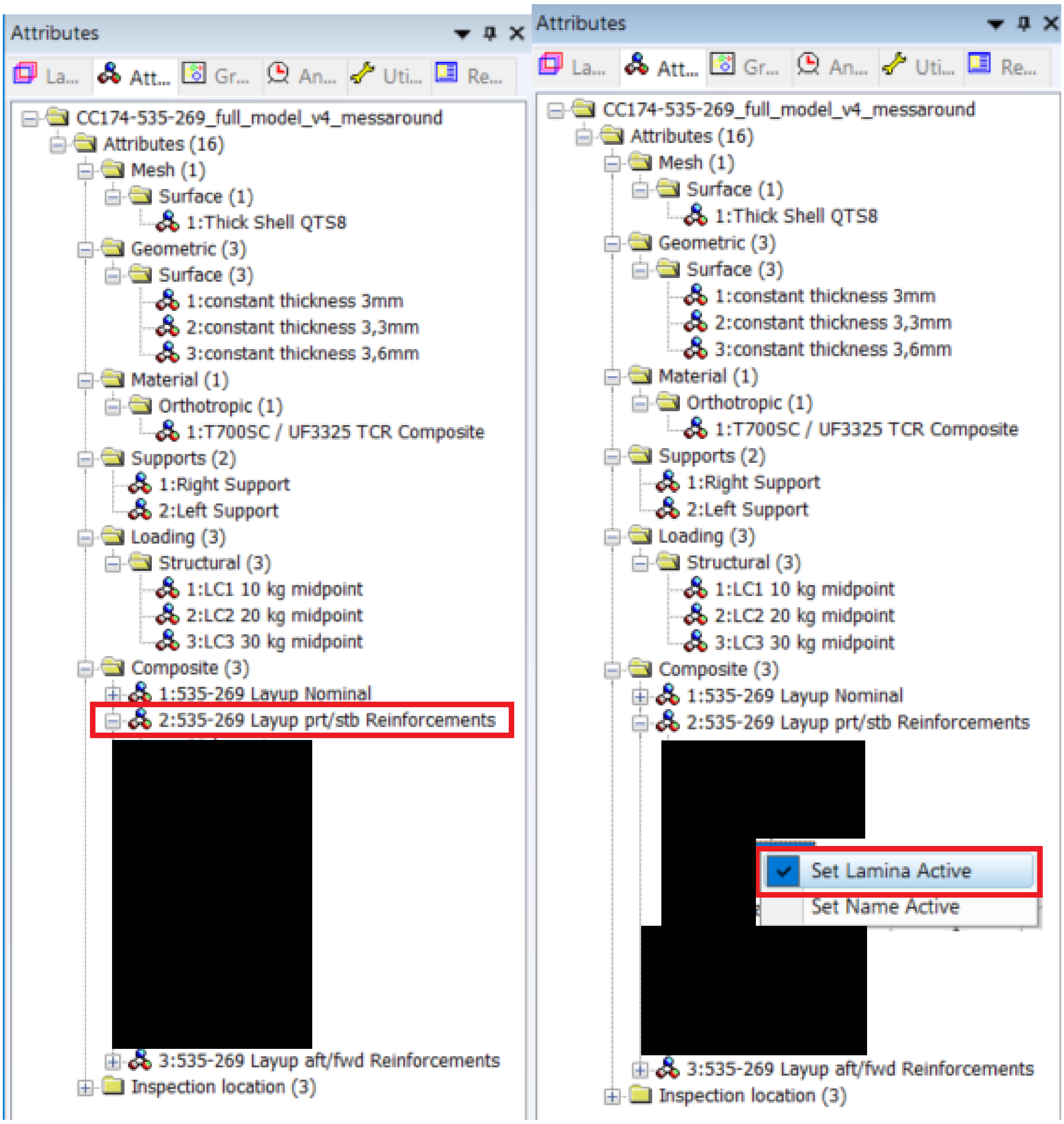

Figure 28: Visualizing a certain layer in the model.

Only one layer layer in one layup can be active at a time. To inspect another layer in the same or another layup, simply repeat the process for that layer.

2.7 Solver Setup

The solver is set up before starting the analysis to assure quick and good convergence. Applying bad settings can result in an analysis that exits with errors or that takes unnecessarily long time to finish.

2.7.1 Non-linear controls

All analyses have been run as non-linear and transient in order to catch any non-linear behaviour in connection to the deformation of the cross-section of the mast. This means that the analysis will be run in several increments from almost no load up until the nominal load defined in the model setup. In order to get the analysis to run smooth and converge easily, a number of setting should be changed. These settings have been recommended by the technical support at LUSAS. The nonlinear controls are accessed by right-clicking *Nonlinear and Transient* found in the *Analysis* tab in the treeview, shown in Figure 29.

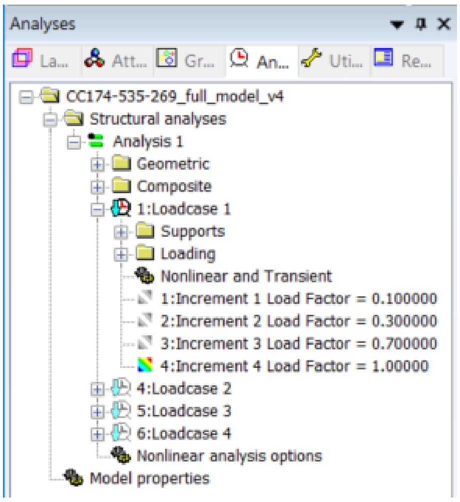

Figure 29: Nonlinear controls are found in the analysis tab in the treeview.

Use the same settings as the ones shown in Figure 30. The settings below mainly aim to:

- Remove arc-length solution by setting it as zero.
- Start with a load factor of 0.1, which can increase without restriction (o) until final solution reaches total load factor of 1.
- Adjust load factor based on how "easy" or how "difficult" it was to converge in the first 4 iterations of an increment.
- Set a more generous threshold of 0.5% for the residual force norm. This decides how good the convergence needs to be for the analysis to move on to the next load increment.
- Ignore the incremental displacement norm (0), as it is the **total** displacement norm that generally matters.

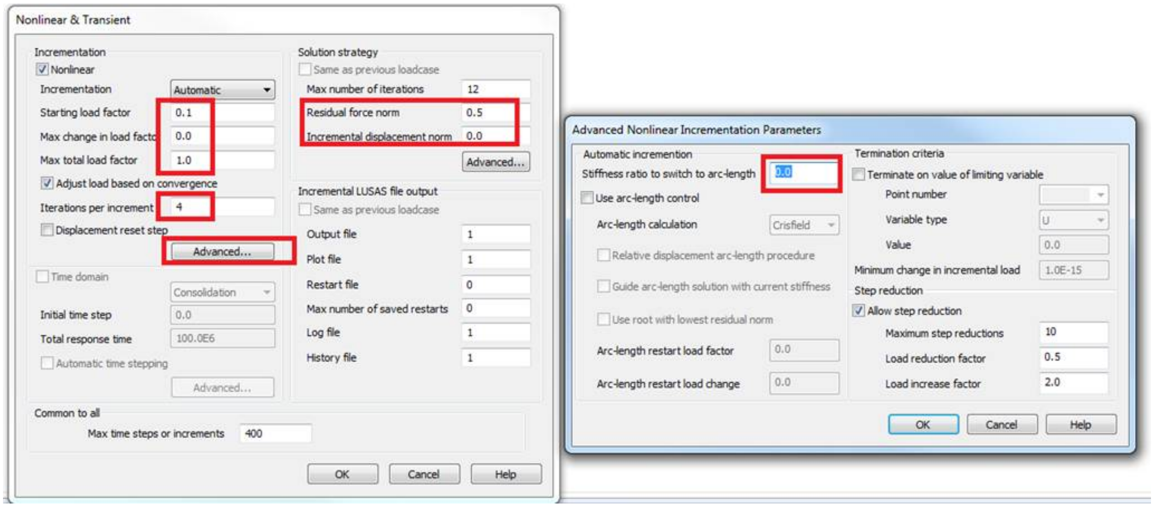

Figure 30: Nonlinear controls.

Apart from this, a suitable mesh should have already been defined in the previous steps.

2.7.2 Inspection Locations

LUSAS gives the user the possibility to define specific inspection locations on the geometry where the value of any parameter can be checked easily. This has been used in the thesis work to check the deflection in two points on the bottom of the mast, to the left and right of the beam midpoint.

The inspection location(s) have been applied to existing geometry, either in points or on lines. To apply an inspection location to a point, go to *Attributes > Inspection Locations*. The dialog window that appears is shown in Figure 31.

In the dialog window you can choose to use either a Point, Line, Surface or Volume for the assignment. If you choose *Assignment to Point* you press OK, select which point(s) you want to Inspect and then drag and drop the inspection point in the same manner as the other attributes.

If the inspection location is to be placed somewhere on a line, select the *Line* radio button and define the *Distance type*. The distance can either be defined as an actual distance along the line, or as a fraction of the total line length.

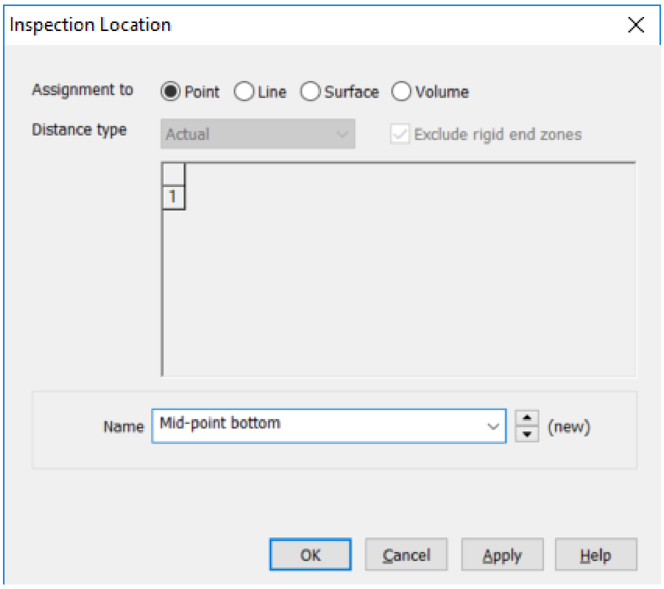

Figure 31: Inspection Location dialog window.

3 Post-processing

Post-processing is carried out a after the analysis has been run. Most steps are the same regardless of the analysis.

3.1 Contour plot

To view the results of the analysis, right-click in the graphics window and select *Contour*. To view results in specific layers of the laminate layup, maximise it in the treeview and right-click the lamina of interest. Click *Set Lamina Active*.

3.2 Model mass check

The mass of a model can easily be accessed from the model tree view after the analysis has been run. The mass is printed in the model output file, which is opened by right-clicking *Analysis* in the analysis tree view. Click *View Solver Output File* as shown in Figure 32. Search for the mass by pressing *Ctrl+F* and search for "mass". The value is found under the headline *Element Mass* as shown in Figure 33. The mass is shown in the unit tonnes.

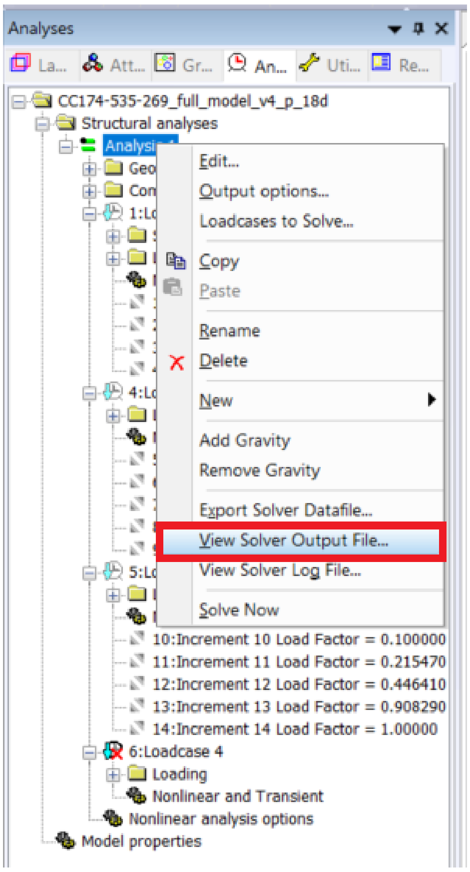

Figure 32: Accessing the .out-file

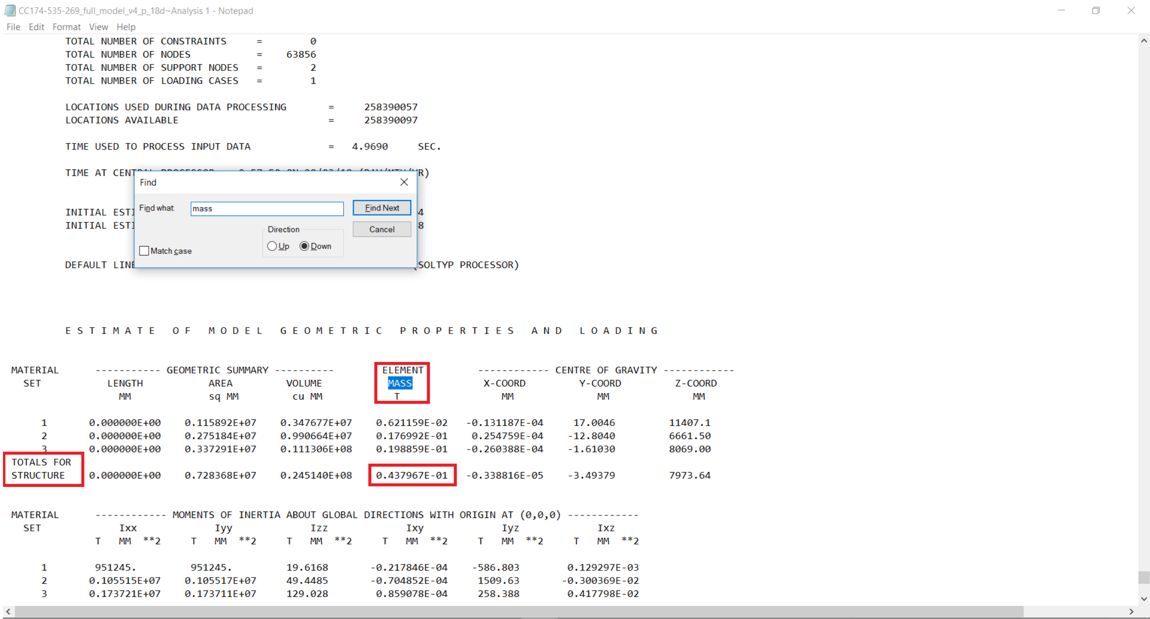

Figure 33: Mass information in the .out-file

3.3 Finding max stress and strain in a composite laminate model

In a LUSAS FE-model no differentiation will be made between stress or strain in resin and fibres. The material properties defined in the pre-processing of the model in Section 2.4 is the properties of the fibres and resin combined. Therefore the FE-model will approximate the material as homogeneous and make no differentiation will be made between fibre and resin. In this specific example the procedure to find maximum and minimum stress will be presented. The same procedure can be applied to find the maximum and minimum strain.

To find the maximum stress or strain in LUSAS stress and strain for each layer has to be analysed separately. To plot the stress or strain contours of a single ply got to the *Attributes* treeview. Expand the composite layup definition and right click the ply you want to inspect, as shown in Figure 34.

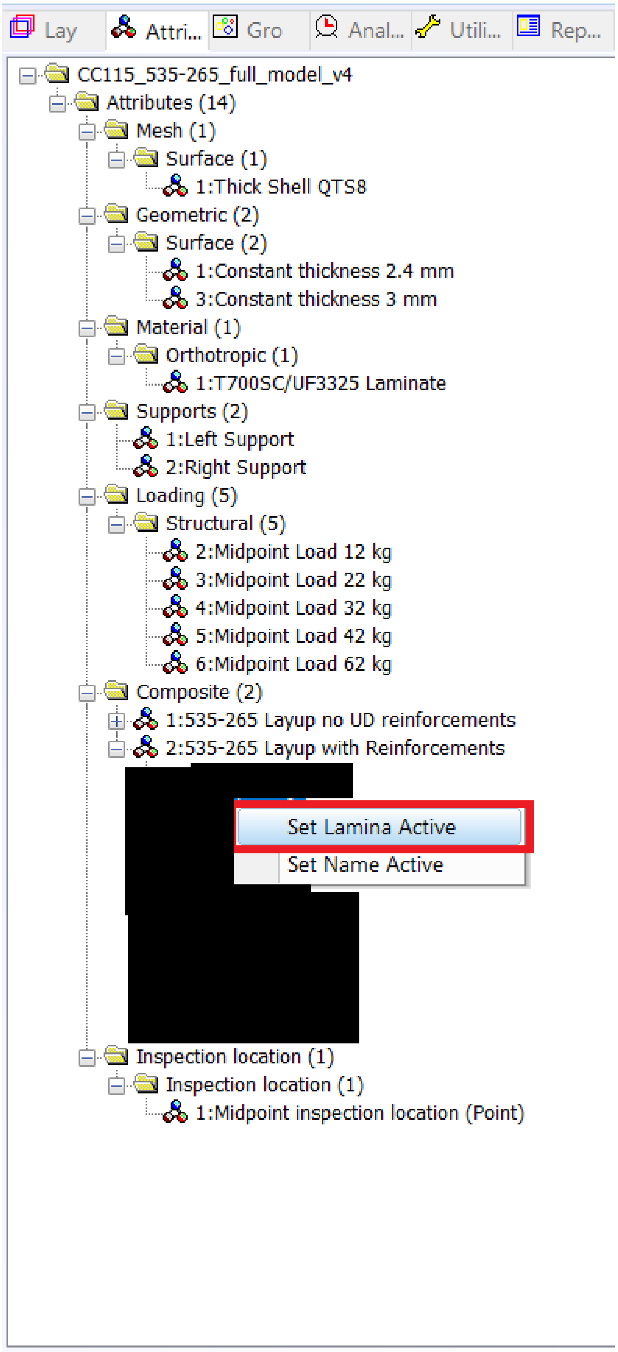

Figure 34: Selecting the active ply of a laminate.

With the active ply selected go to the layers treeview. Right click *Contours* and select *Properties*.

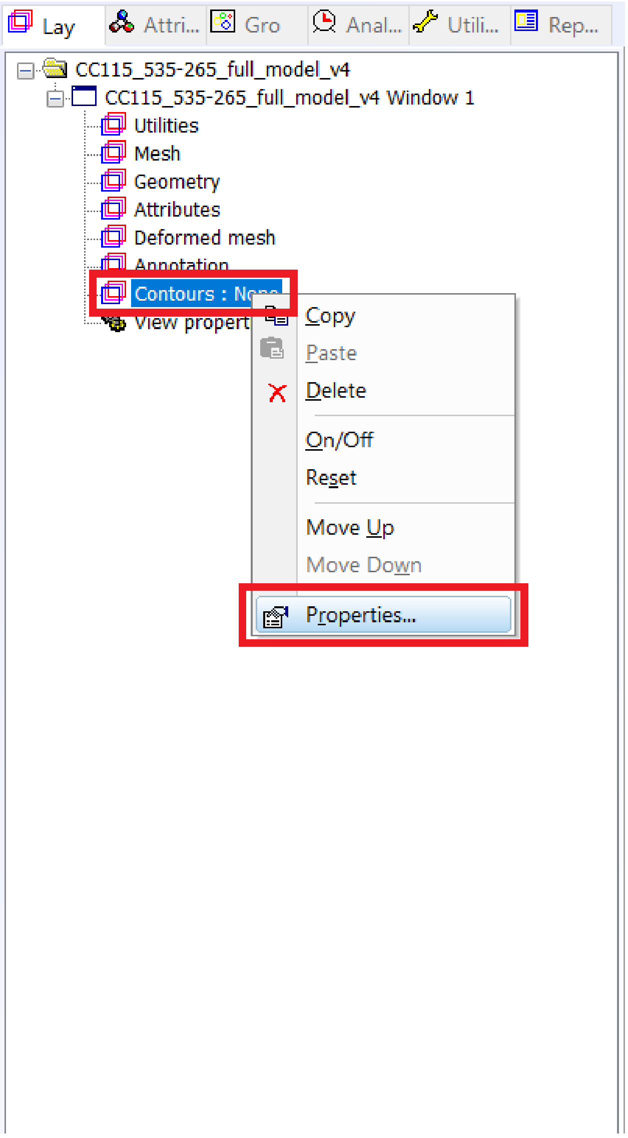

Figure 35: Editing the properties of a contours layer.

The following window will appear.

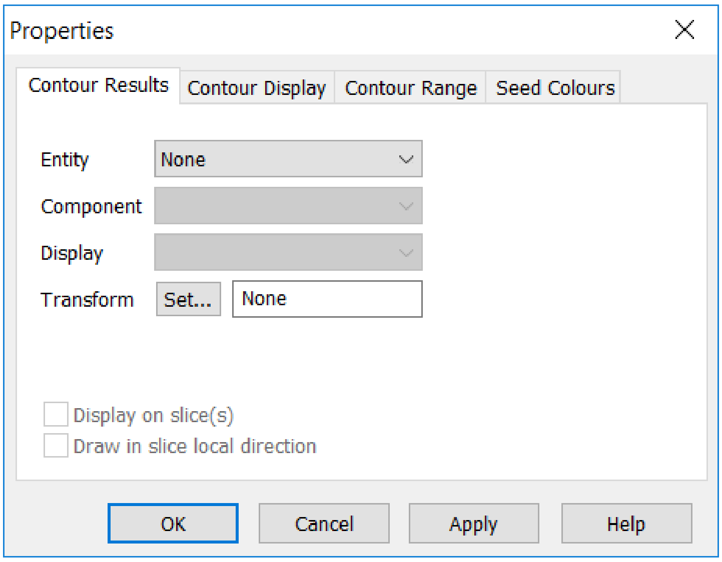

Figure 36: Properties of the contours layers.

From the *Entity* drop down menu select the stress you wish to analyse. Next to the *Transform* field, click *Set...*. In the results transformation window select the *Material* radio button and click OK. This transforms the stress or strain to the material directions of the active ply i.e the fibre directions of the active ply.

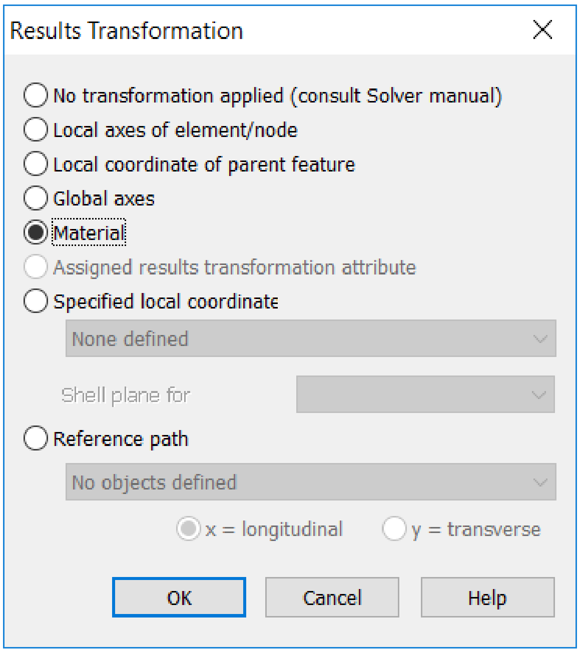

Figure 37: Results transformation window

When the transformation has been set to follow the material direction the components of the stress will follow the directions of the fibres. Selecting S_x in the *Component* drop down menu (Figure 38) will plot the stress in the fibre direction of the active ply. Likewise S_y will plot the stress transverse to the fibres. S_{xy} will plot the contours of the shear stress in the fibres and so on.

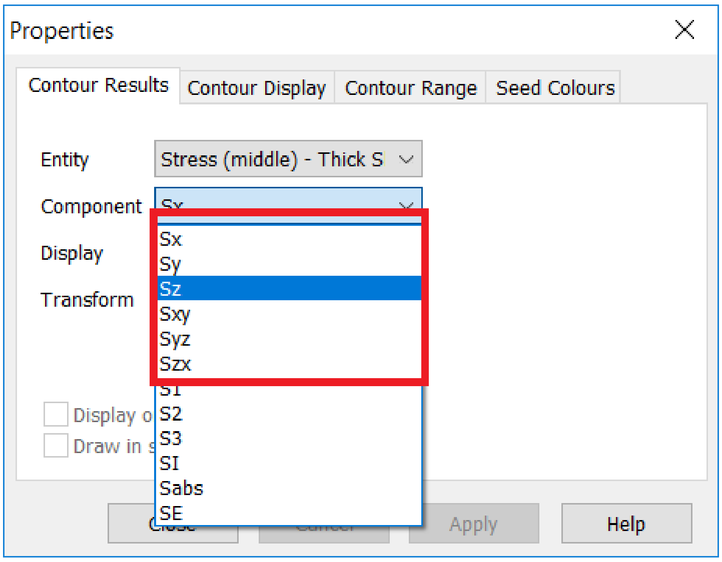

Figure 38: Components of laminate stress

When the desired *Entity* and *Component* has been selected press OK. The contours of the stress (or strain) will be plotted on top of the geometry as shown in Figure 39.

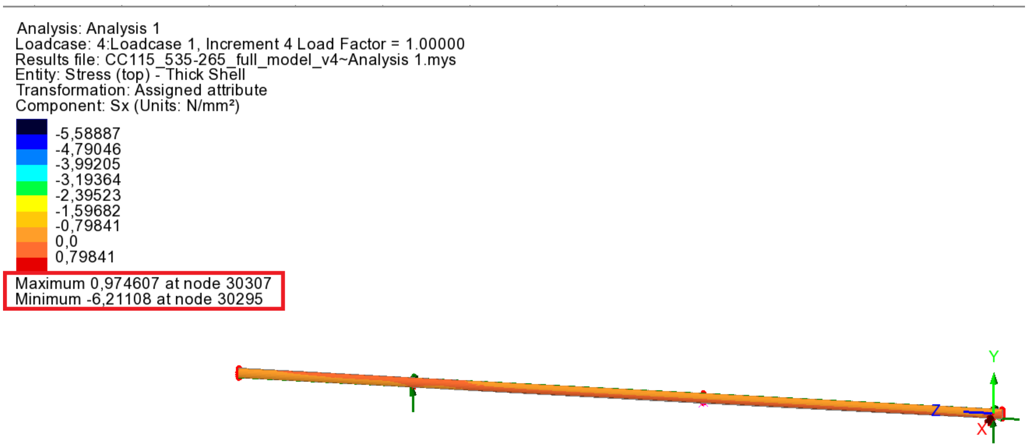

Figure 39: Stress in the fibre direction plotted on a mast

In the red box to the left in Figure 39 the location and magnitude of the maximum and minimum stress value can be seen. To find the location of the node go to Edit in the top bar and click advanced selection.

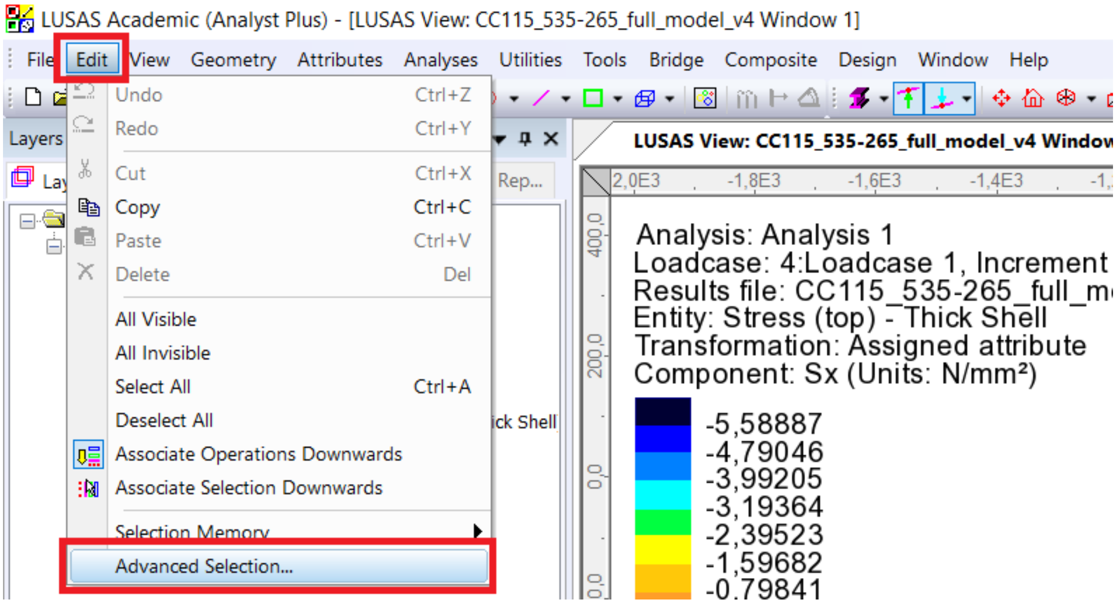

Figure 40: Advanced selection

The following window will appear:

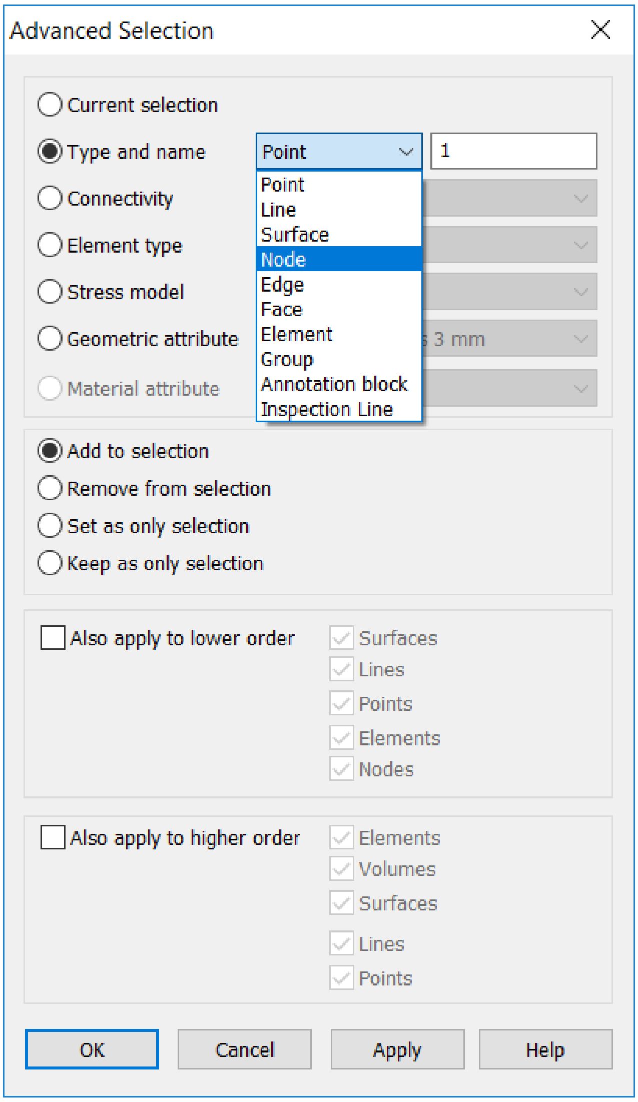

Figure 41: Advanced selection dialog window

From the *Type and Name* drop down menu select *Node* and enter the numbers of the nodes found inside the red box in Figure 39. In this case 30307 and 30295. Click OK and the nodes will appear selected in the model.

The procedure is then repeated for each and every ply in the model. Go back to treeview and select the next ply and repeat the process until all ply have been examined.

LUSAS has confirmed that there is no function inside the program at the moment for finding the maximum or minimum stress or strain in a model. The method proposed in this document was the simplest way found by the authors. It is possible that in future release that such a function might be included

4 Determining bending stiffness EI

With the model technique explained in Sections 2 and 3 the bending stiffness EI_x and EI_y can be determined for any given mast. The process of determining the bending stiffness includes creating a LUSAS FE-model according to the loadcase specified in Figure 42.

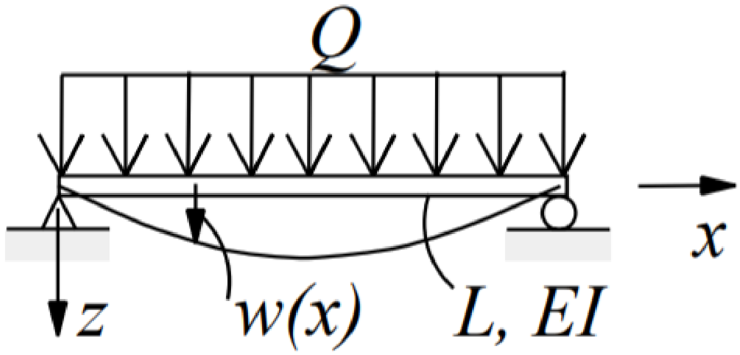

Figure 42: Loadcase used to determine bending stiffness.

The loadcase is that of a simply supported beam, subjected to an evenly distributed load along its entire length. The loadcase represents a mast being deflected by its inherent mass alone. To create the load case in LUSAS the mast section is simply swept to desired length L.

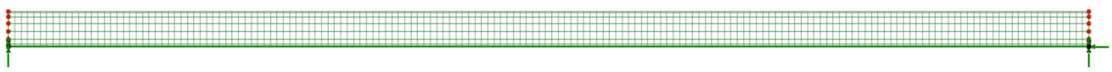

Figure 43: The loadcase modelled in LUSAS.

The length L should be such that the mast can be considered long and slender. For example, a mast produced on the 535-269 mandrel the length was set to $L = 13000\ mm$. This length ensured, in that specific case, that the mast was long enough to be considered slender.

If one wishes to determine EI_x the supports should be assigned to the points defining the aft line, as shown in Figure 44

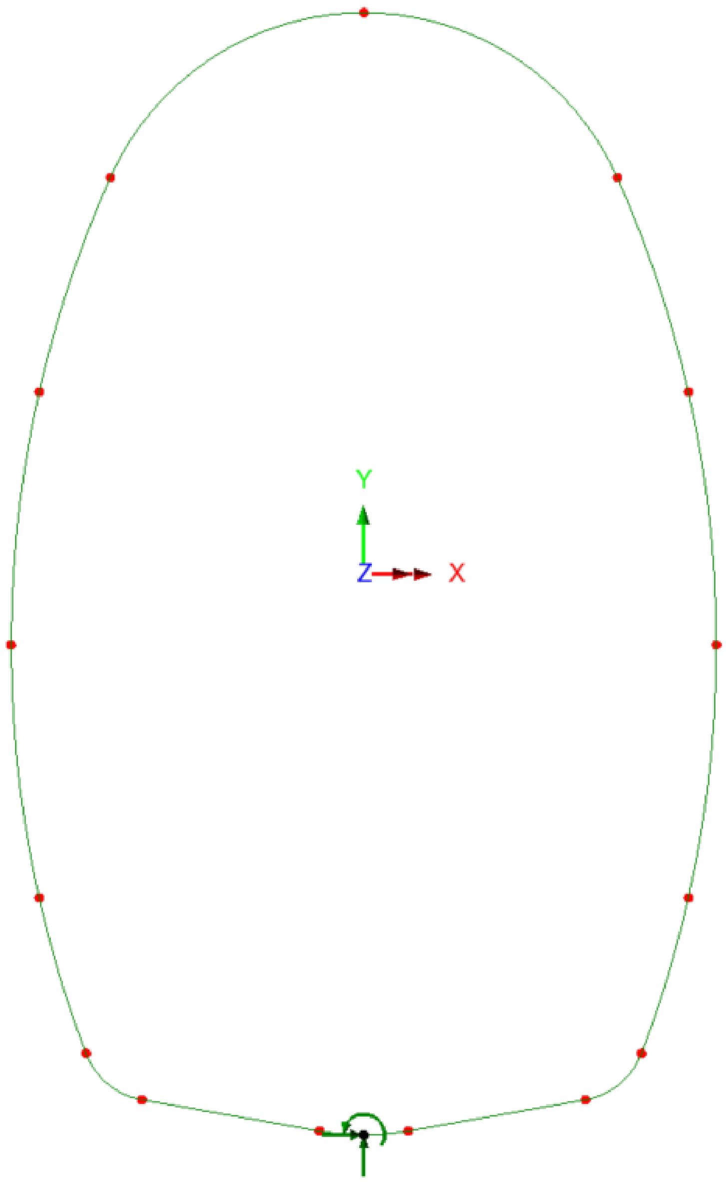

Figure 44: Support definition when determining EI_x.

To define EI_y the mast needs to be rotated 90°. To do this *select* the entire model by pressing *Ctrl+A* then go to *Geometry > Surface > Move* in the window that appears click the *Rotate* radio button. In the *Angle* field enter 90 and *select Z-axis* radio button, as shown in Figure 45

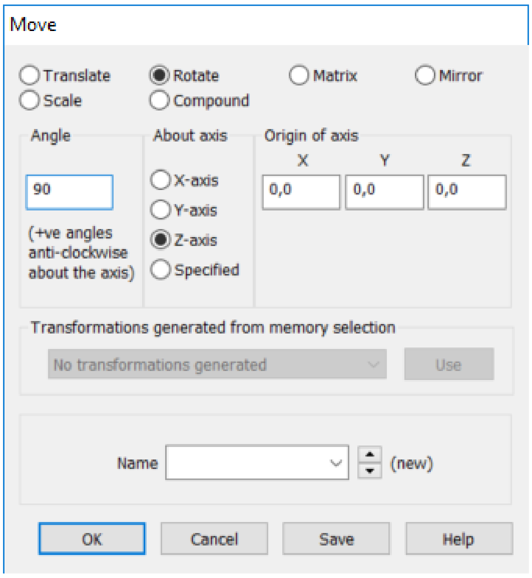

Figure 45: Geometry rotation dialog window.

The supports can then be assigned to the points defining the B-lines, as shown in Figure 46

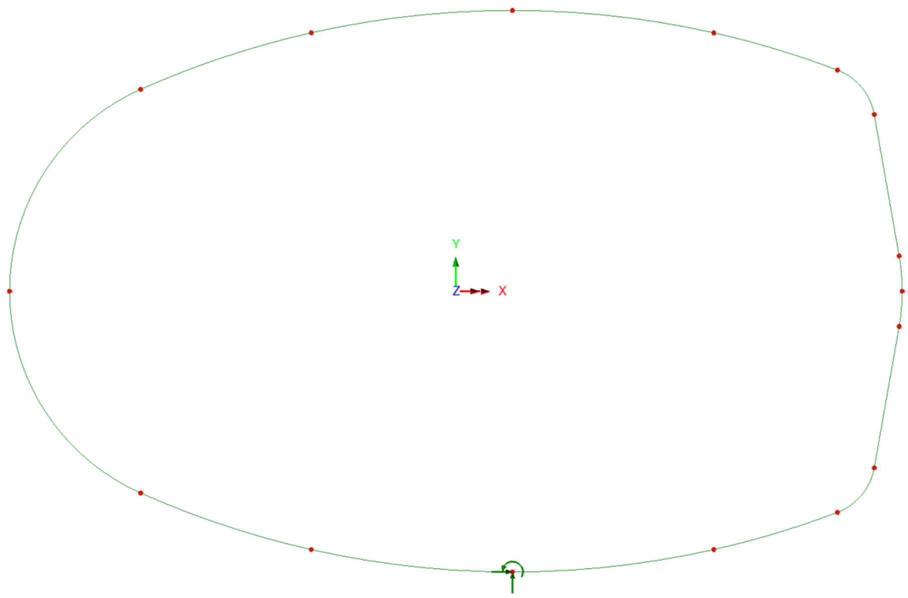

Figure 46: Support definition when determining EI_y.

Note! that when rotating the model the reference axis for gravity may need to be changed. See Section 2.5.2

Make sure that a inspection location is assigned at the mid span of the mast, Section 2.7.2. The deflection w, at the inspection location will later be used to determine the bending stiffness.

Run the simulation, make sure that the analysis completes without errors and that the model passes the checklist found in Appendix A.

In Figure 47 the deflection in the loading direction has been plotted

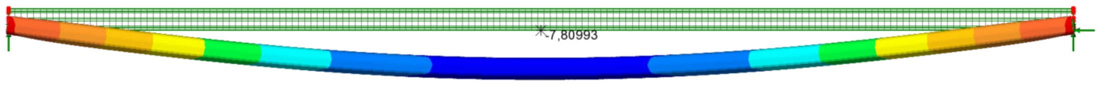

Figure 47: Deflection of the mast in the loading direction.

If the deflection seems reasonable the deflection at the midpoint i.e the deflection at the inspection location is noted. With this value the bending stiffness can now be determined.

The deflection in the elementary case shown in Figure 42 is determined by:

$$w(x) = \frac{QL^3}{24EI}\left(\frac{x^4}{L^4} - 2\frac{x^3}{L^3} + \frac{x}{L}\right) \tag{1}$$

Where Q is the resultant of the distributed load. In this case Q is calculated as:

$$Q = qL = \frac{mg}{L}L = mg \tag{2}$$

m is the mass of the model. To find the mass of the model see Section 3.2. By setting $x = \frac{L}{2}$ the deflection of the midpoint can be determined as:

$$w_{mid} = \frac{5QL^3}{384EI} \tag{3}$$

With this expression the bending stiffness is determined as

$$EI = \frac{5QL^3}{384w_{mid}} \tag{4}$$

Where w_{mid} is taken directly from the LUSAS model. Depending on if the model was modelled according to Figure 44 or 46 the bending stiffness will be either EI_x or EI_y.

A Analysis setup self-check

The following pages contain a basic checklist in order to find possible errors in the analysis setup. Checking the points in the list will make sure that all most of the possible mistakes when setting up the analysis can be avoided. It is recommended to read through the list before running the analysis.

Checklist for LUSAS simulations

Points on the list are signed with date and signature once they are checked.
Points which are not relevant may be crossed but should still be signed.

Analyst Name:

Reviewer Name

Report Number:

	Comment	Date	Sign Analyst	Sign Reviewer
Geometry				
Is the geometry based on the correct / latest revision?				
Geometry is based on drawings?				
All relevant geometry is included.				
Dimensions agree with drawings.				
Mesh				
Correct choice of dimensionality (solids, shells, beams).				
Correct choice of element type (reduced integration, hourglass control etc.)				
Elements have sufficient quality where it matters?				
Elements have sufficient size where it matters?				
How many percent of elements with warned quality exists?				
Do coincident elements or nodes exist?				
Element connectivity is correct.				
Properties				
Materials are defined according to specification. If no reference exists, the material definitions seem reasonable.				
Sectional properties are correct.				
All regions have been assigned with correct section properties.				
Shell normal directions are correct.				
All shell/membrane elements are defined on midsurfaces? If not, are the offsets correct?				
Shell thicknesses are correct.				
Inertia and mass elements are correct.				
Total mass in the .out file corresponds to the report or expected value.				
Analytical surfaces are correct.				
Material orientations are correct.				
Units are correct and corresponding.				
Interactions				
Contact – Master and slave surfaces are correctly chosen.				
Contact – Initial adjustments of slave nodes are small compared to the geometry dimension.				

	Comment	Date	Sign Analyst	Sign Reviewer
Contact – Appropriate normal and tangential behaviour are used (pressure – over closure behaviour, friction etc).				
Connector elements have the correct functionality (type, behaviour, orientation).				
Multipoint constraints (MPC, Couplings) are correct.				
Boundary Conditions and Loads				
Loads are applied as intended (according to specification).				
Boundary conditions are applied as intended (according to specification) and seem reasonable.				
Load amplitudes (time histories) are defined as intended (according to specification).				
All relevant load cases are evaluated.				
Analysis - General				
Sufficient geometry is included for a local analysis.				
Warnings in the .dat file are not critical.				
Local coordinate systems and orientations are correct.				
Is large deformation theory used?				
Have self-weight been included or not?				
Are the FE-model and analysis in general adequate for this structural assessment?				
Analysis – Dynamic specific				
Centre of gravity is correct for all parts.				
Damping is defined according to specification. If no reference exists, the assumptions seem reasonable.				
Sufficiently small increments are used in the time and frequency domain.				
Results				
Stress levels seem reasonable.				
Magnitude of displacements / deformations seems reasonable.				
Deformed state seems reasonable.				
Reaction forces are correct.				
The results are extracted properly, from relevant nodes, elements, section points.				